UC Berkeley
UC Berkeley Electronic Theses and Dissertations

Title

A Multiplexed Strontium Optical Lattice Clock

Permalink

https://escholarship.org/uc/item/5876b3f2

ISBN

9798189279867

Author

Dolde, Jonathan Caldwell

Publication Date

2026-05-01

Peer reviewed|Thesis/dissertation

eScholarship.org Powered by the California Digital Library
University of California

A Multiplexed Strontium Optical Lattice Clock

by

Jonathan Caldwell Dolde

A dissertation submitted in partial satisfaction of the

requirements for the degree of

Doctor of Philosophy

in

Physics

in the

Graduate Division

of the

University of California, Berkeley

Committee in charge:

Associate Professor Shimon Kolkowitz, Chair
Assistant Professor Harry Levine
Assistant Professor Mengjie Yu

Spring 2026

A Multiplexed Strontium Optical Lattice Clock

Copyright 2026
by
Jonathan Caldwell Dolde

Abstract

A Multiplexed Strontium Optical Lattice Clock

by

Jonathan Caldwell Dolde

Doctor of Philosophy in Physics

University of California, Berkeley

Associate Professor Shimon Kolkowitz, Chair

Optical atomic clocks have spurred a range of precision frequency comparison experiments and proposals including tests of general relativity, gravitational wave detection, and relativistic geodesy. Current measurements using optical atomic clocks are often limited by the coherence of the clock laser rather than the atomic samples used as a frequency reference. In order to overcome the performance limits imposed by clock laser coherence, we realize a multiplexed optical clock system where multiple spatially resolved ensembles each consisting of thousands of strontium atoms trapped in a 1D optical lattice function as separate atomic frequency references that can be simultaneously interrogated with a shared clock laser. This scheme allows us to make differential frequency comparisons with a quantum projection noise limited fractional instability of $9.7(4)\times10^{-18}/\sqrt{\tau}$ and a differential fractional uncertainty of 8.9×10^{-20} after 3.3 hours of averaging. We then use this system to perform a lab-based test of the gravitational redshift at the centimeter scale, where we measure a fractional frequency gradient of $[-12.4\pm0.7_{\mathrm{stat}}\pm2.5_{\mathrm{sys}}]\times10^{-19}$/cm, consistent with the predicted value of 10.9×10^{-19}/cm. Having demonstrated that our differential comparisons are no longer limited by the local oscillator, we turn to fundamental limits on atom–atom coherence. We perform a direct decay measurement of the natural lifetime of the excited clock state $^3\mathrm{P}_0$ in ^{87}Sr, in which we use measurements of simultaneously loaded high and low density atomic ensembles and compare decay rates of ^{87}Sr and ^{88}Sr to help isolate natural lifetime decay from other population dynamics. We measure a lifetime of 167^{+79}_{-40}, which is consistent with previously reported experimental and theoretical values. Lastly, we demonstrate a hyperfine-resolved readout scheme in ^{87}Sr that converts depolarization errors during interrogation into erasure errors, extending coherence times between ensembles in our optical lattice clock up to 150s using spin-echo measurements. These results taken together demonstrate the advantages of differential clock measurements that aren't limited by clock laser coherence and how to characterize and improve on the performance limits that arise in that regime.

For Bert.

Light of my life, love of my hug.

Contents

Contents **ii**

List of Figures **v**

List of Tables **vii**

1 Introduction **1**
1.1 Atomic clocks . . . 1
1.1.1 Optical atomic clocks . . . 1
1.2 Atomic clock working principle . . . 3
1.3 Why does strontium make a good clock? . . . 4
1.4 Differential clock comparisons . . . 5
1.5 Thesis outline . . . 6

2 Experimental setup **8**
2.1 Overview of the multiplexed optical lattice clock . . . 8
2.2 Vacuum system . . . 9
2.3 Magnetic field control . . . 9
2.4 Laser Systems . . . 10
2.4.1 461 nm laser system . . . 10
2.4.2 679 & 707 nm laser system . . . 11
2.4.3 689 nm laser system . . . 13
2.4.4 813 nm laser system . . . 14
2.4.5 698 nm laser system . . . 19
2.5 Readout . . . 19
2.5.1 Calibration procedure . . . 27
2.6 General experimental sequence . . . 28
2.7 Measuring differential frequencies . . . 31
2.8 Simultaneous loading of different isotopes of Sr . . . 34

3 Gravitational redshift at the centimeter scale **38**
3.1 Introduction to our gravitational redshift measurement . . . 38

3.2 Atom preparation and experimental procedure . . . 41
3.3 Systematic evaluation in detail . . . 42
3.3.1 Systematic evaluation summary . . . 42
3.3.2 Zeeman shifts . . . 43
3.3.3 Density shift . . . 46
3.3.4 Black-body radiation shift . . . 46
3.3.5 Lattice light shift . . . 49
3.3.6 Probe Stark shift . . . 52
3.3.7 DC Stark shift . . . 53
3.3.8 Ellipse fitting . . . 54
3.3.9 Wannier-Stark ladder, imaging, and the expected gravitational redshift 54
3.4 Measurement of the gravitational redshift . . . 57
3.5 Relativistic clock height difference measurements . . . 59
3.6 Context and discussion . . . 60

4 Measurement of the natural lifetime of the $^3P_0$ clock state in ^{87}Sr 62
4.1 Introduction . . . 62
4.2 Lifetime measurement setup . . . 63
4.3 Decay modeling and analysis . . . 68
4.3.1 One-body loss . . . 69
4.3.2 Two-body loss . . . 69
4.4 Low-density data . . . 72
4.5 Black-body scattering rate . . . 73
4.6 Lifetime measurement conclusions and outlook . . . 74

5 Erasure conversion in an optical lattice clock 76
5.1 Introduction . . . 76
5.2 Comparing erasure and dephasing error limits on differential fractional frequency instability . . . 77
5.3 Impact of Raman Scattering and Radiative decay on Atomic Coherence . . . 80
5.4 Measurement of hyperfine state population distribution induced by Raman scattering . . . 82
5.5 Hyperfine-state-resolved readout method . . . 83
5.6 Enhanced atomic coherence . . . 86
5.6.1 Synchronous Ramsey spectroscopy . . . 86
5.6.2 Modified synchronous spin echo spectroscopy . . . 87
5.7 Resulting differential stabilities and the associated metrological gain . . . 89
5.8 Conclusion . . . 91

6 Future Work 93

Bibliography 98

A Supplemental material for Chapter 5 **113**
A.1 Ellipse fitting with maximum likelihood estimator 113
A.2 Modified spin echo sequence 114
A.3 Raman scattering population distribution calculation 115
A.4 Theoretical discussion on coherence enhancement 115
A.5 Numerical simulation of the experiment 118
A.6 Discussion of technical limitations 120
A.7 Coherence and Allan deviation at all trap depths 120

List of Figures

1.1 Optical atomic clock diagram 2
1.2 ^{87}Sr simplified level structure 5

2.1 CAD model and photo of our vacuum system 9
2.2 461 nm laser diagram 12
2.3 679 & 707 nm repump laser diagram 13
2.4 689 nm laser diagram 15
2.5 689 nm laser frequency chain 16
2.6 Operational magic wavelength of $|g, m_F = \pm 5/2\rangle \rightarrow |e, m_F = \pm 3/2\rangle$ transition . 18
2.7 EMCCD images and timing diagram for loading multiple spatially separated atomic ensembles 20
2.8 813 nm laser system 21
2.9 698 nm laser diagram 22
2.10 Rabi linewidth and Ramsey coherence time limited by our local oscillator noise 23
2.11 Experiment table-level laser diagram 24
2.12 Experiment middle-level laser diagram 25
2.13 Experiment mezzanine-level laser diagram 26
2.14 Spatial imaging efficiency 28
2.15 Experimental timing diagram 29
2.16 Atomic temperatures in the optical lattice 30
2.17 Hyperfine clock levels of ^{87}Sr. Due to the I=9/2 nuclear spin of ^{87}Sr , there are 10 m_F sublevels in $^1S_0$ and $^3P_0$. The solid arrows show interrogations of both the $|g, m_F = \pm 9/2\rangle \rightarrow |e, m_{F'} = \pm 9/2\rangle$ and $|g, m_F = \pm 5/2\rangle \rightarrow |e, m_{F'} = \pm 3/2\rangle$ transitions. The dashed arrows show the coherent transfer pulses to load into the $|g, m_F = \pm 5/2\rangle$ state from the spin stretched $|g, m_F = \pm 9/2\rangle$ state. 31
2.18 Experimental shot to shot excitation fraction using synchronous Ramsey interrogation 32
2.19 QPN limits on differential frequency uncertainty 34
2.20 Differential frequency measurement 35
2.21 Demonstration of simultaneous isotope loading in our multiplexed clock system 37

3.1 Experimental setup of gravitational redshift measurements 40
3.2 Redshift systematic evaluation summary 44

3.3 Black-body redshift systematic evaluation . . . 47
3.4 Lattice-induced AC Stark shift systematic evaluation . . . 50
3.5 Probe Stark shift evaluation. . . . 52
3.6 Ellipse fitting bias error evaluation. . . . 55
3.7 Wannier-Stark ladder sidebands. . . . 56
3.8 Redshift measurement . . . 57
3.9 Measurements before and after removal of the blinded offset gradient. . . . 58
3.10 Height determination with measured gravitational redshift . . . 60

4.1 Population decay in an optical lattice . . . 64
4.2 Population decay measurement scheme and example data for ^{87}Sr . . . 65
4.3 Decay rate Γ_{eg} from the excited $^3P_0$ state to the ground $^1S_0$ state in ^{87}Sr (blue) and ^{88}Sr (red) as a function of lattice trap depth . . . 67
4.4 One-body loss rates for ground Γ_g and excited Γ_e states for high and low density ensembles of ^{87}Sr and ^{88}Sr. . . . 70
4.5 Inferred values of two-body loss K_{ee} for high-density ensembles of ^{87}Sr and ^{88}Sr. 72
4.6 Comparison of extracted decay rates between high (solid) and low (dashed) density ensembles of ^{87}Sr and ^{88}Sr as a function of trap depth. . . . 73
4.7 Comparison of measured ^{87}Sr lifetime values . . . 75

5.1 Comparison of phasing and erasure errors in an optical lattice clock . . . 79
5.2 Lattice photon-induced Raman scattering and its effect on hyperfine state populations . . . 81
5.3 Hyperfine state population ratio measurement of erasures. . . . 84
5.4 Illustration of pulse sequence used for hyperfine state resolved readout, starting with a quantum superposition between $|g, 5/2\rangle$ and $|e, 3/2\rangle$ . . . 85
5.5 Comparison of coherence times using standard readout, hyperfine-resolved readout, and reconstructed standard readout methods . . . 88
5.6 Extracted Allan deviations at 1 second for the differential clock comparisons for Ramsey and spin echo under varying readout conditions . . . 90

6.1 Einstein equivalence principle test in a movable 1D lattice clock . . . 95
6.2 Next generation experiment . . . 96

A.1 Illustration of modified spin echo sequence. . . . 114
A.2 Theoretical decoherence rate for Ramsey and spin echo sequences with varying erasure fractions . . . 117
A.3 Coherence, atom number and clock stability as functions of clock interrogation time at all trap depths measured . . . 121

List of Tables

3.1 Redshift measurement uncertainty budget 45

4.1 Summary of experimentally measured rates and comparison with existing theory. 71
4.2 Contribution of statistical and systematic uncertainties to the total uncertainty in extracted radiative decay rates. 74

A.1 Theoretically calculated Raman scattering rates from $|^3\mathrm{P}_0, m_F = 3/2\rangle$ 115

Acknowledgments

To begin, my many thanks to Shimon Kolkowitz, my advisor for this dissertation. He helped me to develop my scientific inquiry skills and his ideas and suggestions were invaluable to my graduate career. His enthusiasm for science truly shows, it was always exciting to share new data with him. I really appreciate his problem-solving perspectives, which always made difficult problems easier. I'm very grateful to be able to put all of his advice and mentorship towards what comes next in my career. I want to thank my other committee members, Harry Levine and Mengjie Yu, who have both been great to interact with during my shorter time here at Berkeley. I really appreciate their time put towards reviewing my dissertation and their expertise for helping me improve it. I also want to thank Joel Moore for serving on my qualifying exam committee.

As for my labmates, I want to start by thanking Xin Zheng, from whom I've learned everything there is to know about working in lab. Thanks for taking time to show a graduate student who'd never worked in AMO physics how it all works. Xin has such a talent for making things in lab just work, and could always un-stick me from any mess I made while learning. Matt Cambria is a fantastic scientist and great friend, it was always amazing to watch him shred on the keyboard or guitar. I loved the passion Aedan Gardill always had for both his experiments and scientific outreach, he showed me how much a graduate student can accomplish simultaneously. The two undergrads I got to work with during my time at UW Madison, Brett Merriman and Haoran Li, put in so much effort that was always a huge help in lab.

After our lab's move to Berkeley, I got to work with a whole new team, who helped me to learn how to work in a large(r) group. Dhruva Ganapathy's perspective from a different field always helped me to think about the broader context of physics outside of the narrow window of the lab. His ability to analyze things from multiple views is super impressive, and something I know will take him far. I also have to mention his taste in tastes, the man never misses with a restaurant recommendation. Shuo Ma's ability to move fast is a real sight to behold, and somehow the hardest problems always seem to be solved with a quick walk with him to Sheng Kee. His help in lab has been invaluable. Anke Stöltzel's directness is so refreshing, that she refuses to nod along when something didn't add up, and I appreciate her willingness to ask the question everyone else was thinking. It made the work better every time. I still can't believe how quickly Andrew Householder has taken to the SrI experiment, he's been amazing at asking questions and making improvements. I'm really excited for his career based on how much I've seen from him so far. Finally for strontium team members, I want to acknowledge my former π^2 mentee, Bennett Christensen, who's truly grown to be a great researcher and good friend, you're really gonna kill it at grad school. Across the control room, I really admire the entire NV lab team. I'm always jealous of Saroj Chand's dedication and great attitude. Caitlin Mary Reiter has always shown passion for her experiment, and I've seen her become so much more confident in her abilities. Alyssa Matthews has been such a cheerful presence in the control room, and it's always been a real honor to get to visit

Sweetpea. It's been a pleasure to get to know Yael Sternfeld since she's arrived to the lab, and I can already tell she's a great addition to the NV team.

I want to thank the graduate students at UW-Madison that commiserated with me during classes and celebrated with me after finals, including my trusty roommates/butlers Cameron Kuchta and Sophia Nowak, Josh "the goblin" Peterson, Ricardo Ximenes, Abby Bishop, Ganesh Parida. I also want to thank Jacob Scott for being a friendly face down the hall in Chamberlin, always willing to lend a hand, a thought, or a lens that I *really* need right now.

Thanks to all the amazing instructors I've had throughout my studies. My high school physics teacher, Brad Jacobsen, inspired my love of physics. Paul Kleiber's *Physics I* and *Intro. to Quantum Mechanics I* courses were fantastic undergraduate classes, and he always carried a room-brightening smile to every lecture. Lisa Everett taught an amazing two semesters of graduate quantum that have been a foundation of my ability as a physicist. Her office hours were good at both elevating minds and lifting spirits.

The support staff that I've worked with have always gone above and beyond to make things so much smoother for me. Ann Austin always seemed to be able to move heaven and earth to get a purchase order placed when we needed, and I always loved to complain about vendors with her. Claire Legas has been an invaluable colleague, willing to answer whatever innane question I had about Berkeley bureaucracy. It was great to get to chat in the mornings with her. Carlos Bustamente and Espe Munoz-Riddle were so helpful at resolving logistics issues that came up.

I want to acknowledge all the people who help to develop free and open source resources for physics education and research, and especially Alexander Franzen for developing the ComponentLibrary that I've used to help create many of my laser system diagrams in this dissertation.

To close, I want to thank my family. To my parents, who have never stopped supporting me and have always worked hard to ensure I have as many opportunities as possible. To Matt and Sam, my brothers that have always had my back, and always will. And of course to Hailey, for always supporting my pursuits, big and small, and making life so much more fun together.

Chapter 1

Introduction

1.1 Atomic clocks

Clocks track the passage of time by recording occurrences of a regularly repeating phenomenon. The more often the repetition occurs, the smaller the interval of time we can measure, and the better our clock's precision. In the same vein, the more regular our repeating phenomenon is, the more stable our clock can be. In general, a good clock should be as precise and stable as possible. The development of the atomic clock in the mid-20th century, with Essen and Perry demonstrating the first Cs beam clock in 1955 [1], allowed for rapid development of timekeeping [2–4] and navigation [5–8]. The most famous application of atomic clocks has been their use in global navigation satellite systems (GNSS) such as the Global Positioning System (GPS) [5]. Atomic clocks have also been a key part of many physical science experiments [9–12], such as the famous Hafele–Keating experiment [10], where atomic clocks were flown on commercial airliners both with and against Earth's rotation to test both the velocity-induced time dilation predicted by special relativity and the gravitationally-induced time dilation predicted by general relativity.

The general principle of atomic clock operation is to count the number of oscillations of electromagnetic (EM) waves corresponding to the energy difference between internal (electronic, hyperfine, or nuclear) states in an atomic reference. Early atomic clocks referenced their electromagnetic wave frequency to the ground state hyperfine splitting of ^{133}Cs, corresponding to a microwave frequency of about 9.19 GHz. In 1967, the General Conference on Weights and Measures officially adopted the definition of the SI second to be exactly 9,192,631,770 oscillations of EM waves corresponding to this hyperfine transition in ^{133}Cs [2].

1.1.1 Optical atomic clocks

In the late 20th century, a new category of atomic clocks emerged; one that was based on an optical frequency as opposed to the previous microwave atomic clocks [13–16]. This type of atomic clock, the optical atomic clock, could theoretically outperform microwave atomic clocks as the oscillations of these optical clocks occur at optical frequencies (100s of THz),

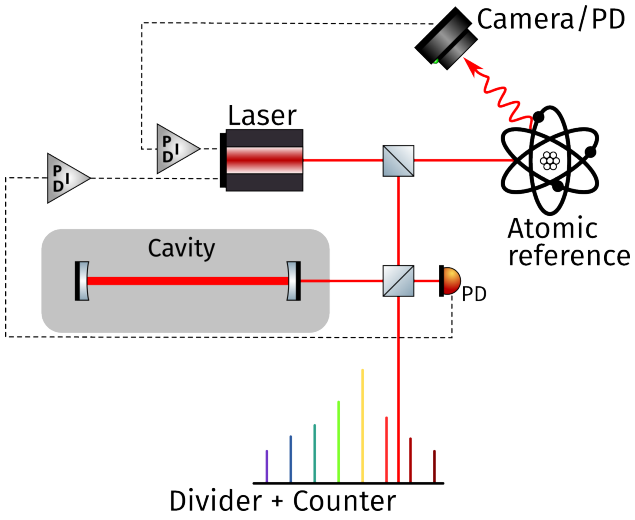


Figure 1.1: The basic optical atomic clock architecture. The laser serves as the clock's local oscillator, and is referenced to a cavity for short-term stability and an atomic transition for long-term drift correction. The local oscillator's ticks are converted to microwave frequencies through the use of a self-referenced frequency comb, which are then counted and distributed with electronic systems.

about 10^4 faster than the 9.19 GHz microwave frequency of the ^{133}Cs hyperfine transition. More oscillations in the same amount of time allowed these new optical atomic clocks to reach the same frequency precision much faster, and could therefore reach new frequency precision regimes that were previously untenable for the microwave atomic clock.

Microwave-based atomic clocks still performed better than early optical atomic clock realizations [17, 18], primarily due to an outstanding technical issue with optical atomic clocks. The electronics used for keeping track of these clock oscillations were not, and still are not, fast enough to count optical frequencies, making phase-coherent connections between the optical and microwave frequency domains extremely difficult. This technical hurdle was overcome in 1999, when the self-referenced optical frequency comb was developed [19, 20], which allowed for precise and relatively simple translation of the optical frequency domain into something electronic systems could process and distribute. The general setup for an optical atomic clock is shown in Fig. 1.1.

Optical atomic clock frequency precision eventually outperformed microwave atomic frequency precision by 2006 with a Hg^+ ion clock [21], reaching a total fractional frequency uncertainty of 7.2×10^{-17}. This new frequency precision horizon has led to a wide array of new physics experiments and proposals, including dark matter searches [22–24], gravitational wave detection [24–27], precision geodesy [28–32], tests of fundamental physics [33, 34].

1.2 Atomic clock working principle

Most optical atomic clocks today operate in a pulsed interrogation mode where an atomic sample is first prepared into some initial state, then the sample's electronic transition frequency is compared to the local oscillator's (clock laser's) oscillation frequency during what's often termed "coherent interrogation", and finally the atomic sample's electronic state is read out in order to determine the frequency offset or detuning between the atomic transition and the local oscillator. This information is then used to correct the frequency of the local oscillator such that it tracks the stable atomic transition frequency. During coherent interrogation, two main spectroscopic techniques are used to determine the relative detuning of the clock laser and the atomic reference, Rabi spectroscopy [35] and Ramsey spectroscopy [36]. In Rabi spectroscopy, a near-resonant oscillating EM field of frequency ω interacts with a two-level atomic system with energy splitting $E_0 = \hbar\omega_0$ for a certain period of time, T_{rabi}, and the relative population of atoms in the excited state is given as

$$P_e(\Delta, T_{rabi}) = \frac{\Omega^2}{\Omega^2 + \Delta^2} \sin^2\left(\frac{\sqrt{\Omega^2 + \Delta^2}}{2} T_{rabi}\right) \tag{1.1}$$

where $P_e = N_e/(N_e + N_g)$ where N_e is the number of atoms in the excited state, N_g is the number of atoms in the ground state, Ω is the Rabi frequency, determined by the strength of the interaction between the EM field and the atomic transition, and $\Delta = \omega - \omega_0$ is the frequency detuning between the transition and the EM drive. The full-width half-maximum (FWHM) of this lineshape goes as $\approx 0.8 \times 1/T_{rabi}$ on resonance, allowing one to determine the atomic transition's frequency more precisely the longer the EM field interacts with the atom. In 1950, Norman Ramsey described an improved version of Rabi spectroscopy, where instead of the EM field interacting with the atomic sample during the entire period of the interrogation, two short pulses are used at the beginning and end of the interrogation, with the atomic sample freely evolving at a rate determined by the detuning of the EM field and the atomic transition. After the second pulse, the relative population of atoms in the excited state looked like

$$P_e = \frac{1}{2}\left(1 + \cos(\Delta T_{Ramsey})\right) \tag{1.2}$$

on the assumption of short pulse time compared to the total length of interrogation, T_{Ramsey}. The FWHM of the Ramsey fringes are $1/2 \times 1/T_{\text{Ramsey}}$) and therefore we see that for the same amount of interrogation time, the Ramsey method has a line shape of $(0.5/0.8) \approx 0.63$ times as broad as the Rabi method, giving a more precise determination of the atomic transition frequency. Ramsey also has the added benefit of having the EM field in contact with the atomic sample for very little of the interrogation time, meaning that fluctuations in laser intensity during this time don't affect your determination of the atomic transition frequency like they would with the Rabi method.

In order to more quantitatively define the performance limits of an atomic clock, we can write down the instability of an atomic clock using Ramsey spectroscopy based on the

fundamental quantum noise floor for unentangled atoms, known as quantum projection noise (QPN)[37].

$$\sigma_{QPN}(\tau) = \frac{1}{2\pi\nu CT}\sqrt{\frac{T+T_d}{N\tau}} \tag{1.3}$$

where σ_{QPN} is the overlapping Allan deviation [38, 39], a convergent measure of frequency instability for the types of noise processes that occur in atomic clocks, ν is the clock transition frequency, C is the contrast (fringe visibility), T is the coherent interrogation time, T_d is the dead time, τ is the total averaging time, and N is the number of atoms being interrogated. This noise arises from the inherent probabilistic nature of quantum mechanics, and represents the fundamental lower limit of an atomic clock instability using unentangled atoms[1]. From this fundamental noise limit, we can see that a high frequency transition, large atom numbers, and a long averaging time are all desirable aspects for a high precision clock. As of the time of writing, the most precise clocks are based on narrow (mHz level) optical transitions in strontium (Sr) and ytterbium (Yb). These clocks can simultaneously interrogate thousands of these atoms at a time, helping to drive down the QPN limit even further.

1.3 Why does strontium make a good clock?

Strontium is one of a few ideal atoms for optical atomic clock systems. Strontium is a group II (alkaline earth) element, where its outer shell is composed of two valence electrons with a ground state atomic configuration of $5s^2$, $^1\mathrm{S}_0$. For Sr's stable bosonic isotopes (^{88}Sr, ^{86}Sr, ^{84}Sr), there is no first order sensitivity to magnetic fields in the ground state as both J=0 and I=0, and the fermionic isotope (^{87}Sr) is sensitive only through nuclear spin interaction as I=9/2.

The electronic structure of ^{87}Sr is shown in Fig. 1.2. The first transition to note is the $^1\mathrm{S}_0 \rightarrow ^3\mathrm{P}_0$ transition. In fermionic ^{87}Sr, this doubly-forbidden transition is weakly allowed through hyperfine mixing within the $^3\mathrm{P}_J$ manifold [45]. The natural linewidth for this transition, Γ, is approximately $2\pi\times$ 1 mHz. This transition is at 698 nm (429 THz) and serves as our "clock" transition, due to the extremely high precision of this transition, with a quality factor, Q = 429 THz/1 mHz $\approx 4 \times 10^{17}$. Furthermore, it is first order insensitive to magnetic fields as it is a J=0 $\rightarrow$ J=0 transition. Depending on the specific hyperfine ($\mathrm{m}_F \rightarrow \mathrm{m}_{F'}$) transition, this magnetic field sensitivity can be as low as 22 Hz/G in ^{87}Sr for the $|^1\mathrm{S}_0, m_F = 5/2\rangle \rightarrow |^3\mathrm{P}_0, m_{F'} = 3/2\rangle$ [46].

In order to make use of this clock transition, we want to prepare a dilute, gaseous, sample of strontium at very cold temperatures to mitigate atom-atom interactions and thermal motion-induced Doppler shifts that broaden and shift the clock transition. To do this, we first heat a small chunk of strontium metal to 360° C, then use progressive stages of laser

[1]There have been implementations of atomic clocks that use entangled atomic samples to do better than this unentangled limit[40–43], but they have yet to demonstrate absolute performance better than unentangled clocks[44] as of the time of writing.

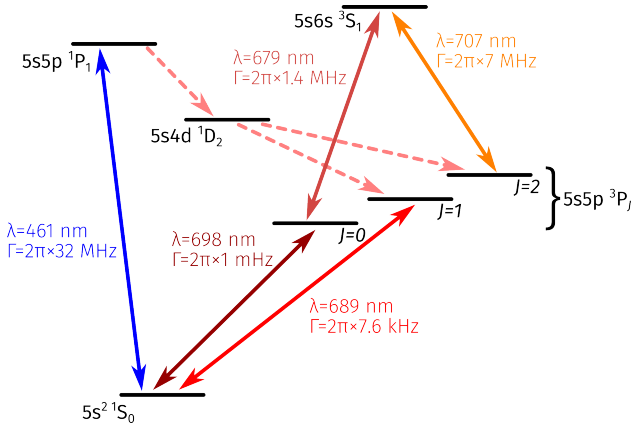


Figure 1.2: Level structure of ^{87}Sr showing transitions relevant for our optical clock implementation. As discussed in Section 1.3, the three transitions from the $5s^2\ ^1S_0$ are all key parts of why strontium is a good atomic reference for an optical atomic clock.

cooling and trapping to create such a sample, which is where two other transitions from the ground state come into play. Very briefly, laser cooling works by imparting momentum to an atom through a photon interaction that drives the atom's velocity towards zero. This cooling method is limited by the rate at which the atom interacts with the cooling laser and the minimum temperature achieved from the cooling. The minimum temperature achievable through Doppler-cooling is given by

$$T_{\text{Doppler}} = \frac{\hbar\Gamma}{2k_B} \tag{1.4}$$

where Γ is the natural linewidth of the cooling transition and k_B is the Boltzmann constant.

The $^1S_0 \rightarrow ^1P_1$ transition is a dipole allowed transition at 461 nm. The natural linewidth of this transition, $\Gamma = 2\pi\times$ 32 MHz, is relatively broad, meaning it can scatter many photons quickly. This is useful for fast initial cooling of Sr, but is limited to a T_{Doppler} in the milliKelvin regime. This transition is useful for Zeeman slowing and a first stage magneto-optical trap (MOT). It is also commonly used to read out Sr state populations since it can scatter many photons that can be captured by fluorescence detectors. The $^1S_0 \rightarrow ^3P_1$ is a narrower ($\Gamma = 2\pi\times$7.6 kHz) singly-forbidden transition at 689 nm. This transition is used for secondary cooling of Sr down to $\approx$ 1 micro-Kelvin in a second MOT. From there, this cold strontium sample can be further confined and cooled, then ultimately serve as an atomic clock reference using the aforementioned clock transition.

1.4 Differential clock comparisons

^{87}Sr's clock transition is narrow enough for its width to not place the current limit on the precision of an atomic clock, as this limit is still technical and arises from the local

oscillator's instability. Most atomic clocks operate with a pulsed interrogation scheme, where there is some amount of averaging time where the local oscillator is not interrogating your atomic reference. This is due to the finite time required to prepare an atomic sample before interrogation, and then to read out the sample's state after interrogation. This so-called "dead time", t_d allows high frequency noise on the local oscillator to alias down into noise on the frequency measurement. This is aliased noise due to interleaved sampling is referred to as the Dick effect[18]. The Dick noise limit on clock stability for Ramsey spectroscopy is

$$\sigma_{\mathrm{Dick}}(\tau) = \frac{\sigma_{\mathrm{LO}}}{\sqrt{2\ln 2}} \sum_{m=1}^{\infty} \left| \frac{\sin(\pi m T/T_c)}{\pi m T/T_c} \right| \sqrt{\frac{T_c}{m\tau}}, \tag{1.5}$$

where σ_{LO} is the frequency instability of the local oscillator. There are a few ways to improve clock measurements when you are in this Dick-noise limited regime. Most straightforwardly, one can reduce the noise on the local oscillator, and much progress has been made recently to realize improved local oscillator noise, with state-of-the-art lasers referenced to cryogenic silicon cavities [47–51]. An alternative method is to run a clock with a continuous interrogation scheme, where the local oscillator is continuously referenced to the atomic transition and thus t_d=0[52, 53]. These types of experiments are currently quite technically challenging compared to traditional pulsed interrogation schemes, but are a promising direction to explore for clock performance improvement.

On the other hand, many of the proposed precision frequency measurements discussed in Section 1.1 rely not on measuring absolute frequencies or elapsed time, but on measuring frequency differences between clocks. Under this paradigm of differential measurements, clock comparisons done synchronously with the same local oscillator can take advantage of common-mode rejection of local oscillator noise. This technique has been successfully demonstrated in optical atomic clock systems including trapped ion clocks[54], 3D lattice clocks[55, 56], and tweezer clocks[57]. The best differential instabilities previously demonstrated on these platforms, $3 \times 10^{-17}/\sqrt{\tau}$[55–57], however, are comparable to the instability of their local oscillator, measured to be 4×10^{-17} at 1s.

1.5 Thesis outline

In this thesis, we demonstrate the novel application of synchronous differential frequency measurements to a 1D optical lattice clock with multiple spatially separated ensembles of ≈2000 ^{87}Sr atoms each, distributed across a 1 cm length scale. We clearly show the effectiveness of local oscillator noise rejection by demonstrating differential instabilities of $9.7 \times 10^{-18}/\sqrt{\tau}$ between two atomic ensembles using a commercial clock laser system with a measured instability of 1×10^{-15} at 1 second, see Section 2.7. In Chapter 3, we use this differential clock measurement technique to test the gravitational redshift predicted by general relativity at the centimeter to millimeter scale. After demonstrating that we are no longer limited by local oscillator-atom coherence, we can explore fundamental limits

to our differential comparisons, set ultimately by atom-atom coherence between ensembles. The natural limit to this coherence time is the lifetime of the excited clock state, which we measure using a direct decay method in Chapter 4. Finally, in Chapter 5, we apply an erasure conversion technique originally developed for use in quantum computing[58] to improve atomic coherence times by discriminating and rejecting atoms that wind up outside of our clock superposition subspace during coherent interrogation. We close with a brief discussion of upcoming experiments planned in our new lab space.

Chapter 2

Experimental setup

Portions of this chapter are adapted from Xin Zheng, Jonathan Dolde, Varun Lochab, Brett N. Merriman, Haoran Li, and Shimon Kolkowitz. "Differential clock comparisons with a multiplexed optical lattice clock". In: Nature *602.7897 (Feb. 2022), pp. 425–430. ISSN: 1476-4687. DOI: 10.1038/s41586-021-04344-y.*

2.1 Overview of the multiplexed optical lattice clock

In order to realize a multiplexed optical lattice clock based on strontium, we trap and cool Sr atoms through multiple stages within a vacuum chamber operating at $< 1.0 \times 10^{-11}$ mbar. The vacuum system is discussed in Section 2.2. Our strontium atoms are first heated to an operating temperature of 360° C in a commercially built Sr cold atom source. This source also includes optics for realizing a 2D Magneto-Optical Trap (MOT) and Zeeman slower based on the broad ($\Gamma = 2\pi\times$ 32 MHz) 461 nm $^1S_0 \rightarrow {}^1P_1$ transition in Sr, see Fig. 1.2. After these cooling stages, the Sr atoms are trapped in a 3D MOT based on the same 461 nm transition, detailed in Sections 2.4.1 and 2.4.2. This first 3D MOT stage is often referred to as the "blue" MOT in other works, this thesis, and in our lab. After cooling in the blue MOT to $\approx 1\ mK$, the atoms are transferred to a 3D MOT based on the narrower ($\Gamma = 2\pi\times$ 7.6 kHz) $^1S_0 \rightarrow {}^3P_1$ transition, cooling the atoms down to $\approx 1\ \mu K$, see Section 2.4.3. Unsurprisingly, this second-stage 3D MOT is referred to as the "red" MOT. Finally, a 1D, vertically-oriented optical lattice is overlapped with the red MOT, where atoms are stochastically loaded into the lattice potential, see Section 2.4.4. It is at this stage that we realize our multiplexed lattice, where we load multiple spatially separated atomic ensembles in order to measure the frequency differences between them. This spatial multiplexing is accomplished by detuning one arm of the lattice relative to the other, turning our standing wave potential into a running wave, pulling atoms out of the red MOT along the lattice axis. Once multiple ensembles are loaded in the lattice, further cooling and preparation steps are performed. After this, we interrogate the ultra-narrow ($\Gamma \approx 2\pi \times 1$ mHz) $^1S_0 \rightarrow {}^3P_0$ "clock" transition, see Section 2.4.5. After interrogation, atomic state population is read out using a 461 nm probe beam and our 679 & 707 nm repump beams. The relative populations of atoms in the $^1S_0$ and $^3P_0$ states

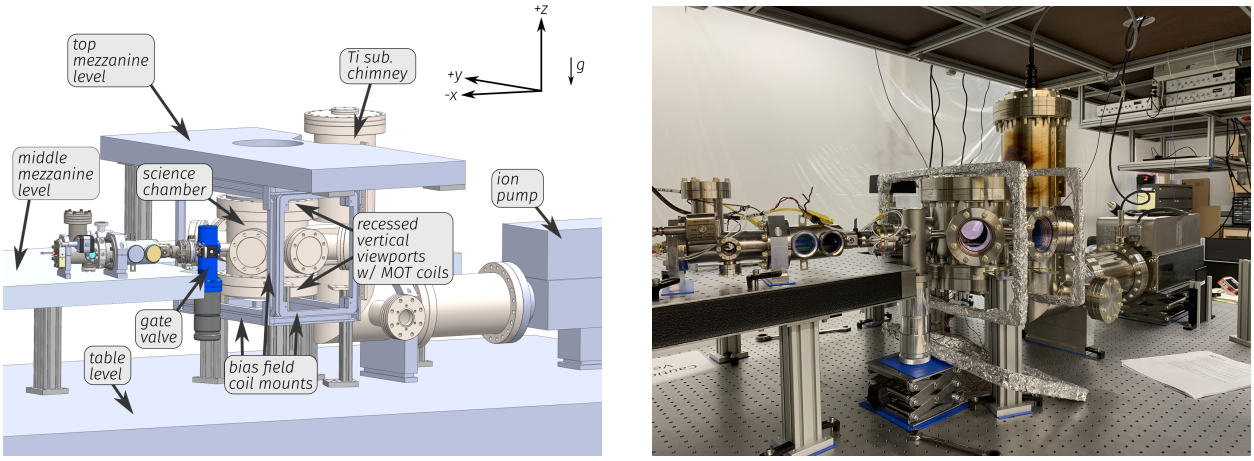


Figure 2.1: (Left) CAD model of our vacuum system and optical breadboard levels. Half of the middle mezzanine optical breadboard and associated supports are hidden to better show the vacuum system. (Right) Photo of our vacuum system after bake-out.

can then be used to extract the relative phase of pairs of atomic ensembles, which is then converted to a measured differential fractional frequency shift.

2.2 Vacuum system

Our vacuum system consists of a commercial cold strontium beam source (AOSense Beam-RevB-Sr) coupled to a custom-designed science chamber (based on a design from Aviv Keshet [60] and Sara Campbell [61]) through a gate valve and differential pumping tube. A CAD model of the vacuum system is shown in Fig. 2.1. The commercial cold strontium beam source integrates a strontium oven, ion pump, viewports and in-vacuum optics for 2D MOTs, and a permanent magnet and a heated viewport for Zeeman slowing. Our science region is a 316 stainless steel vacuum chamber (fabricated by Nor-Cal/Pfeiffer Vacuum) with 9 anti-reflection-coated fused-silica viewports (MPF Products) for laser and imaging access. The top and bottom viewports are both recessed "bucket" windows allow for our MOT coils to be placed about 6 cm from the center of our chamber. The science chamber is pumped by a 200L/s capacity ion pump (Gamma Vacuum TiTan). The integrated gauge on this pump reads the pressure inside the chamber to be below 1×10^{-11} mbar.

2.3 Magnetic field control

In order to form our MOT, we use a pair of magnetic field coils arranged in an anti-Helmholtz configuration such that we can realize a magnetic field gradient of up to 50 G/cm at the center of our vacuum chamber. These coils are formed by water-cooled hollow-core square

copper tubes. We use a 4 kW power supply (Magna-Power SL20-200/208+LXI) to source the current needed, up to 150 A at 13V for our maximum operating gradient. Precise current flow is measured with a pair of Hall probes, and their signal is fed to a current controller servo, which actuates the gate voltage of a high-power IGBT. A varistor is included to clamp voltage transients from the back-EMF of the coils' self-inductance when the current is switched. Finally, we have 5 thermocouples that monitor the temperature of the coils and the IGBT cooling plate. These temperature readings, along with flow meters in the MOT coil water-cooling loop, are combined into an interlock system that shuts down our power supply to prevent overheating of the coils.

We also use bias magnetic field coils to precisely control the magnetic field environment experienced by our atoms. There are three orthogonal pairs of Helmholtz configuration coils that correspond to the x, y, and z axes of our system. These coils are made of enameled copper wire, with about 50 turns each and an approximate loop area of 600 cm^2 per coil. Each loop has its own power supply and current control servo, where we can apply bi-directional current through each between -3.8 A and 3.8 A at 10 V, giving us a maximum applied bias field at our atoms of 6 G. We regularly use these coils to zero the magnetic field at the atoms, which we calibrate daily by minimizing the width of the $^1S_0 \rightarrow {}^3P_1$, F = 11/2 transition. During clock interrogation, these coils are used to apply a bias field of 5.5 G in the $\hat{x}$ direction (see Fig. 2.1), which allows us to frequency resolve specific $|g, m_F\rangle \rightarrow |e, m_{F'}\rangle$ clock transitions. When loading multiple ensembles, individual control of each loop, rather than just each pair, allows for applying magnetic field gradients across the atomic sample, letting us easily control their relative clock transition frequencies. Finally, when conducting some experiments, see Chapters 4 and 5, we used these coils to load multiple ensembles by moving the location of the field zero of our red MOT along the axis of the lattice.

2.4 Laser Systems

2.4.1 461 nm laser system

We start our laser cooling by addressing the $^1S_0 \rightarrow {}^1P_1$ transition with a wavelength of 461 nm. This cooling stage consists of a 2D MOT, Zeeman slower, and 3D MOT.

The commercial beam source we use provides in-vacuum optics and a permanent magnet to realize both of these initial cooling stages, only requiring user-provided 461 nm light. For the 2D MOT, we send in light that is detuned from resonance by -40 MHz, see Fig. 2.2 for our frequency chain, aligned to the in-vacuum optics. The two 2D MOT beams, see Fig. 2.13, are highly elliptical, with a 5mm x 25 mm beam diameter in vertical and horizontal directions, respectively. Both beams are circularly polarized, and the first 2D MOT beam has 12 mW of power, and the second has 6 mW, with their split controlled by a $\lambda/2$ waveplate and PBS. For the Zeeman slower, we send in light detuned from resonance by -550 MHz, aligned to both the center of the incident heated window and atomic oven aperture. This beam is collimated to about a 5 mm beam diameter with 30 mW of power, and is also circularly polarized.

The cooled atom beam moves through a small differential pumping tube into our main chamber. From there, we load our atoms into a "blue" 3D MOT addressing the 461 nm transition. The 3D MOT is formed by 3 retro-reflected beams detuned -40 MHz from resonance. Each 3D MOT beam arm has 10 mW of power, a beam waist of 1 cm, and is circularly polarized. The $^1S_0 \rightarrow {}^1P_1$ transition is not completely closed, with a branching ratio of $\approx 10^{-3}$ to $^1D_2$. From the $^1D_2$ state, atoms quickly decay into both the $^3P_1$ and $^3P_2$. Atoms that decay to $^3P_1$ quickly fall back to $^1S_0$ and can continue to cool, but atoms in $^3P_2$, with an estimated lifetime around 500s [62], are magnetically trapped but are no longer cooled by the 461 nm MOT beams. We therefore apply two so-called "repump" lasers during this 3D MOT stage that pump atoms from $^3P_2$ and $^3P_0$ to $^3S_1$, see Section 2.4.2 to redistribute atoms through the ^3P_J manifold. During a typical experiment, we load this 3D MOT stage for 400 ms, reaching atom numbers of around 1.5×10^6, estimated from light collected with a photomultiplier tube, and an atomic temperature of ≈1 mK. After this cooling stage, we transfer to a second 3D MOT based on the $^3P_1$ transition.

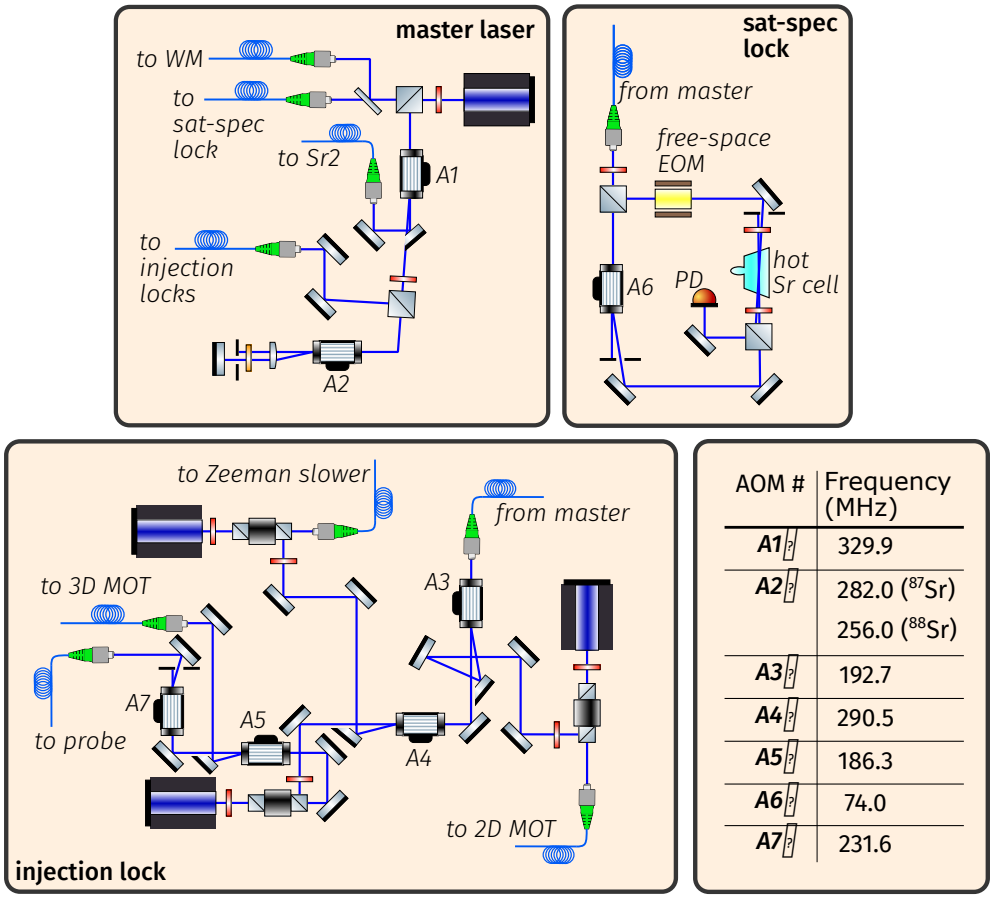
Our 461 nm light is generated by a Toptica DL Pro 461 nm diode laser locked to a home-built hot Sr spectroscopy cell, which seeds 3 injection-locked laser diodes (Nichia NDB4216 100mW) and driven by 3 combined temperature/current controllers (Arroyo ComboPak, 500mA/10V). The injection lock diode currents are not actively stabilized. Instead, we scan each diode's current over an approximate 3 mA range and set it to the value that maximizes the monitor photodiode signal. This setup is shown in Fig. 2.2.

2.4.2 679 & 707 nm laser system

Repump lasers are required to address the $^3P_0$ and $^3P_2$ to $^3S_1$ transitions for two purposes.

First, as previously discussed in Section 2.4.1, these lasers ensure that atoms do not become trapped up in dark states during our first stage blue 3D MOT. Atom numbers in the blue MOT are increased by approximately two orders of magnitude when these lasers are on during MOT operation. The source of both the 679 nm ($^3P_0 \rightarrow {}^3S_1$) and 707 nm ($^3P_2 \rightarrow {}^3S_1$) light are MOGLabs ECDLs, one for each respective transition, see Fig. 2.3. Both of these lasers are free-running, and in order to address the entire hyperfine manifold of the $^3P_2$ state, we modulate the 707 nm laser's PZT control across 423.905-423.919 THz [63]. We also modulate the 679 nm in a similar manner (across 441.329-441.334 THz) to ensure that we can still address the transition if our free-running laser drifts over time. We are also planning to eventually lock both repumps to a frequency comb (Menlo ULN 1550) referenced to our clock system's ULE cavity, which should obviate the need to scan our 679 nm laser. In order to address the hyperfine manifold transitions for $^3P_2 \rightarrow {}^3S_1$, we will use a fiber EOM driven by multiple RF tones instead of scanning.

The second use of these repump lasers is for our imaging step, where to read out our excited clock state ($^3P_0$), we incoherently pump atoms out of $^3P_0$ into $^3S_1$, which quickly decays back into the ^3P_J manifold. Atoms that arrive back in $^3P_0$ and $^3P_2$ are repumped back up to $^3S_1$ with the 679 nm and 707 nm respectively, and atoms that decay into $^3P_1$ quickly



AOM #	Frequency (MHz)
A1	329.9
A2	282.0 (^{87}Sr)
	256.0 (^{88}Sr)
A3	192.7
A4	290.5
A5	186.3
A6	74.0
A7	231.6

Laser Beam	Frequency Chain	Offset from 88Sr 1S0-1P1 for 87Sr (88Sr) [MHz]	Offset from MD for 87Sr (88Sr) [MHz]
Master Diode (MD)	88Sr 1S0-1P1 - **A6**/2	-37.0	0
2D MOT	MD + **A1** - 2*__A2__ + **A3**	-76.4 (-26.4)	-41.4 (+10.6)
Zeeman Slower	MD + **A1** - 2*__A2__ - **A4**	-561.6 (-509.6)	-524.6 (-472.6)
3D MOT	MD + **A1** - 2*__A2__ + **A5**	-84.8 (-32.8)	-47.8 (+4.2)
Probe	MD + **A1** - 2*__A2__ + **A7**	-39.4 (+12.5)	-2.5 (+49.5)

Figure 2.2: Diagram of our 461 nm laser system, broken down into three subsystems, along with a frequency chain. The master laser system includes our main EDCL and frequency control for switching between ^{87}Sr and ^{88}Sr. The saturation-absorption spectroscopy lock system is used for keeping our main ECDL's frequency locked to Sr's $^1S_0 \rightarrow {}^1P_1$ transition through feedback to its current and piezo modulation ports. The injection locking system is used for increased power and MHz-level control for each 461 nm beam on the experiment table, including the 2D MOTs, Zeeman slower, 3D MOT, and probe. We show each beam's frequency calculation relative to the master diode (MD) frequency (650 503.81 GHz), which is locked to ^{88}Sr $^1S_0 \rightarrow {}^1P_1$ transition with a saturation absorption spectroscopy lock, see Fig. 2.2. In order trap ^{88}Sr, we detune AOM A2 by -26 MHz to make up the +52 MHz isotope shift of ^{88}Sr relative to ^{87}Sr.

decay into the ground clock state $^1S_0$, where we use fluorescence imaging on the $^1S_0 \rightarrow {}^1P_1$ to detect atom population. This scheme is discussed further in Section 2.5.

Each repump beam is about 3 mW of power, with a beam waist of 7 mm, and is split evenly across the 3 MOT arm paths, following the 689 nm path and overlapped with the blue MOT beams using dichroic mirrors, see Fig. 2.11.

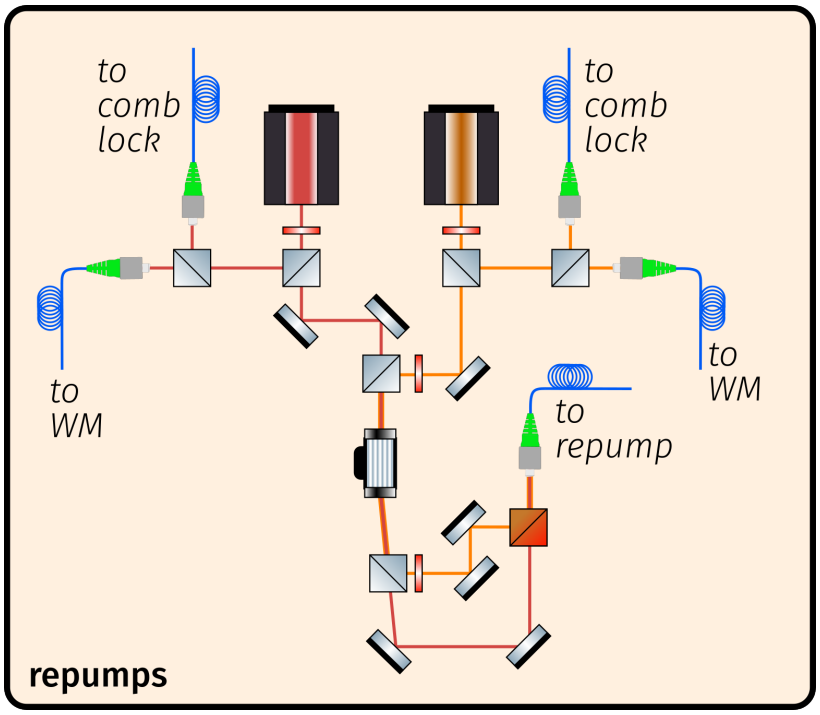


Figure 2.3: Diagram of our 679 & 707 nm "repump" laser system. Both lasers are free-running, and scanned across an ≈6 GHz range through their piezo modulation input. These beams don't require fast independent control, so we use a single AOM for both beams.

2.4.3 689 nm laser system

Once cooled by the initial blue 3D MOT, we further cool our atoms in a second "red" 3D MOT addressing the narrower $^1S_0 \rightarrow {}^3P_1$ transition, at 689 nm with a linewidth of $\Gamma = 2\pi \times$ 7.6 kHz. This stage allows for much colder Doppler-limited temperatures than our blue MOT, with final cooling temperatures of ≈ 1-2 μK. We use a MOGLabs ECDL to generate the required 689 nm light, which we PDH lock to a high-finesse ($F \approx 15,000$) ULE cavity (Stable Laser Systems) (not to be confused with the clock cavity, we use a separate cavity for 689 nm locking), see Fig. 2.4. We then use this ECDL to seed an injection lock to a high power diode (MOGLabs ILA), which we split into light for our 3D red MOT and axial and radial cooling beams, which are used during our in-lattice cooling stage, see Section 2.4.4. In ^{87}Sr,

we address the $^3P_1$, F = 11/2 state for our MOT, and we also require a "stirring beam" that pumps atoms in the poorly-trapped low $|m_F|$ states towards the better trapped stretched $|m_F| = 9/2$ state [64]. This stirring beam addresses $^3P_1$, F = 9/2 and is offset from our $^3P_1$, F = 11/2 MOT light by +1463.35 MHz. To realize this beam, we use a second MOGLabs ECDL that is offset phase locked to the 3D MOT light, see Fig. 2.4.

The red MOT beam, stirring beam, and repump beams are overlapped on the experiment table, and split into 3 arms that are overlapped with the blue MOT beams using dichroic mirrors. All the red beams have approximately the same beam waist of 7mm.

The red MOT sequence consists of two stages. We start with a broadband stage where we modulate the red laser light and have a relatively low magnetic field gradient of 3 G/cm in order to address as large of a velocity range as possible such that as many atoms as possible can be transferred from the blue MOT to the red MOT. We modulate the frequency during this stage by modulating the drive frequency to our double pass AOM with a 200 kHz triangle wave with an amplitude corresponding to a modulation depth of 2MHz (4 MHz total modulation at the atoms), allowing for a velocity capture range matching our blue MOT velocity profile.

Once our atoms are transferred from our blue MOT to our red broadband MOT, we then ramp our laser frequency modulation, laser amplitude, and magnetic field gradient over the span of 200 ms to obtain a cold, dense, atomic sample of about 250k atoms at 1.5 μK. We ramp our frequency modulation depth from 2 MHz to 0 during this stage, ramp our red MOT and stirring beam power from 15 mW and 6 mW of respective total power to 50μW, and our magnetic field gradient from 3 G/cm to 10 G/cm. Once the ramping is finished, we can load our atoms into our magic wavelength 1D optical lattice.

2.4.4 813 nm laser system

Our final trapping stage is a 1D, vertically oriented, magic wavelength optical lattice. This trap has quickly become the best performing way to realize a high precision optical clock [65–68], as it is ultimately a very simple and well-understood potential. The trapping potential arises from AC Stark interactions shifting the electronic energy levels of an atom such that the atom experiences an attractive (red-detuned) or repulsive (blue-detuned) force from the trap light.

$$\Delta E = \frac{1}{2}\alpha(\omega)\langle E^2\rangle \tag{2.1}$$

where the energy shift ΔE is determined by the dynamic polarizability α for light at frequency ω and with average electric field magnitude $\langle E\rangle$. In a 1D optical lattice, the trapping light consists of two counter-propagating, Gaussian TEM_{00} beams, in our system this is accomplished by retro-reflecting a single beam back over itself. The trapping potential in this setup looks like

$$U(r,z) = 4U_0\, e^{-2r^2/w(z)^2} \cos^2\left(\frac{2\pi z}{\lambda_L}\right) \tag{2.2}$$

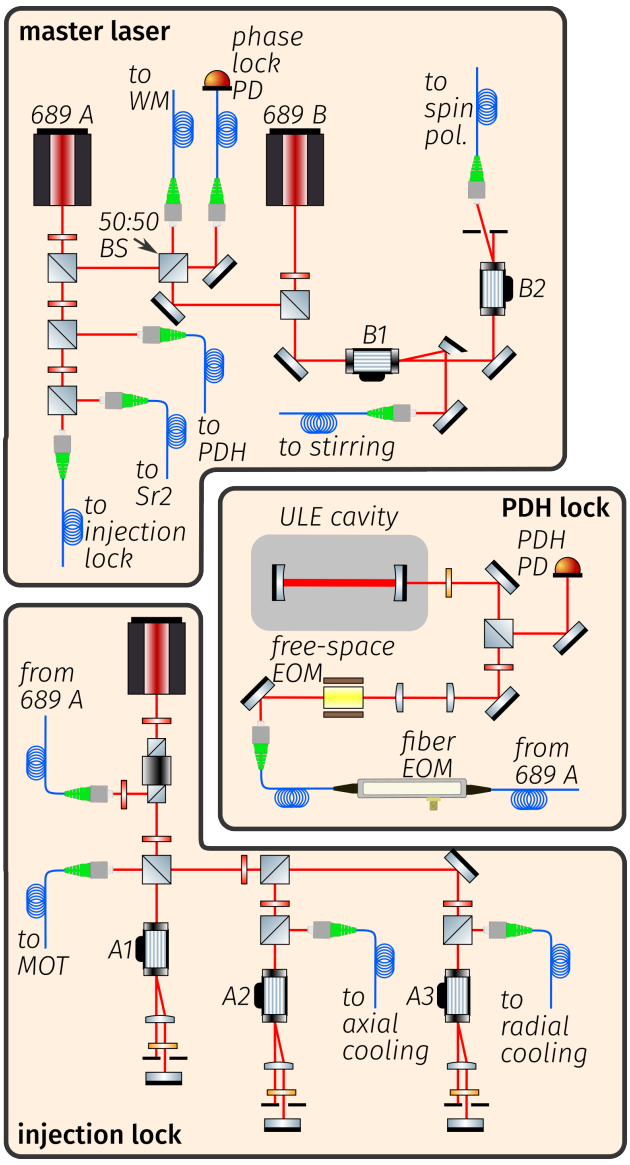


Figure 2.4: Diagram of our 689 nm laser system, broken down into three subsystems. Our main ECDLs are shown in the master laser subsystem. The 689 A diode is locked to our red 3D MOT transition, and the 689 B diode is offset phase-locked to 689 A for our stirring and spin polarization beams. The PDH subsystem is responsible for our frequency locking for 689 A diode, the fiber EOM in the path allows us to span the ULE cavity's FSR for locking to an arbitrary wavelength. Our injection lock subsystem allows for increased power in our 3D MOT path, as well as providing the frequency control for the MOT, axial cooling, and radial cooling.

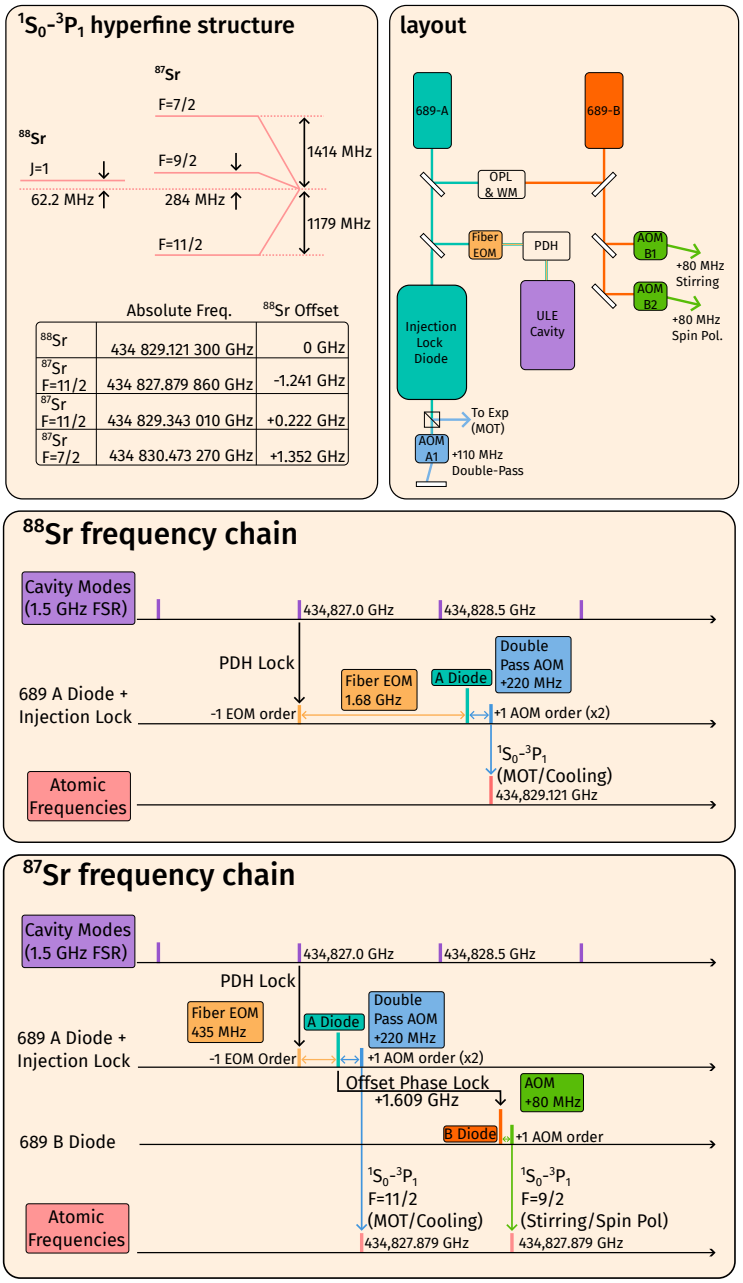


Figure 2.5: 689 nm laser frequency chain for our red MOT. In order to address the desired $^1S_0 \rightarrow ^3P_1$ transitions, we use a ULE cavity to serve as a stable frequency reference for our laser, then use a fiber EOM and additional AOMs to bridge the frequency between our cavity modes and the atomic transition frequency. For ^{88}Sr, we only need a MOT beam and cooling beams addressing the $^3P_1$, F=11/2 transition. For ^{87}Sr, we need an additional "stirring" beam addressing the $^3P_1$, F=9/2 transition in addition to the F=11/2 MOT and cooling beams. See Fig. 2.4 for a more detailed optical layout

where $U_0 = P\alpha(\omega)/(\pi c\epsilon_0 w(z)^2)$ for a laser of power P, beam waist of $w(z)$ where z is axial distance from the minimum waist, w_0, r is radial distance from the beam center, and $\lambda_L = 2\pi c/\omega$ is the lattice wavelength [69]. This separability of the axial and radial potentials gives us access to an axis where the atoms are strongly confined and their motion along this axis is quantized. In this strong-confinement regime along the lattice, the spacing of the motional states should be much larger than recoil energy of a single interrogation photon, i.e. photons from our clock laser, such that the motional and internal degrees of freedom of the atom are uncoupled. This condition is called the Lamb-Dicke regime, with the condition

$$\eta^2(2n+1) \ll 1 \tag{2.3}$$

where η is the Lamb-Dicke parameter, defined as

$$\eta \equiv k_{clock}\sqrt{\frac{\hbar}{2m\omega_z}} \tag{2.4}$$

where k_{clock} is the wave-vector of our clock laser, ω_z is the trap frequency of our 1D lattice, given by expansion of the $\cos^2$ term in Eq. (2.2)

$$\omega_z = \sqrt{\frac{2U_0 k_L}{m}} \tag{2.5}$$

where $k_L = 2\pi/\lambda_L$ the magnitude of the trap wavevector along the strongly confined axis, and m is the mass of the atom, either ^{87}Sr or ^{88}Sr in our system. The strength of this confinement, U_0, referred to as trap depth, is often quoted in units of $E_{\text{rec}} \equiv \hbar^2 k_L^2/(2m)$.

The magic condition of our optical lattice is realized when the dynamic polarizability of the ground and excited clock states are equal, meaning to first order the AC Stark shift of the clock transition is zero as both levels shift the same amount in response to a given trapping light intensity. In our system, we measure the operational magic wavelength of the $|g, m_F = \pm 5/2\rangle \rightarrow |e, m_F = \pm 3/2\rangle$ transition to be 368,554.810(30) GHz by examining how quickly the trap-limited atomic coherence decays at varying trap wavelengths, see Fig. 2.6. Evaluating the full contribution of the AC Stark shift measurements is detailed in Section 3.3.5.

To generate our 813 nm light, we use a titanium-sapphire laser (Sirah Matisse CX) with an integrated 532 nm diode-pumped solid state laser (Sirah Millennia 25W). This laser system has an integrated PDH locking scheme, pushing the instantaneous linewidth of the laser below 20 kHz. However, we see large thermal drift in the integrated reference cavity, so we also run a digital lock to our wavemeter (HighFinesse WS7), which has a frequency resolution of 1 MHz. We measure 6.5 W of power output at 813 nm from the aperture of this system. The optical path of our 813 nm lattice is detailed in Fig. 2.8 and Fig. 2.11. Our lattice is formed with an incoming power of about 1.5 W, with a beam waist of 120 μm and an approximate Rayleigh range of 5 cm.

In order to load multiple spatially separated ensembles along the lattice axis (oriented vertically against gravity to suppress site-to-site tunneling [70]), we place two AOMs in the

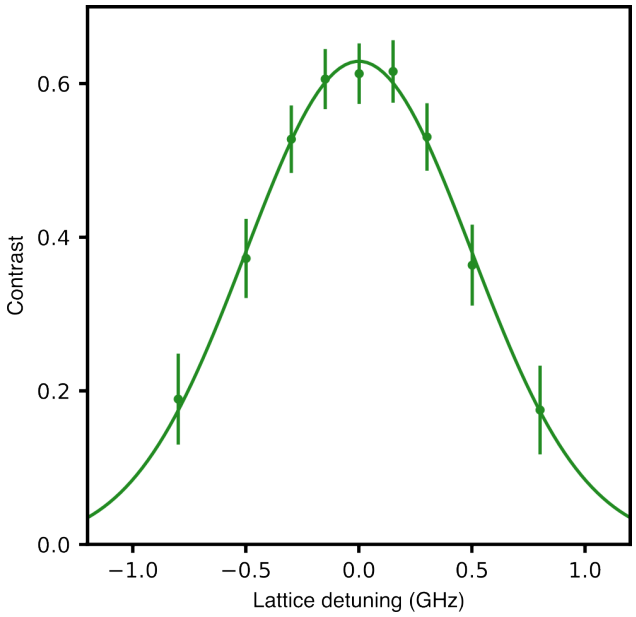


Figure 2.6: Measurement of the operational magic wavelength of the $|g, m_F = \pm 5/2\rangle \rightarrow |e, m_F = \pm 3/2\rangle$ transition. We use a Gaussian fit to extract an operational magic wavelength of 368,554.810(30) GHz. The contrast is measured with our synchronous Ramsey interrogation method at 20 E_{rec}trap depth and 10s interrogation time.

retro reflected path of our lattice, along with a cat's-eye lens setup between our final AOM and retro mirror. Through controlling the drive frequencies of these AOMs, we can control the detuning of the lattice incoming and retro-reflecting paths, turning the standing wave potential into a running wave potential, allowing us to accelerate the atoms trapped in the lattice. The cat's-eye setup ensures that this AOM frequency shift doesn't affect the pointing of the retro-reflected beam during acceleration.

The lattice velocity is explicitly given in Eq. (2.6) in terms of $\delta\nu_L$, the detuning of the drive frequency of the AOM closest to the retro-reflecting mirror and the lattice wavelength, λ_L.

$$v = \frac{1}{2}\lambda_L \delta\nu_L \tag{2.6}$$

The acceleration induced is therefore given by

$$a = \frac{1}{2}\lambda_L \frac{\partial \delta\nu_L}{\partial t} \tag{2.7}$$

The maximal acceleration we can apply is limited by how the atoms are heated during acceleration compared to the operational lattice depth. During normal loading operation, we apply a maximum acceleration of 280 m/s^2 for up to 2 ms at a time. In our experiment, we use two phase-synchronized DDSs and integrated amplifiers to drive the two retro path

AOMs at 110 MHz. A complete timing diagram of our lattice acceleration for loading two ensembles is shown in Fig. 2.7. For loading more than two ensembles, we apply repeated detuning ramps, allowing us to load up to 6 ensembles across 1 cm, limited by the spatial resolution and binning of our EMCCD, see Section 2.5.

Our lattice trap depth is calibrated daily by measuring the axial sideband profile of the clock transition of atoms trapped in the lattice at various lattice intensities, see Section 2.4.5 for details about the axial sideband profile measurement. We use a photodetector on the experiment table to operate an intensity noise servo by modulating the drive power to the lattice AOM on the auxiliary optical table, shown in Fig. 2.8, also allowing us to set the desired trap depth through the setpoint of this servo.

2.4.5 698 nm laser system

Our clock laser system is based on a commercial, rack-mounted, laser and locking system (Menlo ORS). This system integrates an ECDL (MOGlabs ECDL) and laser controller (MOGlabs DLC), an ultra high finesse ULE cavity ($F = 330,000$) and vacuum system, and optics and control electronics for PDH locking, Doppler phase noise cancellation, and fiber coupling to a user path. The laser system's optical layout is summarized in Fig. 2.9. This laser system has a quoted flicker noise floor at the 1×10^{-15} level, 2 orders of magnitude worse than current state-of-the-art lasers locked to cryogenic silicon cavities [55, 57, 71].

At the experiment table, we have 8 mW of 698 nm light that is sent through an AOM that is responsible for the frequency control and intensity servoing of our clock light. The beam path is detailed in Fig. 2.11. The +1 order of the AOM is what is ultimately directed to the Sr atoms, while the 0 order of the AOM is retro-reflected off of a mirror epoxied to the mount of the lattice retro-reflecting mirror and back coupled through the clock fiber to the Doppler cancellation module on the clock laser rack. The intensity of the clock laser at the atoms is controlled both through an intensity servo modulating the drive power of the aforementioned AOM and through the use of a motorized ND filter wheel in the clock path (Thorlabs FW2AND). The approximate beam waist of the clock laser at the atoms is 6 mm, ensuring spatial homogeneity of the beam across the atomic ensembles. The clock's beam position is monitored on the top mezzanine of the experimental table with a CMOS camera.

We use our clock laser to drive both $\pm\sigma$ and π transitions through either overlapping the clock and lattice beams using a PBS (driving $\pm\sigma$ transitions), or a dichroic beam splitter (driving π transitions). During standard operation, we address the $|g, m_F = \pm 5/2\rangle \rightarrow |e, m_F = \pm 3/2\rangle$ clock transition, which is frequency resolved from other $m_F \rightarrow m_{F'}$ transitions by applying a 5.5G magnetic field perpendicular to the clock beam's $\hat{k}$ and polarization axis.

2.5 Readout

In order to measure the phase of our atomic ensembles, we measure the relative populations of atoms in the excited clock state compared to the ground state at the end of our Ramsey

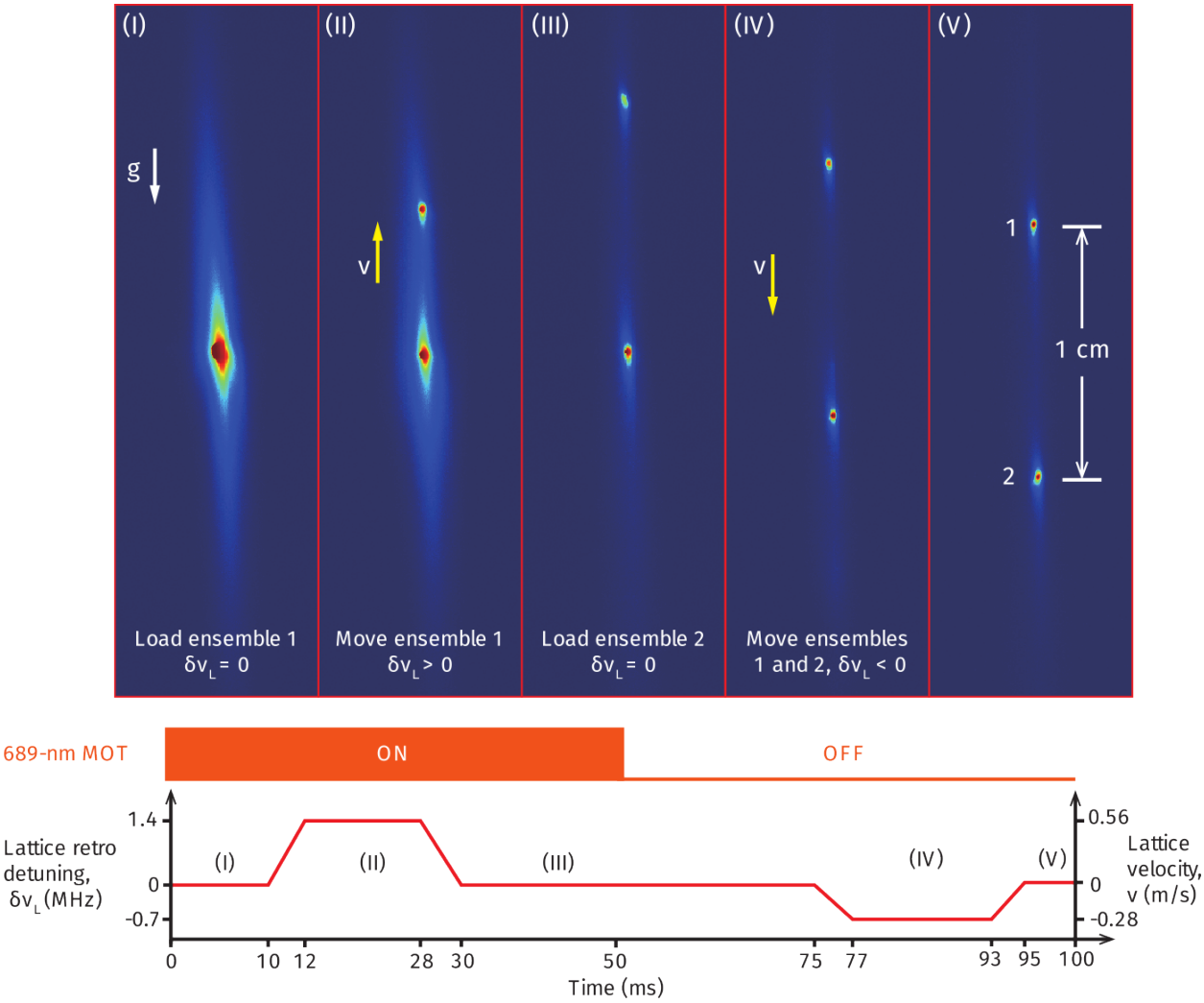


Figure 2.7: EMCCD images and timing diagram of lattice retro-reflected beam frequency when loading 2 spatially separated ensembles. In order to load multiple atomic ensembles, the retro-reflected beam of our 1D optical lattice is detuned relative to the incoming beam through the frequency control of two double-pass AOMs. Stage I is the single-frequency red MOT overlapped with the static optical lattice with zero retro detuning. Stage II is the initial vertical (+**z**) displacement of ensemble 1 by applying a positive relative detuning of the retro beam. Stage III is loading the second ensemble into the static lattice. Stage IV is the second moving stage, where both ensembles are shifted downwards (-**z**) such that they displaced symmetrically from the lattice beam waist. Stage V is the state of the two ensembles after the multi-loading procedure, where they are separated by 1 cm vertically.

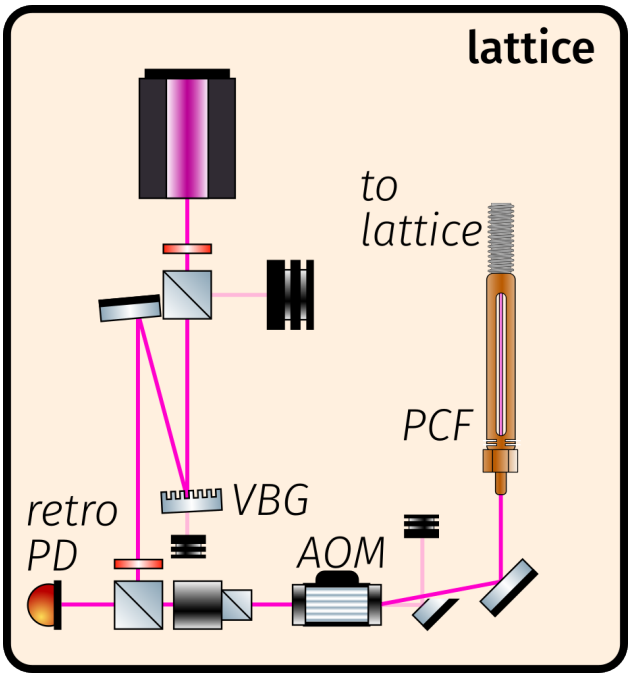


Figure 2.8: Diagram of our 813 nm lattice laser system. The main consideration in this subsystem is high power NIR light handling, and we use a specialized photonic crystal fiber (PCF) with a high-power connector (NKT HP LMA-10) to mitigate the effects of Brillioun scattering in our fiber connection to the experiment table. We monitor power that is retro-reflected from the experiment table and coupled back through the fiber in order to measure how well our incoming and retro-reflected lattice arms are overlapped. The AOM in this setup is responsible for servoing our lattice laser's intensity at the experiment table. Additionally, we use a volume Bragg grating (VBG) to help to clean up our laser's frequency profile.

interrogation sequence. In order to measure these populations, we use a two-stage imaging process, where atoms in the ground state are first imaged destructively, then excited state atoms are pumped incoherently into the ground state through the use of two repump lasers, then finally this new ground state population is read out with the same imaging pulse.

We perform fluorescence imaging on the broad $^1S_0 \rightarrow {}^1P_1$ state with a collimated 461 nm probe beam with a 0.5 mm beam waist directed along the optical lattice axis. This probe beam is on resonance with the transition with a 25 μs exposure time. This fluorescence is collected on a cooled EMCCD (Andor iXon 888), see Fig. 2.12. We then convert these counts into atom numbers through our calibration procedure detailed below.

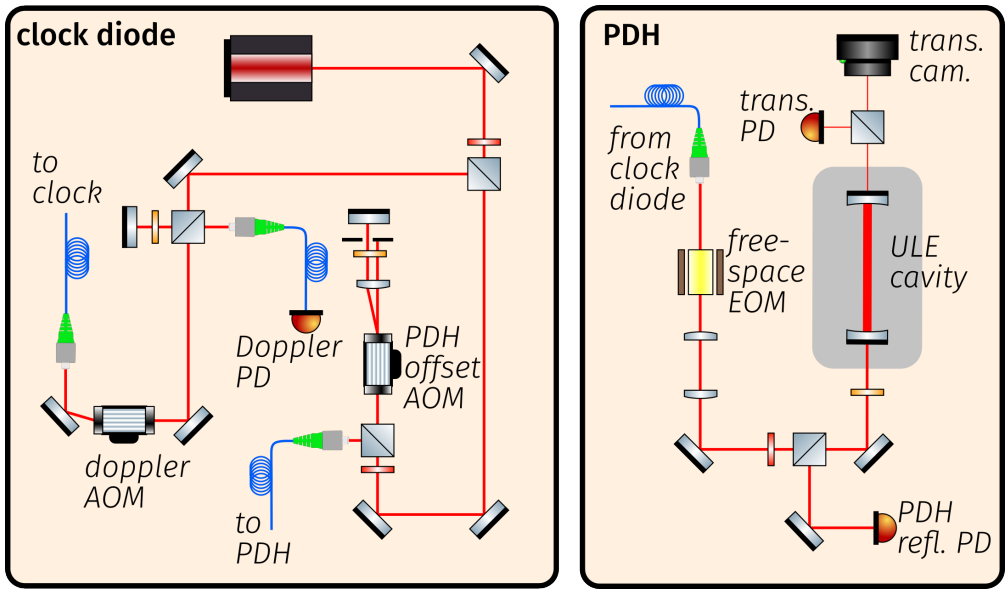


Figure 2.9: Diagram of our clock laser system, broken up into two subsystems. The first subsystem consists of the clock ECDL, an AOM for controlling the frequency offset of the PDH system, and an AOM and optics for Doppler phase noise cancellation, which is referenced to our lattice retro-reflection mirror, see Fig. 2.11. The other subsystem is the PDH lock to a high-finesse ($\approx$ 330,000) ULE cavity for short-term laser stability. Both of these subsystems are in a commercial rack-mounted package from Menlo systems.

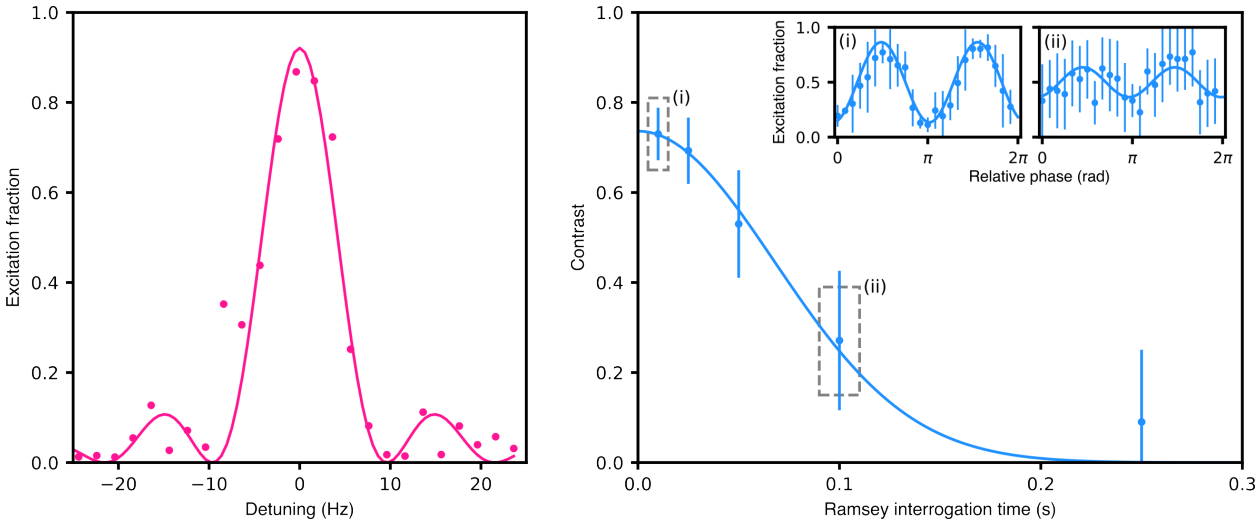


Figure 2.10: (Left) Rabi spectroscopy of a single ensemble with 90 ms π pulse duration (pink points) taken with one measurement without averaging. The fit gives a linewidth of 10.2(4) Hz (pink line). (Right) Decay of Ramsey contrast taken with one ensemble. This is fitted to a Gaussian envelope, which gives an atom–laser coherence time of 96(24) ms. Insets: Ramsey fringes at 10 (i) and 100 ms (ii) interrogation times.

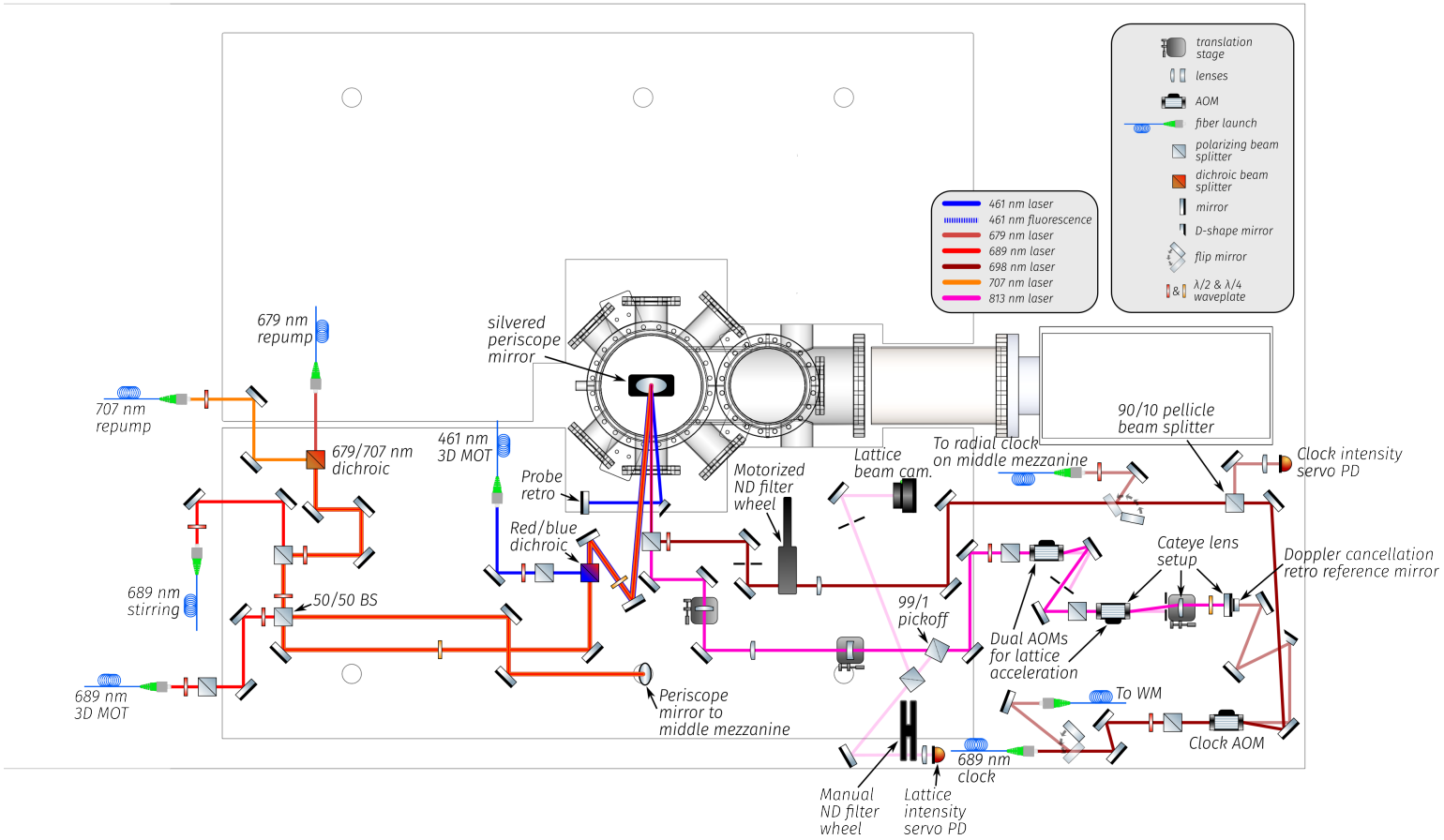


Figure 2.11: Diagram of our experiment table laser system, at the table surface level. Here we launch our vertical 461 nm MOT arm, our 679 & 707 nm repump beams, 689 nm 3D MOT beams, and 698 nm clock beam. This is also the level where we do all frequency control of the retro-reflected light for our optical lattice, which is how we accelerate our atoms to load multiple spatially separated atomic ensembles. We also use photodetectors (PD) to servo both the lattice and clock beam powers. There is also a fiber connection for our clock in order to probe our ensembles radially, shown in Fig. 2.12.

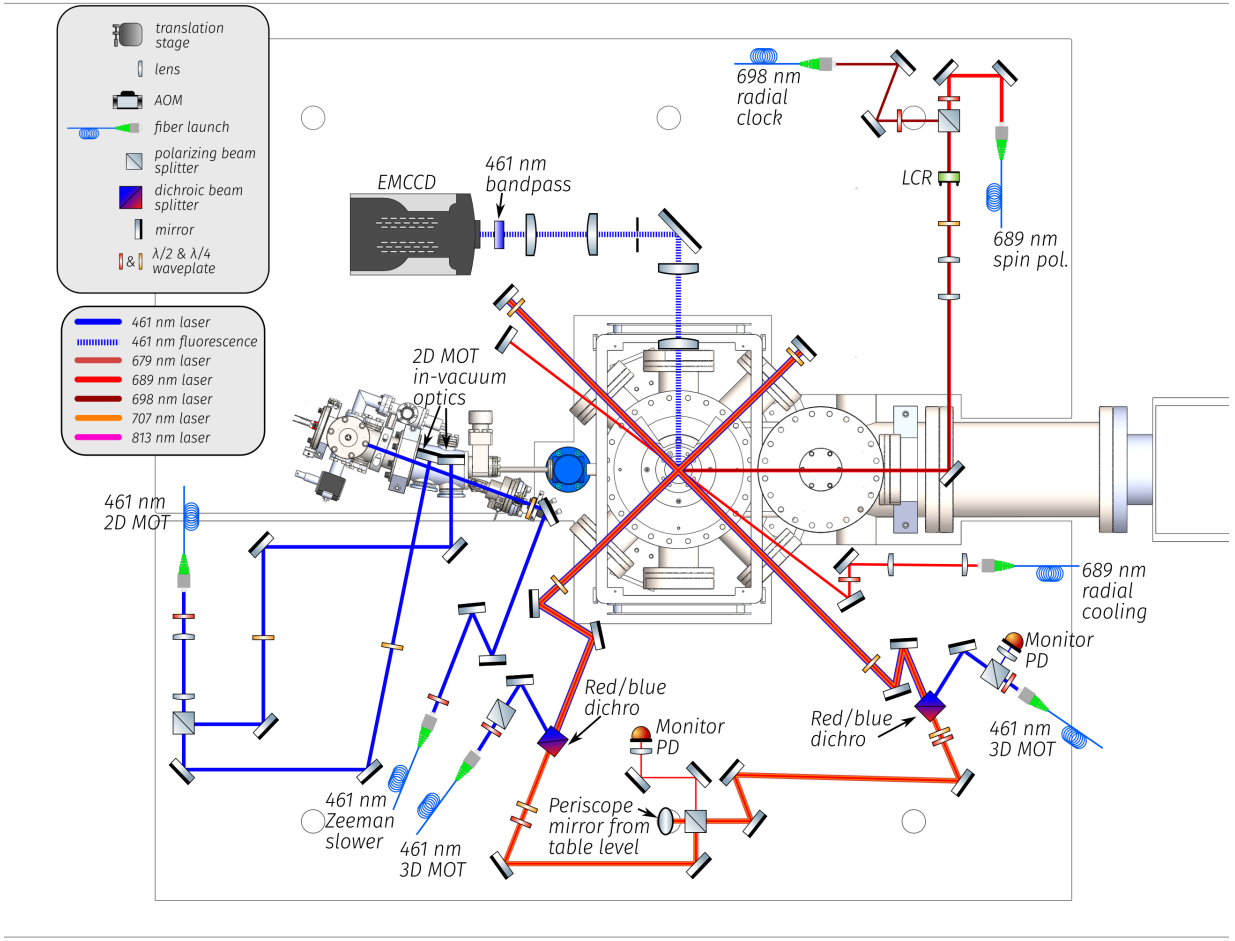


Figure 2.12: Diagram of our experiment table laser system, at the middle mezzanine level. Here we launch our 2D MOTs beam, Zeeman slower beam, 2 horizontal arms of the 461 nm 3D MOT, radial cooling beam, spin polarization beam, and radial clock beam. This is the level we also have our imaging system at, where we collect fluorescence photons from our atomic samples on an EMCCD. We also direct the horizontal arms for the 689 nm 3D MOT and repumps here, coming from a periscope mirror on the table-level setup.

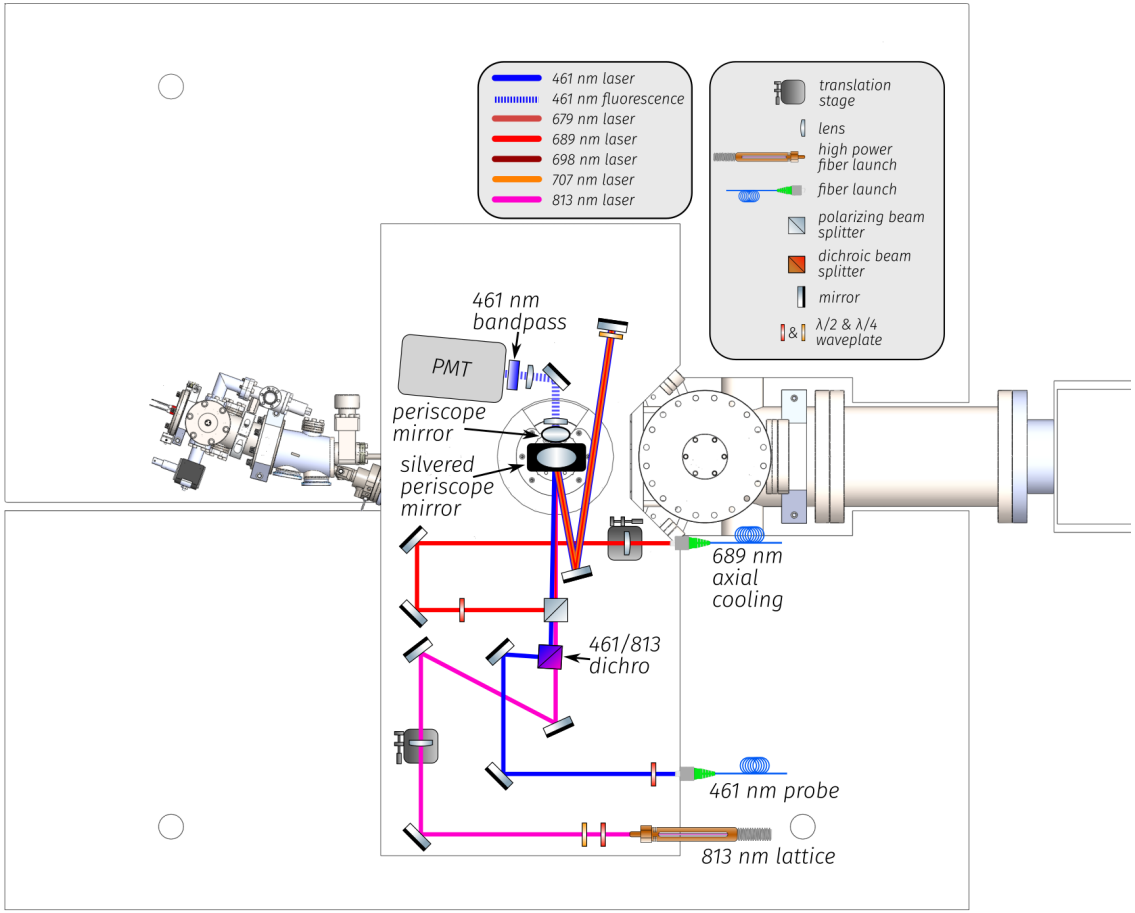


Figure 2.13: Diagram of our experiment table laser system, at the top mezzanine level. Here we launch our 813 nm optical lattice beam, 689 nm axial cooling beam, and 461 nm probe beam. Here we also use a PMT to monitor fluorescence from our 461 nm MOT, a helpful diagnostic parameter in the lab.

2.5.1 Calibration procedure

In order to get an estimate of our atom number, we first calibrate the atom number using a photo-multiplier tube (PMT), which we can then confirm is consistent with a calibration of atom number using quantum projection noise (QPN).

To use the PMT to calibrate our atoms, we note that the number of atoms in the blue MOT will be given by the number of photons detected times the inverse collection efficiency times the number of photons emitted per atom, giving

$$N_{\text{blueMOT}} = N_{\gamma\ \text{det}} \times \epsilon^{-1} \times N_{\gamma\ \text{per atom}} = N_{\gamma\ \text{det}} \times \frac{1}{f \times \text{optics loss}} \times \frac{1}{A\ \rho_{exc}} \tag{2.8}$$

where $N_{\gamma\ \text{det}}$ is the number of photons detected on our PMT, ϵ is our collection efficiency, f is the solid angle fraction of our PMT system, optical loss is our estimated loss from our imaging path optics, $N_{\gamma\ \text{per atom}}$ is the number of photons emitted per atom, A is the radiative decay rate of the $^1\text{P}_1$ state, and ρ_{exc} is the fraction of time spent in the excited state. ρ_{exc} is estimated by blocking the repump beams during a steady-state blue MOT, causing the fluorescence to decay based on the known branching ratio between the decay from $^1\text{P}_1$ to $^1\text{S}_0$ vs $^1\text{P}_1$ to $^1\text{D}_2$. Our measured decay time, τ, is 10.53 ms, which gives us an estimate of ρ_{exc} through $\tau = 1/\text{R} = 1/(A_{^1D_2} * (1/3))\ \rho_{exc}$ where $A_{^1D_2} = 3.9 \times 10^3\ \text{s}^{-1}$, and the 1/3 comes from the branching ratio of $^1\text{D}_2$ to $^3\text{P}_2$. Our PMT imaging path uses a 50.8 mm diameter lens positioned approximately 19.5 cm away from out atomic sample, giving us an NA of 0.13, allows us to capture about f $\approx \pi\ \text{NA}^2 \approx 0.5\%$ of the total photons scattered by our atoms. Our optical losses are estimated to be $0.96^4\times$ 0.9 to account for a 96% efficiency for a viewport, two lenses, and one mirror, and 90% efficiency for our 461 nm band-pass filter on the PMT. We can put this all together, and use the known photons-to-voltage conversion of our PMT at it's operational gain to get an estimate of 1.6×10^6 atoms in our blue MOT per one Volt of PMT signal. We can then use this voltage signal to estimate the counts for the red MOT by simply comparing the height of the blue MOT signal with a now known number of atoms to the height of the red MOT signal when imaged with our 3D MOT beams. This can then be calibrated to match the pixel count to atom number calibration for our EMCCD path. This ultimately gives us a conversion factor of about 5 pixel counts per atom per EM gain on our EMCCD for a 25 μs exposure with our on-resonant probe beam.

We can then confirm this calibration by measuring the quantum projection noise (QPN) made from measurements using our clock laser. By varying both the excitation fraction using Rabi pulses of different times and the atom number by purposely loading more or less atoms, we can check that this calibration value agrees with the expected QPN for a given number of atoms.

Additionally, we must ensure that any spatial gradients in collection efficiency don't affect our atom number calibration when we load multiple ensembles. The spatial gradient arises both due to inhomogeneities in the fluorescence collection along the vertical axis, and pixel-to-pixel quantum efficiency variation across the EMCCD sensor. To calibrate this, we move an ensemble of atoms with a constant 1.5 m/s velocity across an $\approx$ 1.5 cm spatial

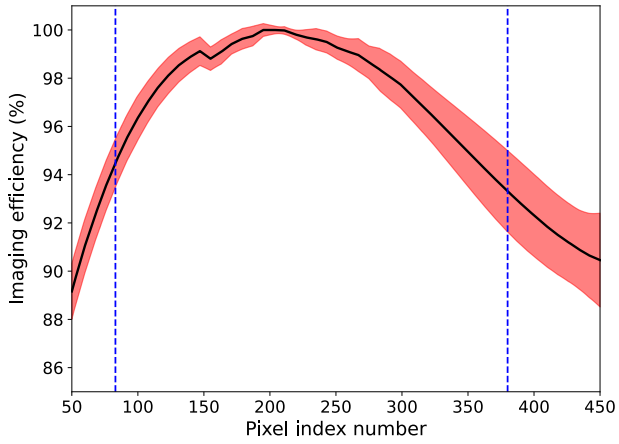


Figure 2.14: Imaging efficiency of our system across the distance our atoms are moved. The black line is the averaged normalized imaging efficiency, with the red region representing the 1σ standard deviation of the averaging. The vertical dashed lines indicate the pixel positions of the center of a pair of ensembles loaded 1 cm apart.

extent corresponding to a 500 pixel region on our EMCCD. We do this movement in <100 ms such that atom loss during this stage is negligible given our ground state lifetime is >20 s. We determine the center and amplitude of the atomic cloud in pixels by fitting to our images with a Gaussian profile. An average of 10 repeated measurements are taken to map out the imaging gradient. A Savitzky-Golay filter is then applied to smooth out the normalized imaging efficiency curve, [72] which is used to post-calibrate our data from a raw EMCCD fluorescence image. A typical calibration curve with 10 averages is shown in Fig. 2.14.

Once we have the population in the ground state measured and cleared from the trap, we now shine our 679 and 707 nm repump lasers for 10 ms to drive all population in the excited state down to the ground state. We repeat the same imaging procedure, then take one more image to serve as a background reference. Finally, our excitation fraction is calculated as

$$P_i = \frac{N_{e,i} - N_{bg,i}}{N_{e,i} + N_{g,i} - 2N_{bg,i}} \tag{2.9}$$

where N_g is the calibrated ground state population measured from the first imaging pulse, N_e is the calibrated excited state population from the second imaging pulse, and N_{bg} is the calibrated background, and the index i enumerates the ensemble being imaged.

2.6 General experimental sequence

In this section, we discuss a typical experimental sequence to make differential frequency measurements in our multiplexed clock system.

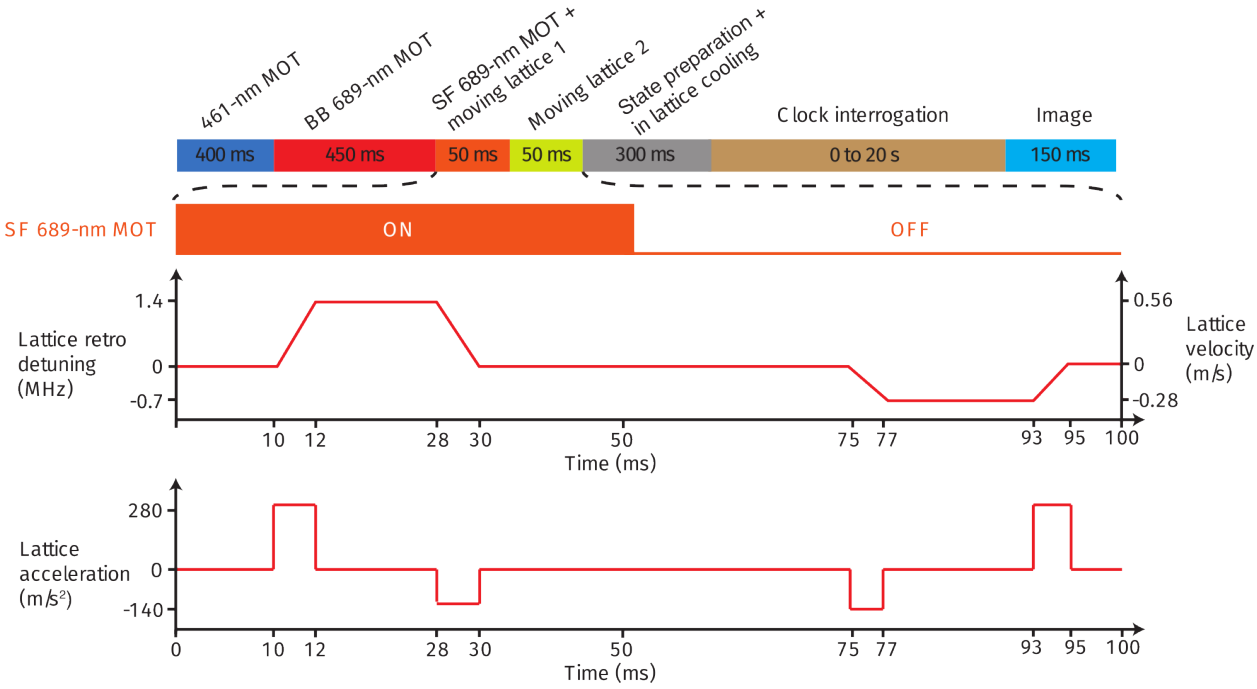


Figure 2.15: A timing diagram of our standard experimental sequence. In order to load multiple atomic ensembles, we detune the retro-reflected arm of the lattice relative to the incoming, the sequence shown here is for loading 2 ensembles with a 1 cm vertical separation. Overall dead-time in our state preparation and imaging totals 1.6s.

Using our 461 nm and 679 & 707 nm systems detailed in Sections 2.4.1 and 2.4.2, we shine our 2D MOT, Zeeman slower beams, 3D MOT beams, and repump beams for 400 ms, while ramping our magnetic field gradient from 0 to 30 G/cm over 100 ms. At the end of the blue MOT loading, we are left with around 1.5×10^6 ^{87}Sr atoms. We then turn on our 689 nm 3D MOT and stirring lasers, and turn off the blue and repump lasers after 5 ms of overlap with our red MOT beams, during which we ramp the magnetic field gradient from 30 G/cm to 3 G/cm. During this step, we frequency modulate both of our 689 nm lasers across 4 MHz in order to match the velocity profile of atoms trapped in the blue MOT to ensure a reasonable transfer efficient from blue to red, which we estimate to be around 25%. We then hold in this "broadband" red MOT for 50 ms, then start linearly ramping down our frequency modulation to 0, our beam power from the maximum power (5 mW per arm in the 3D MOT beam, 2 mW per arm in the stirring beam) to 30 uW per arm, and the magnetic field from 3 G/cm to 10 G/cm over 200 ms. At the end of this ramp, we are now in the "single-frequency" red MOT, with approximately 2.5×10^5 atoms at a temperature of 1-2 μK. During this entire initial trapping and cooling stage, our optical lattice light is on and at full power, and now atoms in the single frequency red MOT are sufficiently cold enough to be trapped in our optical lattice, with an operating maximum depth of about 130 E_{rec}.

This is now the stage where we can accelerate our lattice, with varying pulse timings to load a desired number of atomic ensembles, generally consisting of 5000-10000 atoms each at this stage. In order to balance the counts between the ensembles, we vary the time we keep the at zero velocity after an acceleration pulse. Once these ensembles are loaded across the lattice, we then shine our spin polarization light, with path shown in Fig. 2.13, that addresses the $^1S_0 \rightarrow {}^3P_1$, F=9/2 transition with $\pm\sigma$ polarized light, controlled with an liquid crystal retarder (Meadowlark LRC-200-IR2-TSC). This beam is approximately 1 mW of light across a highly elliptical beam shape, approximately 2 cm vertical x 5 mm horizontal beam diameter, allowing us to address all ensembles across the 1 cm spatial extent of the multiplexed system. We shine this spin polarization beam for 30 ms, and have a survival rate of 80% of atoms as some are lost from the trap due to heating. After spin polarization, we then cool our atoms using resolved sideband cooling along the axis of the lattice and Doppler cooling along the radial direction of the lattice. The axial and radial measured temperatures after this cooling stage are shown in Fig. 2.16. These beams address $^1S_0 \rightarrow {}^3P_1$, F=11/2 transitions, and are detuned to address the red motional sideband (≈-70 kHz from resonance) axially and approximately -Γ_{689} = $2\pi\times$7.6 kHz to the Doppler velocity profile radially. These values are calibrated and tuned daily at the kHz level to ensure high fidelity cooling.

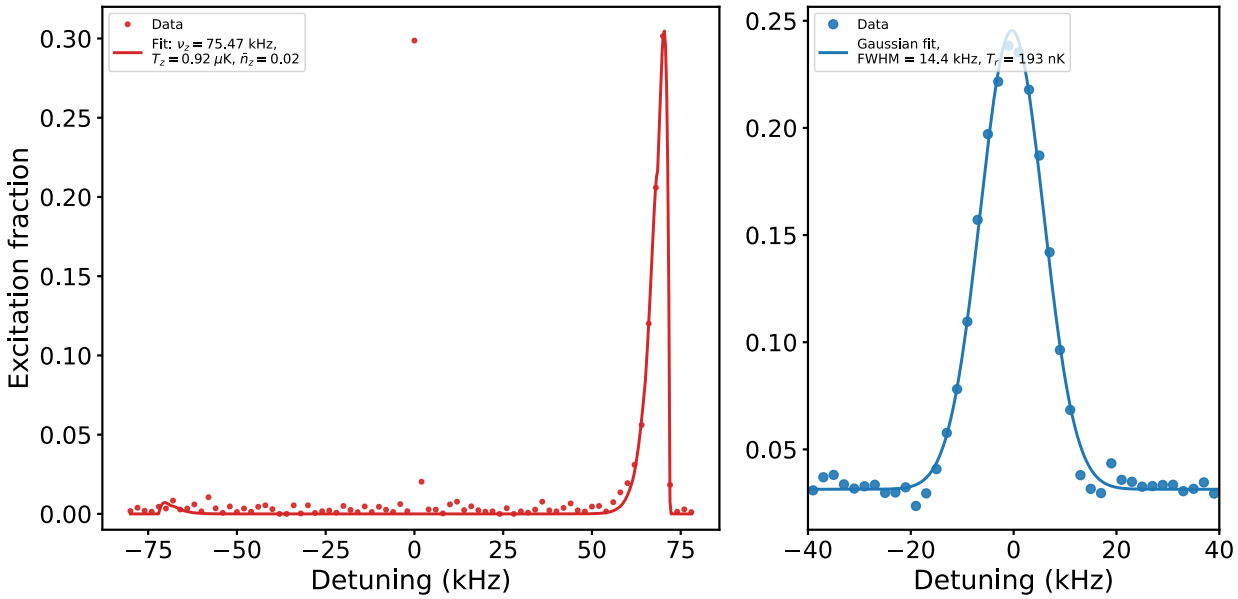


Figure 2.16: (Left) Axial clock sideband thermometry taken at 130 E_{rec}lattice trap depth following in-lattice cooling. The reduced height of the red sideband ($n_z \rightarrow n_z - 1$) indicates that 98% of atoms are populated in the lattice ground band ($n_z = 0$). Radial Doppler broadened profile taken at 15 E_{rec}. A Gaussian fit (solid blue line) yields a radial temperature of 193 nK.

After spin polarization and in-lattice cooling, we now have a cold (≈ 100 nK) atomic

sample of approximately 2000-3000 atoms in the $|^1S_0, m_F = \pm 9/2\rangle$ "spin-stretched" state. Next, in order to reduce the decohering effects of magnetic field gradients across each ensemble, we choose a hyperfine transition with the least magnetic field sensitivity. This is the $|g, m_F = \pm 5/2\rangle$ to $|e, m_F = \pm 3/2\rangle$, with a magnetic field sensitivity of 22.4 Hz/G, about 22× less sensitive than the $|e, m_F = \pm 9/2\rangle \rightarrow |g, m_{F'} = \pm 9/2\rangle$ transition [46]. In order to interrogate this specific $m_F \rightarrow m_{F'}$ transition, we increase our bias field to approximately 5.5 G to frequency resolve each $m_F \rightarrow m_{F'}$ transition as much as technically possible to avoid off-resonant drive while maintaining a π-pulse time of <5 ms for any $m_F \rightarrow m_{F'}$ clock transition. We can then apply 2 sequential π-pulses with $\pm\sigma$ light to drive from the stretched $|g, m_F = \pm 9/2\rangle$ to $|e, m_F = \pm 7/2\rangle$ (≈4.5 ms π pulse time), then $|e, m_F = \pm 7/2\rangle$ to $|g, m_F = \pm 5/2\rangle$(≈3.5 ms π pulse time). This pulse scheme is shown in Fig. 2.17. From there we apply a $\pi/2$-pulse on the $|g, m_F = \pm 5/2\rangle$ to $|e, m_F = \pm 3/2\rangle$ (≈3.0 ms π pulse time) as the first pulse in our Ramsey interrogation. After a given free evolution time, T_R, we apply a second $\pi/2$-pulse to map the phase accrued by the atom ensemble onto an excitation fraction.

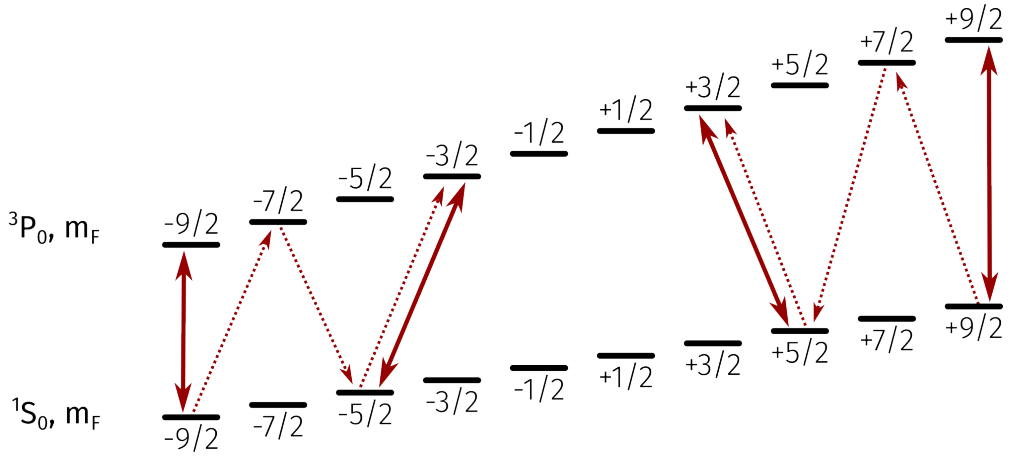


Figure 2.17: Hyperfine clock levels of ^{87}Sr. Due to the I=9/2 nuclear spin of ^{87}Sr , there are 10 m_F sublevels in $^1S_0$ and $^3P_0$. The solid arrows show interrogations of both the $|g, m_F = \pm 9/2\rangle \rightarrow |e, m_{F'} = \pm 9/2\rangle$ and $|g, m_F = \pm 5/2\rangle \rightarrow |e, m_{F'} = \pm 3/2\rangle$ transitions. The dashed arrows show the coherent transfer pulses to load into the $|g, m_F = \pm 5/2\rangle$ state from the spin stretched $|g, m_F = \pm 9/2\rangle$ state.

2.7 Measuring differential frequencies

As discussed in Section 2.6, we can prepare and readout the excitation fractions of multiple atomic clocks simultaneously. At the end of this synchronous Ramsey spectroscopy measurement, we obtain an excitation fraction for each ensemble. The excitation fractions are given

by

$$P_i = \frac{1}{2}\Big[1 + C_i \cos(\theta_L)\Big],$$
$$P_j = \frac{1}{2}\Big[1 + C_j \cos(\theta_L + \phi_d)\Big], \tag{2.10}$$

where $C_{i(j)}$ is the contrast of ensemble $i(j)$, θ_L is the common-mode laser phase, and ϕ_d is the differential phase which yields the differential frequency ($\delta f_{ij} = f_j - f_i$) between ensemble pair (i, j) through $\phi_d = 2\pi\delta f_{ij} T_R$ for a given known Ramsey free evolution time T_R.

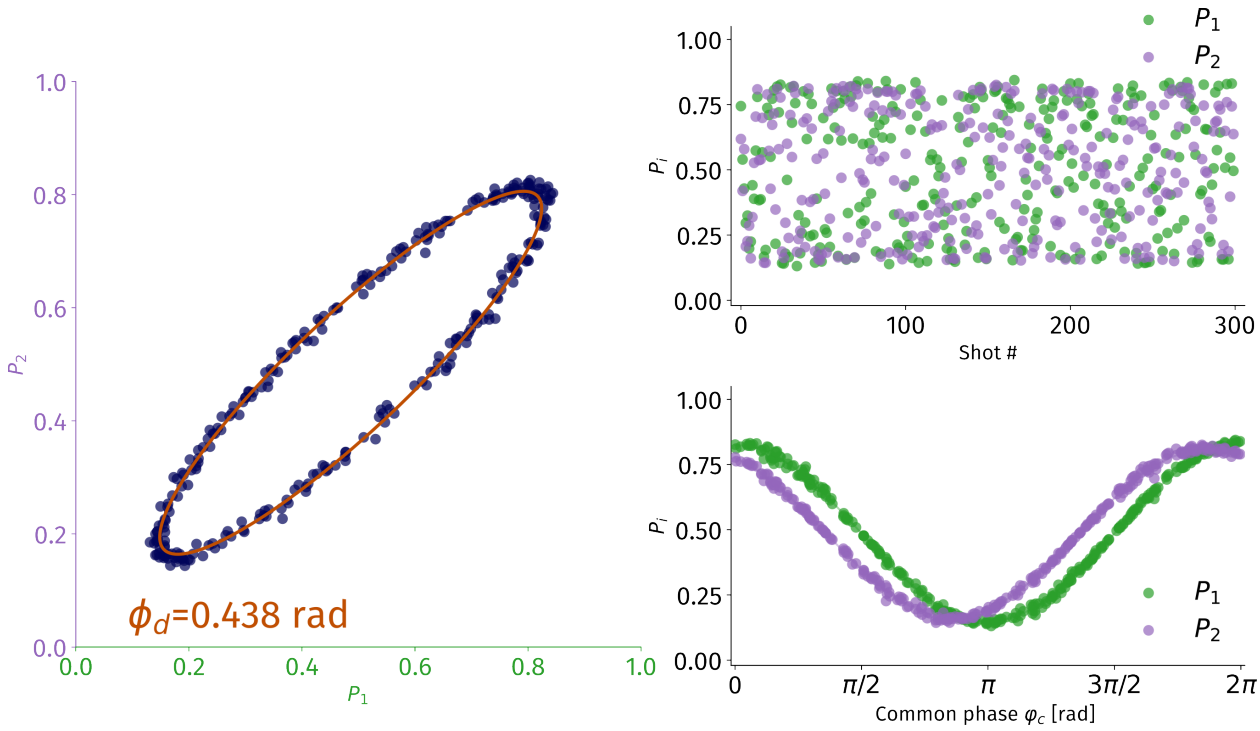


Figure 2.18: (Left) Measured excitation fraction from ensemble 1 and ensemble 2 after an 8.205s synchronous Ramsey experiment plotted parametrically against each other. A least squares fitting algorithm is used to fit and extract a differential phase between the ensembles. (Upper right) The data points plotted vs shot number during an experimental run. The excitation fraction for an individual ensemble is random shot-to-shot as the Ramsey interrogation time is much longer than the atom-laser coherence time. (Lower right) Data points assigned to Ramsey fringes based on the extracted differential phase between ensembles.

Since we are operating at Ramsey dark times well beyond the laser coherence times, θ_L is random and uniformly distributed from 0 to 2π. The data randomly samples from points lying on an ellipse (with slight deviations from the ellipse due to QPN). We then fit to this

ellipse using a least-squares approach [73]. To extract the differential phase [74], we rewrite the data $\{P_i, P_j\}$ (denoted as $\{x, y\}$ below) in the form of a generalized conic section

$$a_1x^2 + a_2xy + a_3y^2 + a_4x + a_5y + a_6 = 0, \tag{2.11}$$

which describes an ellipse when $a_2^2 - 4a_1a_3 < 0$. We rewrite Eq. 2.10 as

$$\begin{aligned} x' &= \frac{2x-1}{C_x} = \cos(\theta_L), \\ y' &= \frac{2y-1}{C_y} = \cos(\theta_L + \phi_d). \end{aligned} \tag{2.12}$$

Through canceling out θ_L, we have

$$\begin{aligned} &\frac{4}{C_x^2}x^2 - \frac{8\cos\phi_d}{C_xC_y} + \frac{4}{C_y^2}y^2 + \left(\frac{4}{C_xC_y} - \frac{4}{C_x^2}\right)x + \left(\frac{4}{C_xC_y} - \frac{4}{C_y^2}\right)y \\ &+ \left(\frac{1}{C_x^2} - \frac{2}{C_xC_y} + \frac{1}{C_y^2} - \sin^2\phi_d\right) = 0, \end{aligned} \tag{2.13}$$

which can be matched up with the coefficients a_i from Eq. 2.11. The differential phase ϕ_d is then extracted using:

$$\phi_d = \cos^{-1}\left(\frac{-a_2}{2\sqrt{a_1a_3}}\right). \tag{2.14}$$

The associated Allan deviation is extracted via jackknifing technique [56], and is then fitted to a white frequency noise model with $1/\sqrt{\tau}$ scaling. Extrapolating the fit to the full averaging time yields the statistical uncertainty of the differential frequency.

Fig. 2.20 shows our first realization of this differential frequency measurement in our system. Here we use an 8.205 s Ramsey time, T_R, and collect 1193 single-shot data points over 3.3 hours of averaging. The differential frequency uncertainty is limited by the intrinsic quantum projection noise of our ensembles of ≈2400 atoms each, and this limit is given by

$$\sigma^2(x) = \frac{1}{N_1}P_1(1-P_1), \tag{2.15a}$$

$$\sigma^2(y) = \frac{1}{N_2}P_2(1-P_2). \tag{2.15b}$$

where N_i is the number of atoms and excitation fraction in the i^{th} ensemble. Now we can express the variance due to QPN in each ensemble in terms of ϕ_d as

$$\sigma^2(\phi_d) = \left(\frac{\partial\phi_d}{\partial x}\right)^2\sigma^2(x) + \left(\frac{\partial\phi_d}{\partial y}\right)^2\sigma^2(y), \tag{2.16}$$

Evaluating the partial derivatives gives us the QPN variance in terms of ϕ and C, where we assume C_j=C_i=C.

$$\sigma^2(\phi_d) = \frac{4}{C^2}\left[\csc^2(\theta_L)\,\sigma^2(x) + \csc^2(\theta_L+\phi_d)\,\sigma^2(y)\right], \tag{2.17}$$

Since θ_L is randomly distributed over $[0, 2\pi)$ for each shot, we average over all θ_L to arrive at

$$\langle \sigma^2(\phi_d) \rangle = \frac{4}{C^2} \left[\int_0^{2\pi} \frac{d\theta_L}{2\pi} \left(\csc^2(\theta_L)\, \sigma^2(x) + \csc^2(\theta_L + \phi_d)\, \sigma^2(y) \right)^{-1} \right]^{-1}, \tag{2.18}$$

This simplifies down to the familiar QPN-limited Ramsey variance of $\langle \sigma^2(\phi_d) \rangle = 2/(NC^2)$ when C=1. For C<1, the QPN limit now depends on the value of phase and contrast, which causes the oscillations in the QPN limit seen in Fig. 2.19.

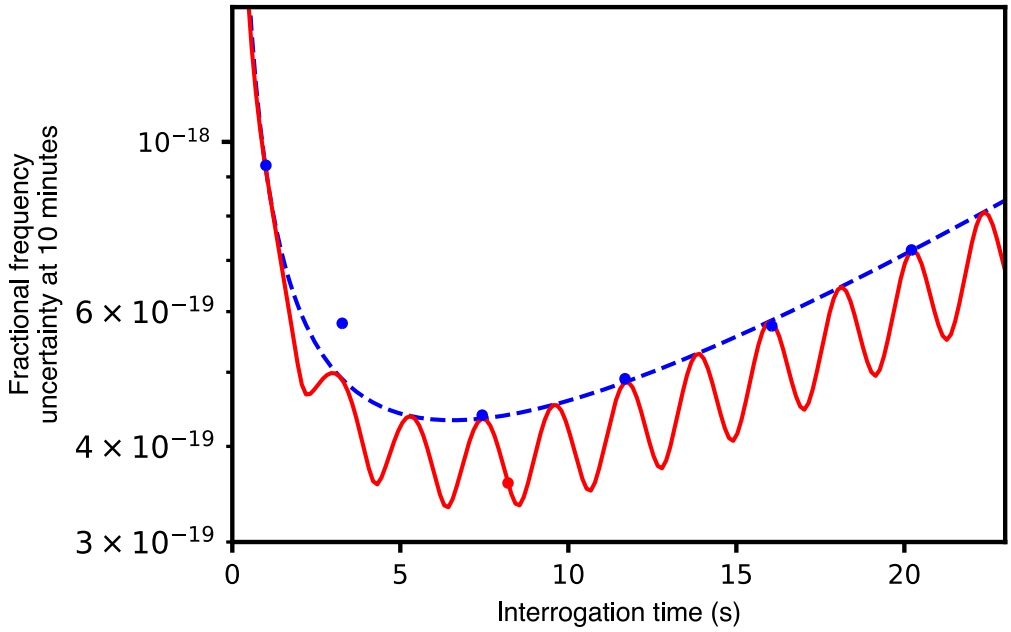


Figure 2.19: Measured differential fractional frequency uncertainties at varying synchronous Ramsey interrogation times, T_R, averaged over 10 minutes. Each blue point's T_R is chosen to give a differential phase, ϕ_d of an odd multiple of $\pi/2$, and the blue dashed line is the theoretical QPN limit calculated for a fixed phase offset of $\pi/2$ and N_i=2400. However, as shown in Eq. (2.18), the QPN limit for a non-unity contrast, C, actually depends on ϕ_d, and is in fact maximized at odd multiples of $\pi/2$, as shown by the red solid line. Finally, the red point corresponds to our operational Ramsey time and QPN limit for the figures in this chapter, which we choose to minimize our QPN while keeping our ϕ_d far enough away from even multiples of $\pi/2$, where our fitting becomes biased, see Section 3.3.8 and Fig. 3.6.

2.8 Simultaneous loading of different isotopes of Sr

The majority of this chapter so far has been focused on the use of the fermionic isotope of Sr, ^{87}Sr, but three other bosonic isotopes of Sr exist, ^{88}Sr, ^{86}Sr, and ^{84}Sr. The relative

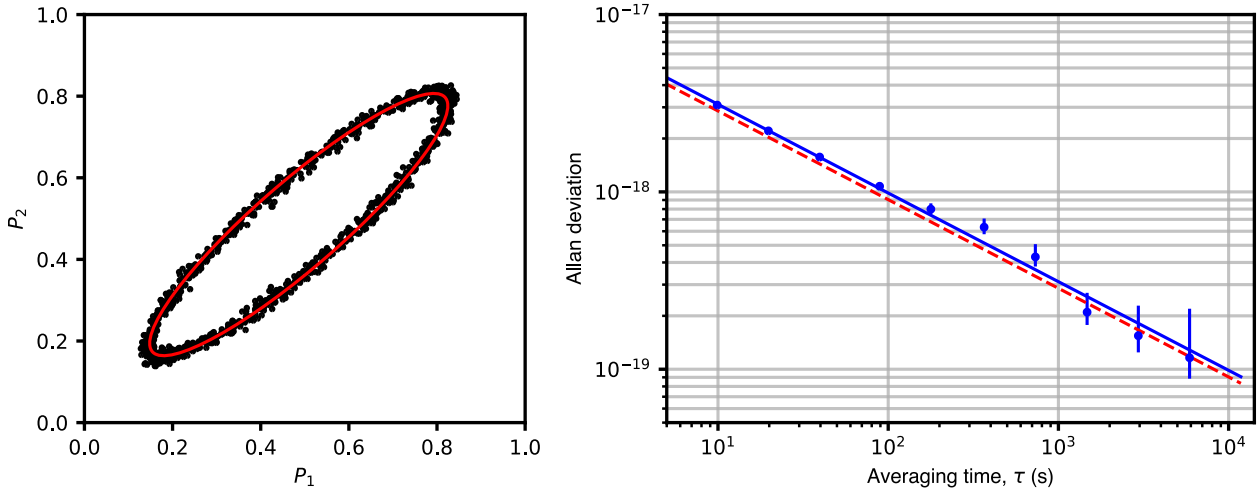


Figure 2.20: (Left) Parametric plot of two ensemble excitation fractions, $P_{i,j}$, collected over 1193 shots of synchronous Ramsey interrogation experiments with an 8.205 s Ramsey time, totaling 11,800s of averaging. The extracted phase from this ellipse, found through a least squares fitting, was 0.438 rads. (Right) Extracted Allan deviation of our differential frequency comparison as a function of averaging time. Each blue point is a differential fractional frequency uncertainty for a give averaging time, extracted with a jack-knife resampling method to estimate single-shot phase variance[56]. The fitted differential instability averages down as $9.7(4) \times 10^{-18}/\sqrt{\tau}$ reaching an differential fractional frequency uncertainty of 8.9×10^{-20} after 3.3 hours of averaging. This differential instability is consistent with the calculated QPN limit, shown by the red dashed line, for the independently measured ≈2400 atoms per ensemble.

natural abundances of each isotope are 82.6% ^{88}Sr, 6.9% ^{87}Sr, 9.9% ^{86}Sr, and 0.6% ^{84}Sr. The Sr sample in our oven has not been isotopically purified, so the only way we determine the isotope that is trapped in our MOTs is through controlling laser frequency. The frequency shift for each isotope is shown in the upper left of Fig. 2.21. When starting a MOT from scratch, it's often easier to create one based on ^{88}Sr, as a much higher natural abundance allows for easier detection of MOT florescence by eye or camera. Furthermore, there is no hyperfine level structure at zero B-field to complicate the trapping scheme, unlike ^{87}Sr, where a stirring beam addressing low $|m_F|$ levels is required to trap atoms in the 689 nm red MOT effectively.

Optical clocks based on ^{88}Sr have also been implemented [57, 75, 76], which have the advantage of trapping and cooling more atoms with a simpler MOT setup than in ^{87}Sr clocks. However the $^1S_0 \rightarrow {}^3P_0$ clock transition is completely forbidden at zero magnetic field in the bosonic isotopes due to an absence of nuclear spin induced hyperfine mixing in the ^3P_J manifold. Through the application of a large (≥20G) magnetic field, this ^3P_J mixing can still be imposed, allowing for interrogation of the clock transition with a variable linewidth

based on the B-field strength [77].

There have been proposals [78–83] for tests of the Standard Model through precision isotope tests, motivating the ability to simultaneously interrogate different isotopes of Sr. As a step towards these experiments, we demonstrated the ability to load multiple spatially separated ensembles consisting of different isotopes of Sr. The scheme for accomplishing this along with EMCCD images of ^{87}Sr paired with each bosonic isotope is shown in Fig. 2.21. The general method is to load a single ensemble of ^{87}Sr , move the ^{87}Sr ensemble upwards 1 cm, shelve the ^{87}Sr atoms into the $^3P_0$ state, create a new 461 nm and 689 nm MOT tuned for the specific bosonic isotope desired, move the ensembles to be equally displaced from the lattice beam waist, then finally image the two ensembles. We haven't yet demonstrated differential isotope comparisons in this system, owing to the current technical inability of our system to apply high enough B-fields to allow the clock transition in the bosonic isotopes. Additionally, each isotope will have its own magic wavelength, requiring different trapping techniques or AC stark shift evaluation methods compared to the ones presented in this thesis [80].

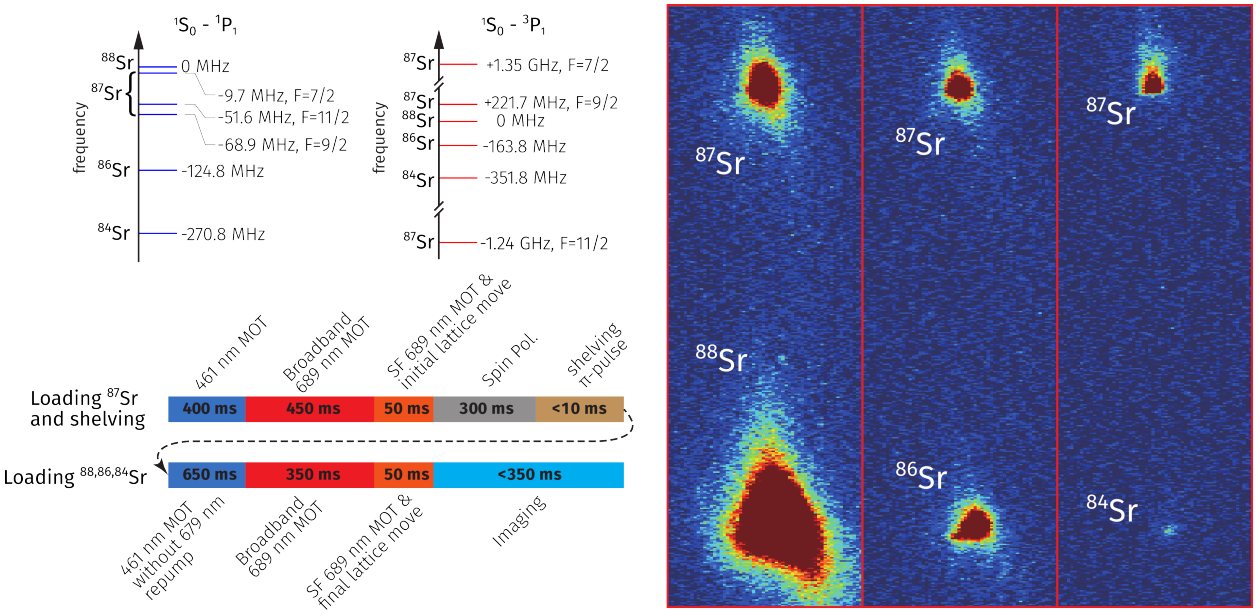


Figure 2.21: Demonstration of simultaneous loading of ^{87}Sr and all other stable bosonic isotopes, ^{88}Sr, ^{86}Sr, and ^{84}Sr. (Upper left) Isotope shifts relative to ^{88}Sr for both the 461 nm and 689 nm transitions. (Lower left) Experimental sequence for loading ^{87}Sr and a bosonic isotope. The sequence starts with a standard load and transport sequence for an ensembles of ^{87}Sr atoms, which is then shelved in $^3P_0$ such that the ensemble will be unperturbed by the MOT stages for the bosonic isotope. The frequency-adjusted 461 nm MOT is then started without the 679 nm repump beam, as this would pump all shelved ^{87}Sr back out of the $^3P_0$. From there, we continue with the shifted 689 nm MOT, then a second transport sequence to bring both ensembles to be symmetric around the lattice beam waist. (Right) EMCCD images of ^{87}Sr loaded with each bosonic isotope, with the captured fluorescence signal reflecting the relative abundances of the isotopes (82.6% ^{88}Sr, 6.9% ^{87}Sr, 9.9% ^{86}Sr, and 0.6% ^{84}Sr).

Chapter 3

Gravitational redshift test at the centimeter scale

This chapter was previously published as Xin Zheng, Jonathan Dolde, Matthew C. Cambria, Hong Ming Lim, and Shimon Kolkowitz. "A lab-based test of the gravitational redshift with a miniature clock network". In: Nature Communications *14.1 (Aug. 2023), p. 4886.* ISSN: *2041-1723.* DOI: *10.1038/s41467-023-40629-8.*

3.1 Introduction to our gravitational redshift measurement

In this chapter, we perform a local-oscillator independent, blinded test of the gravitational redshift at the sub-centimeter scale using our spatially multiplexed optical lattice clock [59] consisting of an array of ^{87}Sr atom ensembles trapped in a vertical, one-dimensional (1D) optical lattice (Fig. 3.1). We prepare 5 atomic ensembles equally spaced by 2.5 mm, spanning a total height difference of 1 cm. Synchronous differential comparisons are performed between the 5 ensembles, resulting in 10 unique pairwise clock comparisons recorded simultaneously, including 4 pairs at 2.5 mm, 3 pairs at 5.0 mm, 2 pairs at 7.5 mm, and 1 pair at 1.00 cm height difference. The gravitational redshift is tested by mapping out the frequency differences between each ensemble pair as a function of height difference. Ultimately, we measure a fractional frequency gradient of $[-12.4 \pm 0.7_{\text{stat}} \pm 2.5_{\text{sys}}] \times 10^{-19}$/cm, consistent with the expected gravitational redshift gradient of -10.9×10^{-19}/cm. Our result constrains deviations from the redshift predicted by general relativity to 0.13 ± 0.23 for mm to cm scale height differences.

Einstein's theory of general relativity [85] has thus far been consistent with every experimental test performed [86], including classical [87, 88], modern [89, 90] and strong field cosmological tests [91–93]. However, despite the successful integration of special relativity and quantum mechanics as quantum field theory, there is currently no theory that successfully unifies general relativity with quantum mechanics. This motivates continued experimental

tests at new length scales, and suggests that performing precision tests of general relativity with quantum systems may offer a way to explore their interplay [94–96].

The gravitational redshift is a central prediction of general relativity. Thanks to rapid advancements in their stability and accuracy [55, 66, 69, 97–100], atomic clocks have now enabled tests of the gravitational redshift over a wide range of length scales [10–12, 101–103]. Recent tests of the gravitational redshift include a frequency comparison between two single-ion clocks with one of the clocks elevated by 30 cm [101], comparisons between terrestrial clocks and microwave atomic clocks in eccentric orbits which have produced the strongest limits on deviations from the expected redshift [11, 102], a frequency comparison between two synchronously linked portable ^{87}Sr optical lattice clocks with a 450 m height difference at the Tokyo Skytree tower [12] resulting in the most precise terrestrial constraint on deviations from the gravitational redshift at the 10^{-5} level, and a recent in-situ synchronous frequency gradient measurement across a millimeter-scale atomic ensemble with an unprecedented differential precision of 7.6×10^{-21} [103].

For two otherwise identical clocks experiencing the same gravitational field with a height difference Δh, their frequency difference δf due to the gravitational redshift is given by

$$\frac{\delta f}{f} \approx \frac{g \Delta h}{c^2} \tag{3.1}$$

where f is the clock frequency, c is the speed of light, and g is the gravitational acceleration. Near the surface of Earth, this amounts to a fractional frequency shift of 1.1×10^{-18} per centimeter of vertical displacement. With optical clocks now reaching instabilities and inaccuracies at the level of 10^{-18} and below [66, 98, 99, 104, 105], they are becoming a sensitive probe of the point to point geopotential at the sub-centimeter scale, where they are expected to complement other methods of geodesy [29–32, 98, 106–109]. For example, a blinded comparison between two independent Yb optical lattice clocks was recently performed with accuracy, instability and reproducibility all at the level required to resolve sub-cm height differences [98]. In addition, the frequency gradient due to the gravitational redshift across a single millimeter-scale atom ensemble was recently observed using Rabi spectroscopy of ^{87}Sr without the use of a blinding offset and taking advantage of an 8-mHz linewidth clock laser [103].

Emerging clock applications such as relativistic geodesy require transportable optical clocks, which currently have poorer stabilities and accuracies than those of laboratory-based clocks [30, 32, 110]. State-of-the-art laboratory-based optical clocks often make use of bulky and immobile reference cavities with second-scale coherence times [47, 49, 50] in order to achieve lower levels of clock instability and to aid in rapid systematic evaluation, limiting deployment in the field. It has recently been demonstrated that differential measurements between single ions [54] and neutral atom ensembles [59, 111, 112], as well as differential spectroscopy by phase-coherently linking a zero-dead-time optical lattice clock and a single ion clock [113], allow interrogation times beyond the limit set by the local oscillators, opening up the prospects for future applications with transportable or space-based clocks [23–27].

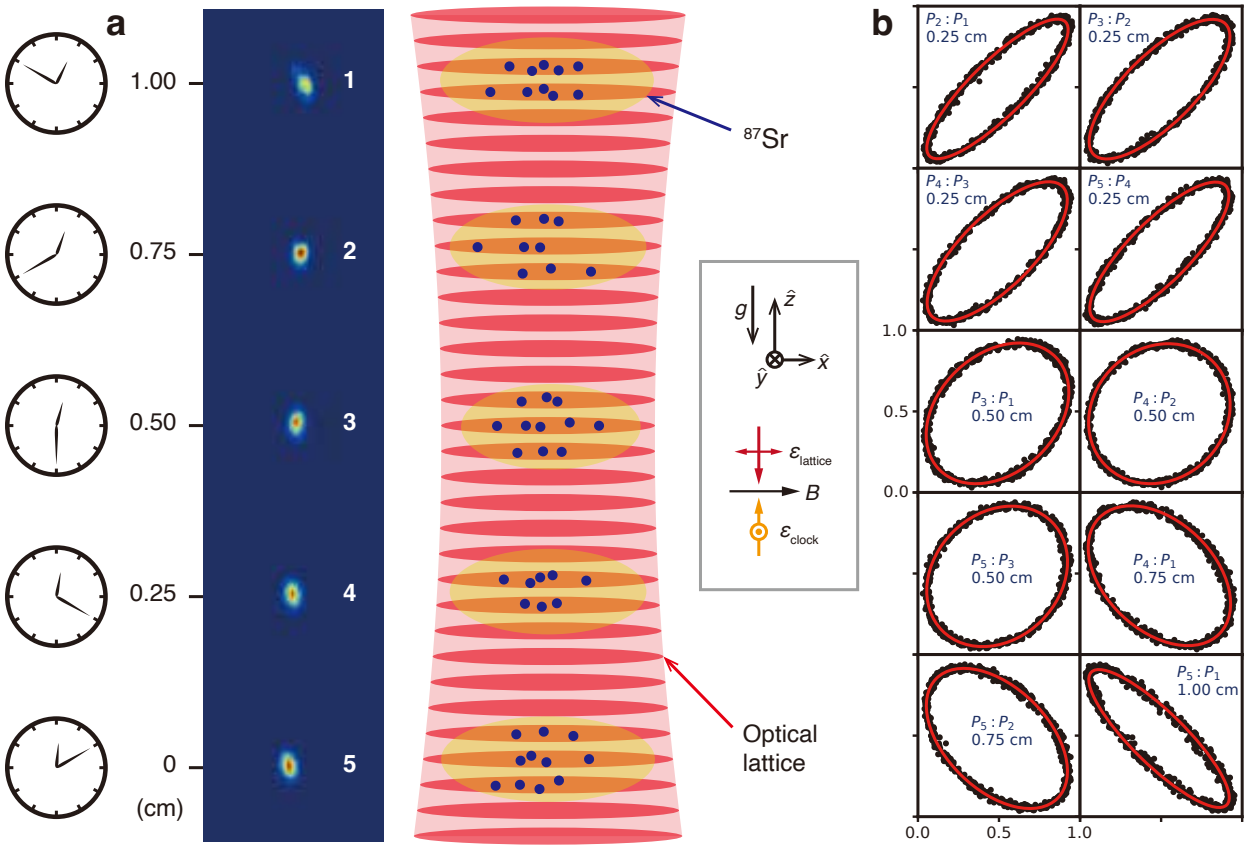


Figure 3.1: **a)** A representative camera image of a spatially multiplexed array with 5 ensembles of ^{87}Sr atoms (indexed 1–5 from top to bottom) trapped in a vertical 1D optical lattice for differential clock comparisons. The spacing between neighboring ensembles is 0.25 cm, spanning a total height difference of 1 cm. Due to the gravitational redshift, clocks at a higher gravitational potential are predicted to tick faster than clocks at a lower potential. The grey box shows the orientations of the applied bias magnetic field (B), and the lattice and clock laser polarizations (ϵ). **b)**. A representative outcome from synchronous Ramsey spectroscopy on the $|^1S_0, m_F = +5/2\rangle \leftrightarrow |^3P_0, m_F = +3/2\rangle$ clock transition with a 10 s free precession time using 5 atomic ensembles, resulting in 10 pairwise clock comparisons. In each plot, the excitation fractions of ensemble j are plotted against the excitation fractions of ensemble i ($P_j : P_i$, where $j > i$), tracing out an ellipse which is fitted to in order to extract the frequency difference between that pair. The frequency difference is dominated by the first-order differential Zeeman shift, which is rejected when averaging transitions between opposite spin states. See Section 3.3.2 for details.

3.2 Atom preparation and experimental procedure

5 ensembles of ultra-cold, spin-mixed ^{87}Sr atoms are loaded into a vertical optical lattice with a depth of 130 $E_{\rm rec}$, where $E_{\rm rec}/h \approx 3.5$ kHz is the recoil energy of a lattice photon and h is the Planck constant, with an equal spacing between ensembles of 0.25 cm over a total extent of 1 cm vertically. This is followed by hyperfine spin polarization into either stretched state ($|^1S_0, m_F = \pm 9/2\rangle$) and in-lattice cooling. The lattice is then adiabatically ramped down to the operational trap depth ($u_{op} = 15\ E_{\rm rec}$), at which a series of π pulses addressing the $^1S_0 \leftrightarrow {}^3P_0$ ($g \leftrightarrow e$) transitions prepare the atoms into $|e, m_F = \pm 3/2\rangle$. Ramsey spectroscopy is performed by interrogating the $|g, m_F = \pm 5/2\rangle \leftrightarrow |e, m_F = \pm 3/2\rangle$ clock transitions. Following the second Ramsey $\pi/2$ pulse, the lattice is adiabatically ramped back up to 130 $E_{\rm rec}$ for read-out. The populations in the ground and excited clock states of all 5 ensembles are read-out in parallel with imaging pulses along the lattice axis, with scattered photons collected on a camera (Andor, iXon-888). The excitation fraction is extracted through $P = (N_e - N_{bg})/(N_g + N_e - 2N_{bg})$, where N_g, N_e and N_{bg} are the ground state population, excited clock state population, and background counts without atoms, respectively.

We perform 4 lattice movements of 0.25 cm each in order to load 5 spatially separated atom ensembles, and a final lattice movement of 0.5 cm in the opposite direction, which positions the ensemble array symmetrically around the lattice beam waist. The entire duration of the moving lattice portion of the loading sequence is typically less than 100 ms, with 80% of the total atom number transferred efficiently from the narrow-line MOT to the 5 ensembles. In-lattice axial (sideband) and radial (Doppler) cooling are subsequently applied to lower the atom temperatures after lattice acceleration.

For clock interrogation, we probe the $|g, m_F = \pm 5/2\rangle \leftrightarrow |e, m_F = \pm 3/2\rangle$ transitions with a shared clock laser along the lattice axis. Synchronous Ramsey spectroscopy is performed to reject common-mode local oscillator noise. The typical Ramsey interrogation time (T_R) is roughly 10 s, with a dead time (T_d) of 2 s between interrogations for sample preparation and read-out, yielding a measurement duty cycle of 83%. Simultaneously probing 5 ensembles results in 10 pairwise clock comparisons for a single nuclear spin state. Combined with atom numbers (N) of ~ 2000 per ensemble and contrast (C) of above 80 %, the typical differential instability for each pairwise comparison is below $1 \times 10^{-17}/\sqrt{\tau}$, where τ is the averaging time, consistent with the quantum projection noise (QPN) limit

$$\sigma_{\rm QPN}(\tau) = \frac{\sqrt{2}}{2\pi f C T_R}\sqrt{\frac{T_R + T_d}{N\tau}}, \tag{3.2}$$

where f is the clock frequency, τ is the averaging time, and the factor of $\sqrt{2}$ assumes equal contribution from each clock.

In our measurements, we probe with an interleaved sequence between clock transitions with either nuclear spin state, $|g, m_F = \pm 5/2\rangle \leftrightarrow |e, m_F = \pm 3/2\rangle$. This results in 10 ellipses for transition with a single nuclear spin state, and thus 20 ellipses per measurement. A representative plot of the $|g, m_F = +5/2\rangle \leftrightarrow |e, m_F = +3/2\rangle$ transition is shown in Fig. 3.1b.

The differential phase for each ellipse is dominated by the differential first-order Zeeman shift (See Section 3.3.2), which is on the order of $\pm 8 \times 10^{-17}$/cm and is rejected by averaging transitions with opposite spin states.

3.3 Systematic evaluation in detail

3.3.1 Systematic evaluation summary

The results of the full systematic evaluation are listed in Table 3.1. The procedure for measuring the contribution of each potential systematic is discussed in detail later on in this section. Several effects dominate the extracted differential frequency and the corresponding systematic uncertainty, and we highlight them here. First, atomic interactions due to p-wave collisions between on-site atoms lead to a frequency shift that scales linearly with atomic density [114–116]. In our differential measurement, the density shift is suppressed by a factor of roughly 10 compared to the absolute shift by balancing the number of atoms loaded into each ensemble. By intentionally varying the atom number differences, the differential density shift for a symmetric pair (2, 4) at u_{op} is evaluated to be $-0.7(1) \times 10^{-19}$ per 100 atom number difference (Fig. 3.2**a**). Due to the Gaussian nature of the lattice beam, we observe a minor trap volume dependence of the density shift, which is accounted for in our evaluation by independently extracting the density shift as a function of atom number difference for each pairwise comparison (See Section 3.3.3). In each measurement run, the corresponding differential density shifts are corrected for each ensemble pair individually.

The largest systematic shift in our system is the second-order Zeeman shift due to the background magnetic field gradient (~ 1.5 mG/cm). The splitting of the transitions with opposite sign nuclear spin states provides a measurement of the magnetic field difference between each ensemble pair, while the overall magnitude of the applied bias magnetic field (~ 5.5 G) is measured independently using a more magnetically sensitive transition. This bounds the uncertainty from the second-order Zeeman gradient to below 1×10^{-19}/cm, limited by uncertainty in the second order Zeeman coefficients for the clock transition (Fig. 3.2**b** and Section 3.3.2).

The frequency shift due to black-body radiation (BBR) is the dominant source of systematic uncertainty for many room-temperature optical clocks[66, 97–99]. In our system, uncertainty arises due to temperature gradients in the surrounding environment. Because the ensembles are arrayed vertically, the primary contribution comes from differences in temperature between the top and bottom recessed viewports of the science chamber, which are the closest surfaces to the atoms. To evaluate the effect of this BBR gradient, we intentionally introduce a thermal gradient by varying the temperature difference between the two viewports by up to ± 1 K. Mapping out the resulting differential frequency shifts of the 10 ensemble pairs, we measure a linear BBR gradient sensitivity of $-4.2(1) \times 10^{-18}$/cm per 1 K difference (Fig. 3.2 **c** and Section 3.3.4). This results in a weighted average BBR gradient of $-15.7(1.5) \times 10^{-19}$/cm under normal operating conditions, which is determined from the

temperature differences recorded with calibrated temperature sensors that were continuously monitored during data taking. This measurement also highlights the application of differential comparisons between spatially multiplexed ensembles for BBR gradient evaluation at the 10^{-19}/cm level, which will be important for pushing the accuracy of room temperature optical lattice clocks below the 10^{-18} level.

AC Stark shifts from lattice light contribute to the fractional frequency uncertainty of state-of-the-art optical lattice clocks at the low 10^{-18} level [117, 118]. For differential comparisons between ensembles within a single shared optical lattice, this is significantly suppressed. A differential lattice AC Stark shift between two ensembles is caused by the relative trap depth difference δu arising from the lattice beam profile, and scales linearly with δu to first-order(See Section 3.3.5). In conjunction with the multiplexed ensemble technique, we can rapidly map out both δu and the differential light shifts. In doing so, we also observe a residual spatial light shift gradient of $-8.0(1.1) \times 10^{-20}/E_{\mathrm{rec}}$/cm, which depends linearly on the lattice depth and the spatial separation between ensembles, and does not depend on δu. We believe this gradient is likely due to the differential tensor Stark shift arising from slight variations in the orientation of the magnetic field vector across the ensemble array. This is supported by the observation of a differential vector Stark gradient of $-2.5(2) \times 10^{-18}/E_{\mathrm{rec}}$/cm in our system (See Section 3.3.5). Regardless of the exact origin of the spatial light shift gradient, we are able to measure and account for it by varying the lattice depth. Subtracting off this residual spatial gradient, we observe correlations between δu and the remaining shifts (Fig. 3.2**d**), as expected. This allows us to extract the operational lattice detuning from the effective magic wavelength [103, 118], and to independently evaluate the lattice light shift gradient upon removal of the δu shifts (Fig. 3.2**e**).

3.3.2 Zeeman shifts

Coupling of the clock states to external magnetic fields gives rise to Zeeman shifts of the clock transition frequency. For a single atomic ensemble with magnetic field amplitude B, the Zeeman shifts when probing the $|g, m_F = \pm 5/2\rangle \leftrightarrow |e, m_F = \pm 3/2\rangle$ clock transitions can be expressed as

$$\nu_{\mathrm{ZS}}(B, \pm) = \pm \mu_L B + \mu_Q B^2, \tag{3.3}$$

where μ_L and μ_Q are the first and second-order Zeeman shift coefficients, respectively. For differential clock comparison between ensemble pair (i, j), where $j > i$, with differing magnetic field strengths B_i and B_j, the differential Zeeman shifts, $\Delta\nu_{\mathrm{ZS}}(B_i, B_j, \pm) = \nu_{\mathrm{ZS}}(B_j, \pm) - \nu_{\mathrm{ZS}}(B_i, \pm)$, are given by

$$\begin{aligned} \Delta\nu_{\mathrm{ZS}}(B_i, B_j, \pm) &= \pm \mu_L (B_j - B_i) + \mu_Q (B_j^2 - B_i^2), \\ &= \pm \mu_L \delta B + 2\mu_Q B \delta B, \end{aligned} \tag{3.4}$$

where $B = (B_i + B_j)/2$ is the mean magnetic field amplitude, and $\delta B = B_j - B_i$ is the magnetic field difference. The first-order differential Zeeman shift (on the order of $\pm 8 \times 10^{-17}$/cm) is

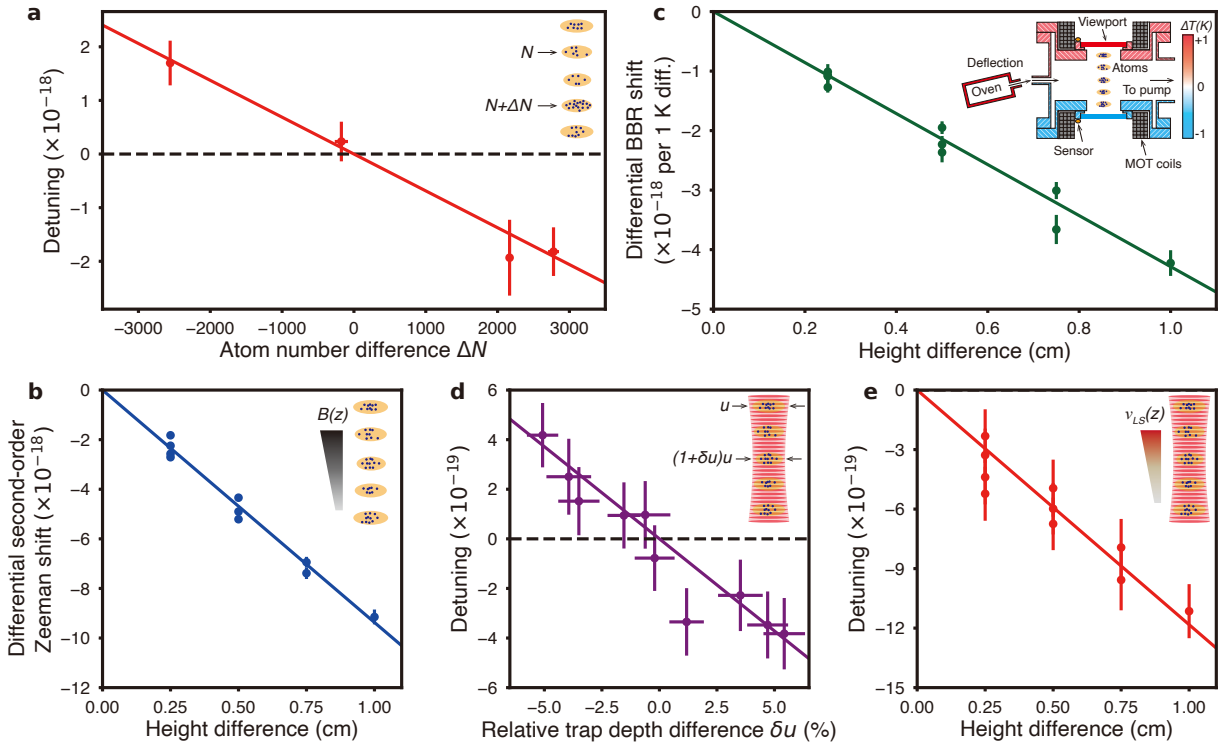


Figure 3.2: **a**, The differential density shift at $u_{op} = 15\ E_{\rm rec}$ for a symmetric pair (2, 4) is evaluated by varying the atom number difference (ΔN). A linear fit yields a shift of $-0.7(1) \times 10^{-19}$ per 100 atom number difference. **b**, Evaluation of the second-order Zeeman gradient arising from the magnetic field gradient ($\partial B/\partial z \approx 1.5$ mG/cm). A linear fit yields a gradient of $-95.3(1.0) \times 10^{-19}$/cm. **c**, Characterization of the BBR shift due to thermal gradients across the vacuum chamber. The inset is an illustration of the science chamber. To evaluate the BBR effect, a thermal gradient is introduced by varying the temperature difference between top and bottom viewports by up to ± 1 K. A linear fit yields a BBR sensitivity of $-4.2(1) \times 10^{-18}$/cm per 1 K difference in our system. **d**, Correlations between relative trap depth difference (δu) and differential lattice light shifts after subtraction of the residual spatial light shift gradient. u and $(1+\delta u)u$ correspond to the absolute trap depths for the ensemble pairs. **e**, Evaluation of lattice light shift gradient at $u_{op} = 15\ E_{\rm rec}$ after removing contributions from δu shifts. A linear fit yields a gradient of $-8.0(1.1) \times 10^{-20}/E_{\rm rec}$/cm.

Table 3.1: **Fractional frequency gradients and corresponding uncertainties.** Uncertainties are quoted as 1σ standard deviations. [a] The BBR shift and second-order Zeeman shift are corrected for each measurement; here the weighted averaged values across all 14 measurements are listed. [b] The density shift and bias error from ellipse fitting are corrected for each pairwise clock comparison individually, and do not depend linearly on spatial separation.

Sources	Gradient ($\times 10^{-19}$/cm)	Uncertainty ($\times 10^{-19}$/cm)
BBR[a]	-15.7	1.5
Lattice light	-11.8	1.2
Density[b]	–	1.0
2nd order Zeeman[a]	-95.3	1.0
Probe Stark	0	0.5
DC Stark	0	0.1
Ellipse fitting[b]	–	0.5
Total systematic correction	+122.8	2.5
Statistical gradient	-135.2	0.7
Corrected gradient	-12.4	2.6
Expected redshift gradient	-10.9	< 0.1

rejected by averaging opposite spin state transitions, while their splitting yields δB. In the limit of $|\delta B| \ll B$, the second-order differential Zeeman shift can be approximated as

$$\begin{aligned} \delta B &= \Delta\nu_{\text{split}}/(2\mu_L), \\ \Delta\nu_{\text{ZS,2}} &= \xi \Delta\nu_{\text{split}} B, \end{aligned} \tag{3.5}$$

where $\xi = \mu_Q/\mu_L$, and $\Delta\nu_{\text{split}}$ is the splitting between the transitions with opposite spin states after subtraction of residual vector AC Stark shift.

The second-order Zeeman shift correction is applied for each measurement run, with uncertainty primarily limited by ξ, which is found to be 0.0105(1) G^{-1} by varying B and δB. This is in good agreement with the theoretical value of 0.0104(2), calculated using $\mu_L = -22.4$ Hz/G and $\mu_Q = -0.233(5)$ Hz/G^2 [46]. The bias magnetic field B is calibrated each measurement day using the magnetically sensitive transitions $|^1S_0, m_F = \pm 9/2\rangle \rightarrow |^3P_1, m_F = \pm 11/2\rangle$, and has a typical value of ~ 5.5 G with fractional uncertainty below 10^{-4}. The field difference δB (~ 1.5 mG/cm) is extracted from the splitting between the clock transitions with opposite nuclear spin states with fractional uncertainty below 10^{-3} after subtraction of the vector AC Stark shift. Through weighted averaging of the data taken at normal operating conditions, we find the mean second-order Zeeman gradient to be $-95.3(1.0) \times 10^{-19}$/cm (Fig. 3.2**b**).

3.3.3 Density shift

Due to the Pauli-exclusion principle, s-wave interactions are forbidden for identical Fermionic atoms within a single lattice site, while p-wave collisions are allowed, leading to a clock frequency shift that scales linearly with atomic density [114, 115]. In our system, the differential density shift is evaluated by varying the atom numbers loaded into each ensemble for each individual pairwise comparison. For a symmetric pair (2, 4), we find a linear slope of $-0.7(1) \times 10^{-19}$ per 100 atom number difference at our operational lattice trap depth $u_{op} = 15\ E_{\mathrm{rec}}$ (Fig. 3.2**a**). In addition, we found a weak trap volume dependence due to the Gaussian nature of the lattice beam (less than 15 % across the entire array), which is accounted for in our evaluation as a different dependence on atom number difference for each pairwise comparison. For a typical run of the experiment, each atomic ensemble has about 2000 atoms, corresponding to an overall density shift of about $-14(2) \times 10^{-19}$. The differential density shift is suppressed by a factor of 10 when the atom number difference is bounded below 200 through optimization of ensemble loading times and conditions. In addition, we measure the atom number in each ensemble in every shot of the experiment, and the average differential density shift is calculated and corrected individually for each pairwise clock comparison measurement run. Uncertainty of density shift correction arises from shot-to-shot atom number fluctuations, for which we estimate an upper bound limit of 1×10^{-19}.

A recent study found that operation in a gravity-tilted shallow lattice allows for cancellation of density shifts at a "magic" lattice depth near 12 E_{rec}, where the partially delocalized Wannier-Stark states enable tunability of on-site p-wave versus neighbouring-site s-wave atomic interactions [116]. In this work we did not observe such a cancellation effect at shallower lattice depths, likely due to the difference in dynamics between Rabi spectroscopy as was employed in Ref. [116] versus our use of Ramsey spectroscopy with a 50:50 superposition [64]. This offers the prospect of further reducing uncertainty from differential density shifts in future works.

3.3.4 Black-body radiation shift

In our experiment, the optical lattice is orientated nearly vertically, with a tilt of about 5°, and is centered with respect to the science chamber to the best of abilities. The tilt is determined by measuring the Wannier-Stark ladder resonances (see Section 3.3.9 for details). The recessed high-emissivity Fused Silica viewports (MPF Products) mounted on the top and bottom sides of the science chamber are the closest surfaces to the atoms, and are primarily responsible for the black-body radiation (BBR) gradient along the lattice axis. To study the BBR effect [119, 120], we heat up either the top or bottom stainless steel flange of the science chamber, which results in a temperature difference of up to ±1 K between the top and bottom viewports (see inset of Fig. 3.2**c**). By measuring the frequency differences of the 10 ensemble pairs simultaneously, we find that the resulting frequency shifts scale linearly with the temperature difference, and the corresponding slopes scale roughly linearly with the

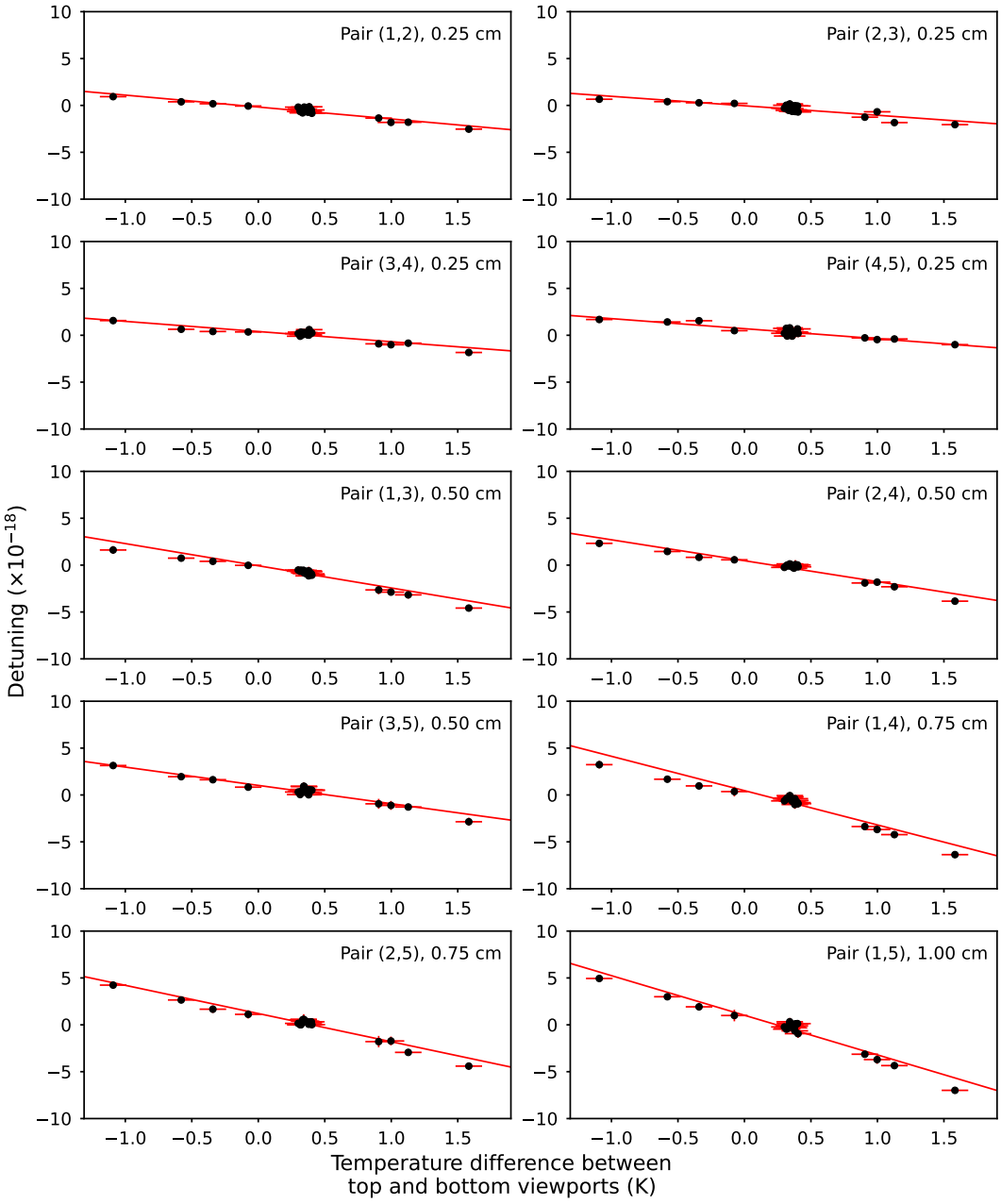


Figure 3.3: **Black body radiation shift evaluation.** Evaluations of BBR shift for all 10 ensemble pairs simultaneously. Solid lines are linear fits to the scatter points. The y-axis scales are kept the same for all the plots. The dense data points around 0.35 K correspond to temperature differences recorded under normal operating conditions. The inset text list the ensemble pair indices and corresponding height difference.

height differences (Fig. 3.3).

The BBR shift due to thermal gradients between the top and bottom viewports can be expressed as [121]:

$$\nu_{\mathrm{BBR}} = -2\frac{\alpha_{\mathrm{Sr}}\sigma_{\mathrm{SB}}}{h\epsilon_0 c}\sum_{k=\mathrm{top,bot}}\frac{\Omega_k(z)}{4\pi}T_k^4 \tag{3.6}$$

where h is the Planck constant, α_{Sr} is the atom's DC polarizability, σ_{SB} is the Stefan-Boltzmann constant, $\Omega_k(z)$ corresponds to the solid angle as seen by the atom ensemble at z. and T_k denotes the temperature on the surface of the viewport. The differential BBR shift between an ensemble pair at (z_i, z_j) is therefore given by

$$\nu_{\mathrm{BBR}} = -2\frac{\alpha_{\mathrm{Sr}}\sigma_{\mathrm{SB}}}{h\epsilon_0 c}\sum_{k=\mathrm{top,bot}}\left(\frac{\Omega_k(z_j)}{4\pi}-\frac{\Omega_k(z_i)}{4\pi}\right)T_k^4 \tag{3.7}$$

Because the viewports separation ($2Z_0 = 15$ cm) is much larger than the separation between the ensemble pairs ($\delta z_{ji} = z_j - z_i \leq 1$ cm), we approximate the solid angle difference as

$$\Delta\Omega_{ji,\mathrm{top}} = \pi r^2\left[\frac{1}{(Z_0+z_j)^2}-\frac{1}{(Z_0+z_i)^2}\right]\approx -\frac{\pi r^2}{Z_0^3}\,\delta z_{ji}, \tag{3.8}$$

$$\Delta\Omega_{ji,\mathrm{bot}} = \pi r^2\left[\frac{1}{(Z_0-z_j)^2}-\frac{1}{(Z_0-z_i)^2}\right]\approx +\frac{\pi r^2}{Z_0^3}\,\delta z_{ji} \tag{3.9}$$

where r = 5.7 cm is the radius of the viewport. The differential BBR shift can further be simplified through a Taylor expansion up to order $\delta T/T^3$, where $\delta T = T_{\mathrm{top}} - T_{\mathrm{bot}}$ is the temperature difference between the top and bottom viewports:

$$\begin{aligned}\nu_{\mathrm{BBR}} &= -2\frac{\alpha_{\mathrm{Sr}}\sigma_{\mathrm{SB}}}{h\epsilon_0 c}\frac{r^2}{4Z_0^3}\delta z_{ji}\,T^4\left[\left(1+\frac{\delta T}{T}\right)^4-1\right]\\ &\approx -2\frac{\alpha_{\mathrm{Sr}}\sigma_{\mathrm{SB}}}{h\epsilon_0 c}\frac{r^2}{4Z_0^3}\delta z_{ji}\,T^4\left[4\frac{\delta T}{T}+6\left(\frac{\delta T}{T}\right)^2+4\left(\frac{\delta T}{T}\right)^3+\mathcal{O}\left(\left(\frac{\delta T}{T}\right)^4\right)\right]\end{aligned} \tag{3.10}$$

Because the absolute temperature ($T = 300$ K) is a factor of 150× greater than the temperature difference we applied to the viewports ($\delta T \leq 2$ K), the magnitude of the first-order term is roughly a factor of 100× larger than the second-order term. Therefore, we can approximate Eq. (3.10) as an expression with a linear scaling with both δT and δz_{ji}:

$$\nu_{\mathrm{BBR}} \approx -2\frac{\alpha_{\mathrm{Sr}}\sigma_{\mathrm{SB}}}{h\epsilon_0 c}\frac{r^2}{4Z_0^3}T^3\times\delta z_{ji}\times\delta T \tag{3.11}$$

Measuring the frequency differences of the 10 ensemble pairs simultaneously, we find that as expected from Eq. (3.11), the resulting frequency shifts scale linearly with the temperature difference, and the corresponding slopes scale roughly linearly with the height differences,

see Fig. 3.3. Through a linear fit to the extracted slopes as a function of height differences, we find the BBR sensitivity in our system to be $-4.2(1) \times 10^{-18}$/cm per 1 K difference (Fig. 3.2**c**).

To monitor the temperature, we use commercially available 10 kΩ negative temperature coefficient thermistors (Amphenol Thermometrics, MC65F103A), rated for an interchangeability of 50 mK by the manufacturer. Relative accuracy of the temperature sensors is calibrated in an ice water bath, and we find the temperature differences between each sensor consistent within 25 mK. The temperature sensors are mounted on the stainless steel Conflat flanges of the top and bottom viewports, as well as the side flanges of the science chamber for monitoring the radial temperature inhomogeneity. Under normal operating conditions, we find the temperature difference between the top and bottom sensors lies within a range of 350 ± 100 mK and find the radial temperature inhomogeneity to be less than 75 mK.

The MOT coils are mounted in the recessed window of the science chamber, which could potentially introduce temporal thermal drifts during the sample preparation stage. To suppress this, we opt for compact coils with efficient water cooling through hollow wires, keep the ${}^1S_0 \leftrightarrow {}^1P_1$ first-stage MOT loading time (< 0.5 s) short compared to the experimental cycle time (12 s), and ensure that the duty-cycles remain consistent throughout the measurements.

While the strontium oven atom source (AOSense) is another potential source of BBR shift, the atom ensembles have no direct line of sight to the BBR photons from the oven thanks to the use of a 2D-MOT for atomic beam deflection. We operate the oven at the lowest possible temperature ($T = 360$ °C) under normal conditions, and find no statistically significant change in the frequency differences across the ensemble array at the 1×10^{-19}/cm level when intentionally increasing the oven temperature to 460 °C, a lever arm of 1.8 due to T^4 scaling bounds the systematic gradient from the oven to below 5.5×10^{-20}/cm.

Overall, for measurements taken under normal operations, we find the averaged temperature difference between top and bottom sensors to be 370(35) mK, resulting in a BBR gradient of $-15.7(1.5) \times 10^{-19}$/cm.

3.3.5 Lattice light shift

The lattice light shift for a single atomic ensemble is given by [118]:

$$\begin{aligned}\nu_{LS}(u, \delta_L, n_z) \approx & \left(\frac{\partial\tilde{\alpha}^{E1}}{\partial\nu}\delta_L - \tilde{\alpha}^{qm}\right)\left(n_z + \frac{1}{2}\right)u^{1/2} \\ & - \left[\frac{\partial\tilde{\alpha}^{E1}}{\partial\nu}\delta_L + \frac{3}{2}\tilde{\beta}\left(n_z^2 + n_z + \frac{1}{2}\right)\right]u \\ & + 2\tilde{\beta}\left(n_z + \frac{1}{2}\right)u^{3/2} - \tilde{\beta}u^2,\end{aligned} \tag{3.12}$$

in which $\tilde{\alpha}^{E1}$, $\tilde{\alpha}^{qm}$, and $\tilde{\beta}$ are the differential $E1$, $E2$-$M1$ polarizabilities, and hyperpolarizability on the clock transition, respectively. u is the lattice trap depth in units of E_{rec}, n_z is the axial vibrational quanta, and δ_L is lattice detuning from the effective magic wavelength,

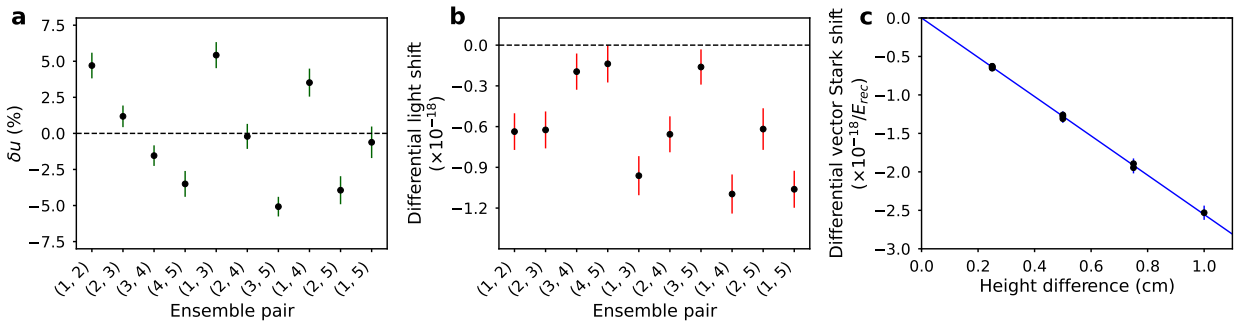


Figure 3.4: **Lattice light shift evaluation. a**, Extraction of relative trap depth difference δu for 10 ensemble pairs. The extracted δu are symmetric around 0, reflecting the Gaussian nature of the lattice beam profile and that the ensembles are centered about the beam focus. **b**, Evaluation of differential lattice light shifts at $u_{op} = 15\ E_{\mathrm{rec}}$ for 10 ensemble pairs. The shifts scale with spatial separation, but do not scale with δu, resulting in a residual spatial lattice light shift gradient of $-8.0(1.1) \times 10^{-20}/E_{\mathrm{rec}}/\mathrm{cm}$. **c**, Evaluation of the differential vector Stark shift, which also doesn't scale with δu. A linear fit (blue solid line) yields a gradient of $-2.5(2) \times 10^{-18}/E_{\mathrm{rec}}/\mathrm{cm}$.

where the scalar and tensor shifts cancel. The vector shift is rejected by averaging the transitions with opposite nuclear spin states. Through clock sideband thermometry both axially and radially we find $n_z < 0.01$ and radial temperature $T_r < 200$ nK at $u_{op} = 15\ E_{\mathrm{rec}}$, where thermal averaging of the effective trap depth can be neglected. By operating at lattice depths below 35 E_{rec}, the hyperpolarizability terms are also negligible.

To model the differential lattice light shift in our system, we introduce a dimensionless parameter δu, which characterizes the relative lattice trap depth difference between ensemble pair (i, j), where $j > i$

$$\begin{aligned} u_i &= u, \\ u_j &= u(1 + \delta u). \end{aligned} \tag{3.13}$$

For $\delta u \ll 1$, the differential light shift $(\nu_{LS,j} - \nu_{LS,i})$ can be approximated as

$$\Delta\nu_{LS}(\delta_L, \delta u, u) = \delta u \left[\left(\frac{\partial \tilde{\alpha}^{E1}}{\partial \nu} \delta_L - \tilde{\alpha}^{qm} \right) \frac{1}{4} \sqrt{u} - \frac{\partial \tilde{\alpha}^{E1}}{\partial \nu} \delta_L u \right], \tag{3.14}$$

which scales linearly with δu.

By modulating the lattice detuning between $\delta_L + 100$ MHz and $\delta_L - 100$ MHz at the operational depth $u_{op} = 15\ E_{\mathrm{rec}}$, we have

$$\begin{aligned} &\Delta\nu_{LS}(u_{op}, \delta_L + 100\ \mathrm{MHz}) - \Delta\nu_{LS}(u_{op}, \delta_L - 100\ \mathrm{MHz}) \\ &= \delta u \frac{\partial \tilde{\alpha}^{E1}}{\partial \nu} \left(\frac{1}{4} \sqrt{u_{op}} - u_{op} \right) \times 200\ \mathrm{MHz}, \end{aligned} \tag{3.15}$$

allowing extraction of δu, which are found to be below 5 % for all the ensemble pairs, and are symmetric around 0 (Fig. 3.4**a**), reflecting the Gaussian nature of the lattice beam profile and that the array is centered about the focus. Through mapping out the frequency shifts for 10 ensemble pairs when modulating the lattice intensity, we find the differential light shifts scale with the spatial separations between ensemble pairs but do not scale with δu, resulting in a residual spatial light shift gradient of $-8.0(1.1) \times 10^{-20}/E_{\rm rec}/{\rm cm}$ (Fig. 3.4**b**).

Although the origin of the spatial light shift gradient is not definitively known, we also observe a differential lattice vector Stark gradient of $-2.5(2) \times 10^{-18}/E_{\rm rec}/{\rm cm}$ by measuring the splitting between transitions with opposite spin states (Fig. 3.4**c**), which also does not scale with δu and instead scales with trap depth and spatial separation. For a single ensemble, the vector Stark shift is proportional to $\xi_{\rm lat}(\hat{e}_k \cdot \hat{e}_B)$, where $\xi_{\rm lat}$ is the ellipticity of the lattice light, $\hat{e}_k$ is the lattice wave vector along $\hat{z}$ direction, and $\hat{e}_B$ is the magnetic field vector primarily along $\hat{x}$. We find the vector Stark gradient arises from the spatially varying coefficient, $\hat{e}_k \cdot \hat{e}_B$, verified through the change of vector Stark gradient by applying an additional magnetic field gradient $\partial B/\partial z$ of up to ± 10 mG/cm, which effectively changes $(\hat{e}_k \cdot \hat{e}_{B,j} - \hat{e}_k \cdot \hat{e}_{B,i})$. Based on this observation, we hypothesize that the residual spatial light shift gradient is due to a differential tensor Stark shift, in which the spatially varying magnetic field vectors are coupled to the (nearly) linear lattice polarization ($\hat{e}_{\rm lat}$, along $\hat{x}$) through $|\hat{e}_{\rm lat} \cdot \hat{e}_B|^2$. The differential vector Stark shift results in a gradient of $-37(3) \times 10^{-18}/{\rm cm}$ at $u_{op} = 15\ E_{\rm rec}$ in the splitting between transitions with opposite spin states, equivalent to a fictitious magnetic field gradient of $\sim 600\ \mu$G/cm and is accounted for during the second-order Zeeman shift corrections.

To independently evaluate the light shift gradient, we need to account for the δu dependent shifts, which require the knowledge of δu and δ_L. The latter is done by first subtracting the residual spatial gradient from the measured differential light shifts. We then find that the remaining shifts are correlated with the extracted δu (Fig. 3.2**d**) as expected from Eq. 3.14. From this we find our operational lattice detuning δ_L to be 16.9(1.5) MHz. With the extracted δ_L and δu calibrated from each measurement day, we are able to monitor and account for the residual light shift gradient. A representative plot is shown in Fig. 3.2**e**.

Our operational lattice frequency is measured to be $368,554,780(30)$ MHz, limited by the accuracy of the wave-meter (HighFinesse, WS7). However, the lattice frequency is stabilized to a ultra-low-expansion cavity with typical drifts of less than -20 kHz per day, inferred from the narrow-linewidth ${}^1S_0 \leftrightarrow {}^3P_1$ MOT, providing sufficient long-term stability throughout the measurements. The lattice intensity is actively stabilized and controlled via feedback to the acoustic-optical modulator before the beam delivering optical fiber (NKT Photonics, LMA-PM-15). Both the incoming and retro-reflected lattice alignments are monitored on several cameras and photo-diodes, ensuring the daily-calibrated δu remained symmetric around 0 throughout the data taking campaign. Overall, the lattice light shift gradient in our system is evaluated to be $-11.8(1.2) \times 10^{-19}/{\rm cm}$.

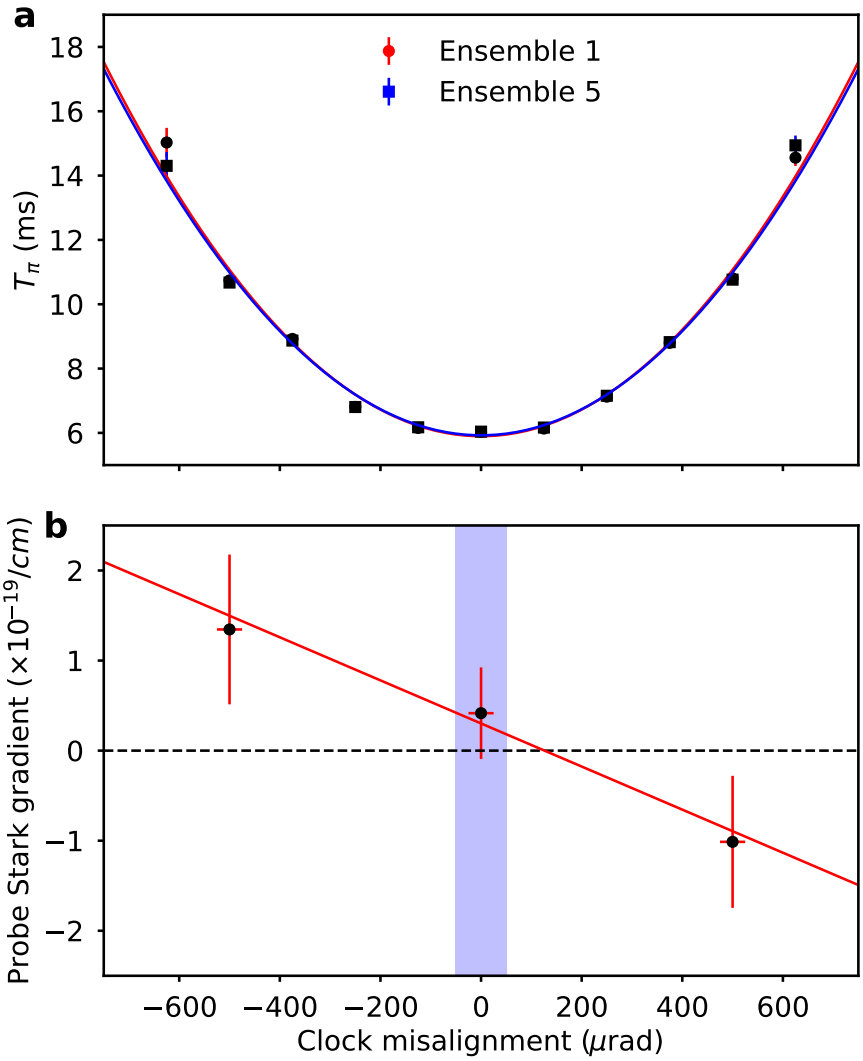


Figure 3.5: **a**, Measured π pulse durations T_π for ensemble 1 (red) and 5 (blue), the pair with largest spatial separation (1 cm), as a function of the angle of clock beam misalignment. The solid lines are quadratic fit to the data. **b**, Evaluated probe Stark shift at the operational intensity I_{op} at ± 500 μrad clock beam misalignment (estimated using camera). A linear fit to the data bounds the probe Stark shift gradient to be below 0.5×10^{-19}/cm (the blue area represents a ± 50 μrad range).

3.3.6 Probe Stark shift

The probe AC Stark shift arises from the clock light itself, and is suppressed when probing with a shared clock light, with uncertainties primarily arising from inhomogeneity and

misalignment of the clock beam with respect to the lattice. The clock light beam waist is ~ 1 mm, a factor of 10 greater than that of the lattice, ensuring homogeneity across the atomic ensembles both axially and radially. The clock light is carefully aligned to the lattice light, and is monitored using several cameras by picking-off the beam before and after the science chamber over a distance of ~ 2.5 m. The alignment is further verified by ensuring that the time periods of the clock transition Rabi oscillations of all 5 ensembles agree within 1% fitting uncertainty before and after each measurement run.

Evaluation of the probe Stark effect is performed by interleaving between the operational clock intensity of I_{op}, corresponding to a π pulse duration of 6 ms, and the case of $4I_{op}$. This interleaved measurement is repeated by further misaligning the clock beam by up to ± 500 μrad (estimated via camera images), at which the π pulse durations increase by about a factor of 2 (Fig. 3.5). Through linear fitting, we find a frequency gradient of $2.5(1.0) \times 10^{-19}$/cm across the span of ± 500 μrad misalignments. Under normal operations, the misalignment is monitored and bounded within a ± 50 μrad range which accounts for possible drifts during the experiments. This bounds the uncertainty from probe Stark shift to below 0.5×10^{-19}/cm.

3.3.7 DC Stark shift

Frequency shifts arising from electric fields can perturb the clock transition through DC Stark effect of the form kE^2, where $E = |\widehat{\mathrm{E}}|$ is the static electric field and $k \equiv -(\alpha_e - \alpha_g)/(2h)$ is the coefficient specific to the clock transition, with $\alpha_{g,e}$ being the static polarizabilities of the ground and excited clock states. To evaluate the DC Stark effect, a pair of quadrant electrodes are mounted along the lattice axis outside the top and bottom science chamber viewports, with a total separation of roughly 30 cm. We then probe the clock transition with opposite voltages applied to the electrode pair and interleave between $(+V, -V)$ and $(-V, +V)$ configurations. We observe differential shifts below the 1×10^{-19}/cm level when applying voltages of up to ± 100 V to the electrodes, indicating that the background electric field gradient is small.

To quantify our uncertainty in the differential shifts due to the background electric field gradient, we follow the approach laid out in Ref. [122]. In the presence of a background field E_{bg}, which would most likely arise due to charge accumulation on the nearby top and bottom viewports, the DC Stark shift for a single atom ensemble is given by $k(E_{bg} + cV)^2$, where c is the atomic coefficient. We rewrite the above form as [122]

$$\nu_{dc}(V) = \nu_{bg} + aV + bV^2, \tag{3.16}$$

where ν_{bg} is the background stray field shift, and coefficients a and b are experimentally accessible parameters by modulating V. We note that aV represents the coupling between the background field and the applied field. When comparing ensemble i and ensemble j $(j > i)$, the differential DC Stark shift $(\Delta\nu_{dc} = \nu_j - \nu_i)$ becomes

$$\Delta\nu_{dc}(V) = \Delta\nu_{bg} + AV + BV^2, \tag{3.17}$$

where $A = a_j - a_i$, $B = b_j - b_i$, and $\Delta\nu_{bg} = \nu_{bg,j} - \nu_{bg,i}$ is the differential background shift due to charges on the viewports.

Due to the finite spatial extent (s) of the atom ensembles and inhomogeneity of the applied field, there is no V such that the applied field identically cancels $\Delta\nu_{bg}$. We consider the extremum value of $\Delta\nu_{dc}(V)$, denoted as $\Delta\nu^*$. We then have the difference between the differential background shift and the extremum shift, $\Delta\nu_{\text{diff}} \equiv \Delta\nu_{bg} - \Delta\nu^*$ (refer to Fig. 1 in Ref. [122] for details). From Eq. 3.17, we find $\Delta\nu_{\text{diff}} = A^2/(4B)$. We note that $\Delta\nu^*$ plays the role of a frequency correction for the field gradients, and can be written as $\Delta\nu^* = \eta\Delta\nu_{\text{diff}}$, due to the fact that $\Delta\nu^*$ and $\Delta\nu_{\text{diff}}$ scale similarly with the stray field. The differential background shift is then given by

$$\Delta\nu_{bg} = (1+\eta)\Delta\nu_{\text{diff}} = (1+\eta)A^2/(4B), \tag{3.18}$$

in which η is given by $\eta = \zeta^2 s^2/R^2$ to leading order of s, where $\zeta \equiv (q_1+q_2)/(q_1-q_2)$ quantifies the charge symmetry between the viewports, and R is the effective length.

By applying voltages of up to ± 100 V to the electrodes, we find $A^2/(4B) = 0.6(3)\times 10^{-20}$ for the ensemble pair of 1 cm separation. In our system, we obtain $\eta \approx 0.02$ for $s = 500$ μm, $R = 40$ mm, and assuming 25% more charge on one viewport than the other. This bounds the background DC Stark shift gradient to below 0.1×10^{-19}/cm.

3.3.8 Ellipse fitting

In the presence of QPN and numerical constraints which ensure an ellipse-specific solution, the least squares ellipse fitting approach is biased at phases close to 0 or π where the ellipse collapses into a straight line [73]. The differential phases across the ensemble array are dominated by the differential Zeeman shifts, such that through precise control of the magnetic field and gradient, we can operate in the regime where all the differential phases lie within the $(\pi/6, 5\pi/6)$ range. For typical experiments with a 10 s Ramsey dark time and 2000 atoms per ensemble, the ellipse fitting bias error is bound to below 2×10^{-19} (Fig. 3.6). During initial data processing, the bias error is corrected using Monte-Carlo simulations with the experiment parameters such as atom number and contrast as inputs. While the bias error does not scale with spatial separations, we estimate an upper bound limit of 0.5×10^{-19} due to uncertainty in the input parameters used for Monte-Carlo simulation during bias error corrections.

3.3.9 Wannier-Stark ladder, imaging, and the expected gravitational redshift

The local gravitational acceleration in our laboratory was measured by the group of Prof. Tikoff from the Department of Geoscience at the University of Wisconsin-Madison using a LaCoste-Romberg gravimeter, and was then cross-validated with known values from several other survey points in Wisconsin. The local gravitational acceleration in our laboratory was measured to be $g = -9.803$ m/s^2, rounded to the 4$^{\text{th}}$ digit.

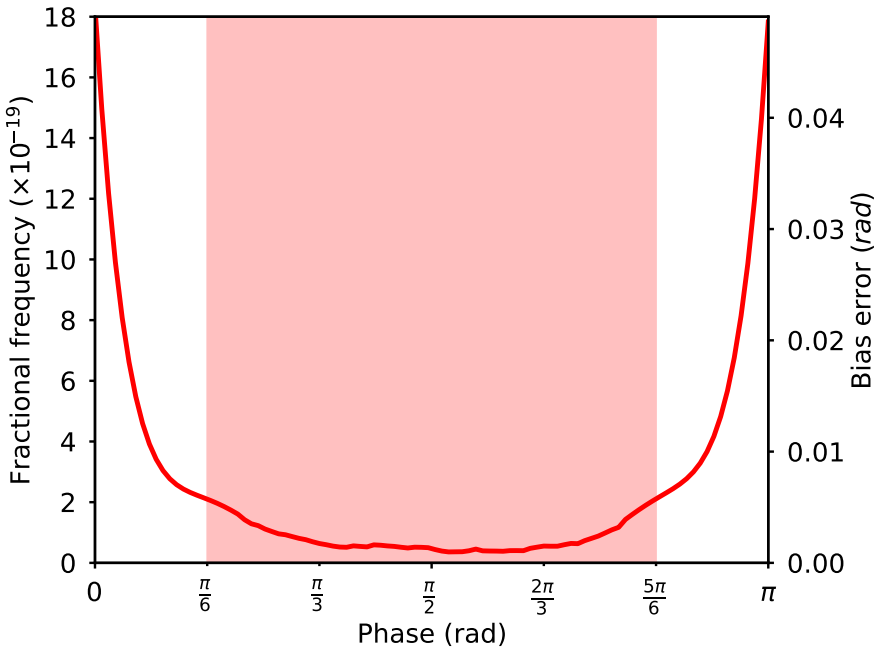


Figure 3.6: Monte-Carlo simulations of bias error from ellipse fitting with input parameters of 2000 atoms per ensemble, 85% contrast and 10 s Ramsey dark time (red solid line). The red area represents our normal operating range of $(\pi/6, 5\pi/6)$, where fractional bias error is bound below 2×10^{-19} and is corrected for each ellipse fitting during data analysis with uncertainty below 0.5×10^{-19}.

The lattice tilt (θ_{tilt}) with respect to gravity is independently measured using the splitting of the $\pm 1^{\text{st}}$ order Wannier-Stark sidebands [70] to the clock transition at 5 E_{rec} lattice depth (Fig. 3.7**a**), which is given by

$$\Delta\nu_{\text{WS},\pm 1} = mg\lambda_L \cos\theta_{\text{tilt}}, \tag{3.19}$$

where m is the mass of ^{87}Sr, and $\lambda_L = 813.4$ nm is the lattice wavelength. A representative plot of the measured Wannier-Stark sidebands is shown in Fig. 3.7**b**, and we find the weighted average splitting between $\pm 1^{\text{st}}$ order sidebands to be 1729(2) Hz, corresponding to a tilt with respect to gravity of 5.0(1)°.

The overall spatial extent of the ensemble array is 1.00(1) cm, calculated based on the frequency chirp profile of the moving optical lattice loading sequence, which is precisely controlled using a direct digital synthesizer (DDS, Moglabs XRF). This yields an effective height difference of $\Delta h = 0.99(1)$ cm, consistent with the extraction of the height difference from the camera images. The effective camera pixel size in our imaging system is calibrated to be 34(1) μm per pixel using the standard time-of-flight imaging.

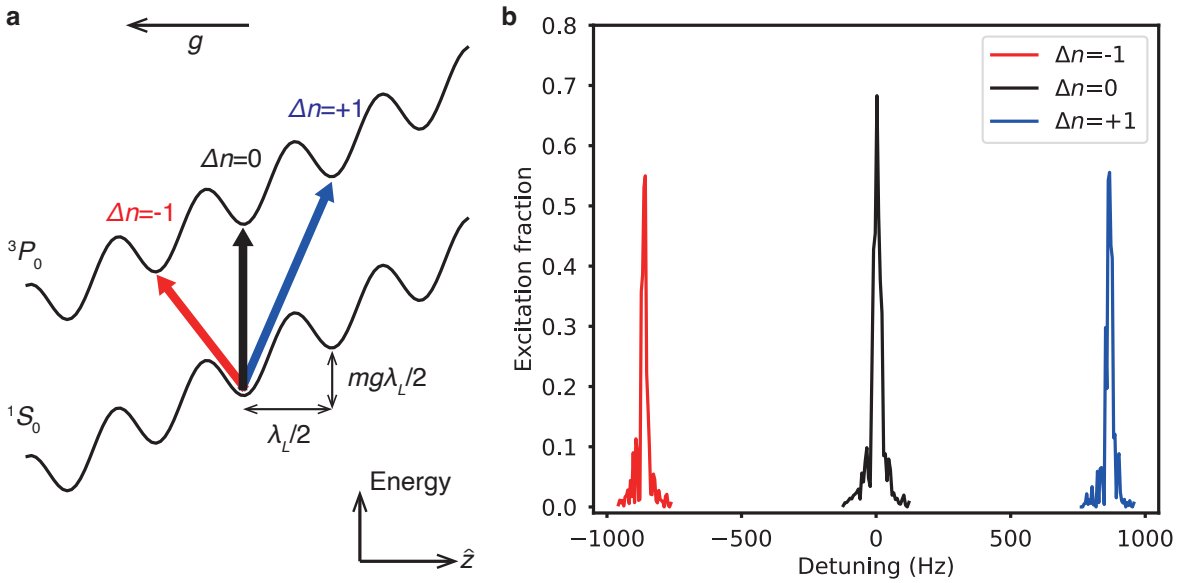


Figure 3.7: **a**, Illustration of the Wannier-Stark ladder in a 1D vertical optical lattice along the $\hat{z}$ direction. The Wannier state at lattice site n has energy $nmg\lambda_L/2$. The black arrow represents the carrier clock transition where n remains unchanged ($\Delta n = 0$). The blue (red) arrow represents the first-order sideband transition with $\Delta n = +1(-1)$. **b**, Representative plot of measured Wannier-Stark sidebands at a shallow lattice depth (5 E_{rec}) recorded with Fourier-limited Rabi spectroscopy with a π pulse duration of 40 ms. The black line corresponds to the carrier ($\Delta n = 0$) transition, and the blue (red) line corresponds to off-site transitions, $\Delta n = +1(-1)$. The splitting between $\Delta n = \pm 1$ transitions is used to extract the lattice tilt.

Fluctuations of background magnetic fields modifying the narrow-line MOT operation could result in position drift in the atom ensemble. This is rejected by identifying the center-of-mass of each ensemble with a 2D Gaussian fit, followed by a selection of region-of-interest (ROI) with a 15 pixel by 15 pixel region centered on the fit. Each ensemble has a finite vertical spatial extent of roughly 500(10) μm, corresponding to an expected gradient of $-5.5(1) \times 10^{-20}$ across the ensemble due to the gravitational redshift, which is averaged out by spatial averaging over the ROI in order to extract the redshifts between the center-of-mass positions of each ensemble. The center-of-mass position uncertainty of each ensemble is limited by the DDS timing accuracy (100 ns), corresponding a position error of < 0.1 μm.

The expected gravitational redshift from theory of general relativity at a 1 cm height difference is then given by

$$\frac{g\Delta h}{c^2} = -10.9 \times 10^{-19}, \tag{3.20}$$

where c is the speed of light. This results in an expected redshift gradient of -10.9×10^{-19}/cm,

with the uncertainty bounded $< 0.1 \times 10^{-19}$/cm due to uncertainties in g and Δh.

3.4 Measurement of the gravitational redshift

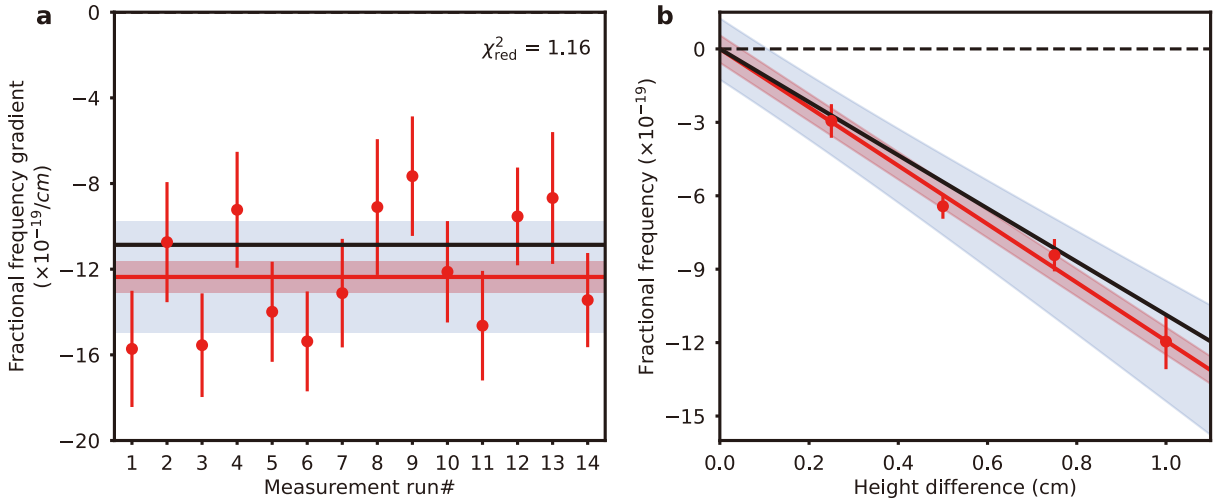


Figure 3.8: **a**, The measured fractional frequency gradients after accounting for all systematic corrections over 14 data taking runs (red scatter points), each of duration ranges from 1 to 4 hours. The weighted average (red solid line) yields a measured gradient of $[-12.4 \pm 0.7_{(\mathrm{stat})} \pm 2.5_{(\mathrm{sys})}] \times 10^{-19}$/cm, consistent with the expected redshift gradient (black solid line). Red (blue) area represents $\pm 1\sigma$ statistical (total) uncertainty, in which the statistical uncertainty is inflated by the square root of the reduced χ^2 statistic, $\chi^2_{\mathrm{red}} = 1.16$. The error bars correspond to 1σ standard deviation. **b**, Mean differential frequencies as a function of height difference across all measurements (red scatter points), analyzed using the same data set as in **a**. A linear fit (red solid line) yields a fractional frequency gradient of $(-11.9 \pm 2.6) \times 10^{-19}$/cm, again fully consistent with the expected redshift gradient (black solid line).

We performed 14 blinded measurement runs of gravitational redshift data under normal operating conditions over a 3-week campaign. Each run ranged in duration from 1 to 4 hours, and was performed in conjunction with verification of several experimental parameters to ensure that the associated systematic effects are under control, such as the magnetic field gradient, density shift coefficients, δu, and clock and lattice beam alignments (See Methods). In each measurement run, the differential frequency of each ensemble pair was extracted through ellipse fitting, with the associated Allan deviation extrapolated to the full averaging time taken as the statistical uncertainty. The corrections for density shifts and bias error from the ellipse fitting are applied to each ensemble pair individually. The total uncertainty of each clock comparison is given by the quadrature sum of its statistical uncertainty and the

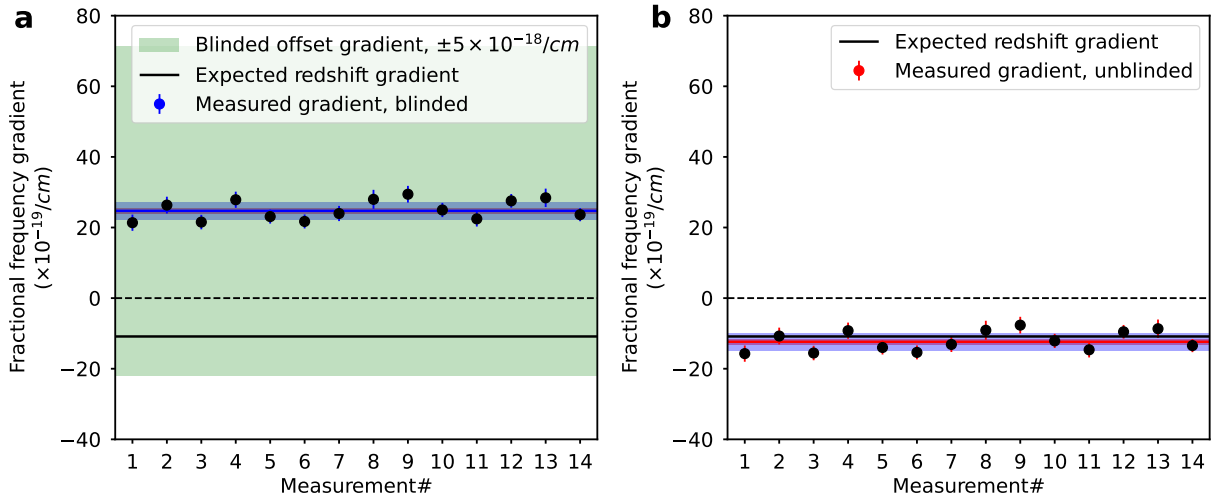


Figure 3.9: **a**, Measured fractional frequency gradients (blue scatter points) with blinded offset. The blue area represents $\pm 1\sigma$ total uncertainty. The black solid line is the expected gravitational redshift gradient of -10.9×10^{-19}/cm. The green area represents the range of possible outcomes upon removal of the blinded offset gradient, corresponding to a $\pm 5 \times 10^{-18}$/cm range. All corrections and uncertainties were finalized at this stage, without knowledge of the blinded offset. **b**, Measured fractional frequency gradients following removal of the blinded offset. Red scatter points are the same data set as in **a** with the blinded offset gradient ($+3.7 \times 10^{-18}$/cm) removed. This represents the same data shown in Fig. 3.8**a**, but here the scale of the y-axis is kept the same as in panel **a** for the sake of comparison.

uncertainties of systematic corrections. We analyze the measured frequency gradient using two approaches.

In the first approach, the extracted frequency differences for 10 ensemble pairs from each measurement run are plotted as a function of the height differences. A linear fit is applied to each measurement run. Many of the clock comparison pairs share a clock, e.g., pair (1, 2) and pair (2, 3) share clock 2. This means that the quantum projection noise is partially correlated between pairs, and not accounting for this would result in an underestimation of the error bar associated with the fit. To account for this, the covariance matrix is included in the fitting algorithm, where the covariance between clock pairs (a, b) and (b, c) is given by the jackknifing re-sampling approach [56]

$$\mathrm{Cov}(\phi) = \frac{N-1}{N} \sum_i \left(\bar{\phi}_{ab}^{JK} - \bar{\phi}_{ab,\neq i}^{JK} \right) \left(\bar{\phi}_{bc}^{JK} - \bar{\phi}_{bc,\neq i}^{JK} \right), \tag{3.21}$$

where $\bar{\phi}_{\neq i}^{JK}$ is the extracted phase except the i^{th} data point, $\bar{\phi}^{JK}$ is the mean of $\bar{\phi}_{\neq i}^{JK}$, and N is the total number of measurements.

The associated fitted slopes from 14 measurement runs, after accounting for systematic gradient corrections, are then weighted averaged, yielding a statistical uncertainty of 0.7×10^{-19}/cm, inflated by the square root of the reduced χ^2 statistic, $\chi^2_{\text{red}} = 1.16$ (Fig. 3.8**a**). Upon completion of the measurements, the pseudo-randomly generated offset blinding gradient was revealed and subtracted from the measurements. The offset gradient proved to be $+3.7 \times 10^{-18}$/cm, and the measurements before and after unblinding are shown in Supplementary Figure 8. We find a weighted mean frequency gradient of $[-12.4 \pm 0.7_{(\text{stat})} \pm 2.5_{(\text{sys})}] \times 10^{-19}$/cm, consistent with the expected redshift gradient of -10.9×10^{-19}/cm within 1σ total uncertainty.

In the second approach, we re-analyze the data and apply systematic corrections to each pairwise clock comparison individually over the same raw data set. For each pair, the total uncertainty is calculated as the quadrature sum of the standard error of its weighted mean, systematic uncertainties that don't scale with height difference (density shift and ellipse fitting corrections), and other systematic uncertainties that scale with height difference. The weighted averaged frequency differences of each ensemble pair are given in Supplementary Table 1. Through a final linear fit to the differential frequencies as a function of the height differences, we find a frequency gradient of $(-11.9 \pm 2.5) \times 10^{-19}$/cm (Fig. 3.8**b**), again fully consistent with the expected redshift gradient within 1σ total uncertainty.

To eliminate possible bias of our data taking and systematic analysis towards an expected outcome, we employ a data blinding protocol. Our data software adds a large constant offset gradient to our measurements, including the data taken for systematic evaluations and data runs taken under normal operating conditions. The blinded offset gradient is pseudo-randomly drawn from a uniform distribution spanning over $\pm 5 \times 10^{-18}$/cm, 10 times the size of the expected redshift gradient. The blinded offset gradient is scaled by the height difference between each ensemble pair, and is then automatically added to the results from our data analysis code for ellipse phase extraction.

The blinded offset gradient was only unblinded after finalizing the corrections for all systematic effects, determining the measured value with blinded offset gradient taken under normal operating conditions, and finalizing the associated statistical and systematic uncertainties. No additional data was taken and no changes were made to the analysis, the error budget, the measured value, or the uncertainties after unblinding.

3.5 Relativistic clock height difference measurements

Assuming that the theory of general relativity is correct and that the gravitational redshift is given by Eq. 3.1, and treating the ensemble array as a network of spatially distributed clocks with unknown heights, we demonstrate a relativistic gravitational potential measurement [30, 32, 98] using synchronous clock comparisons (Table 3.1). The height difference Δh for each clock pair is then given by

$$\Delta h = \frac{\delta f}{f} \frac{c^2}{g}, \tag{3.22}$$

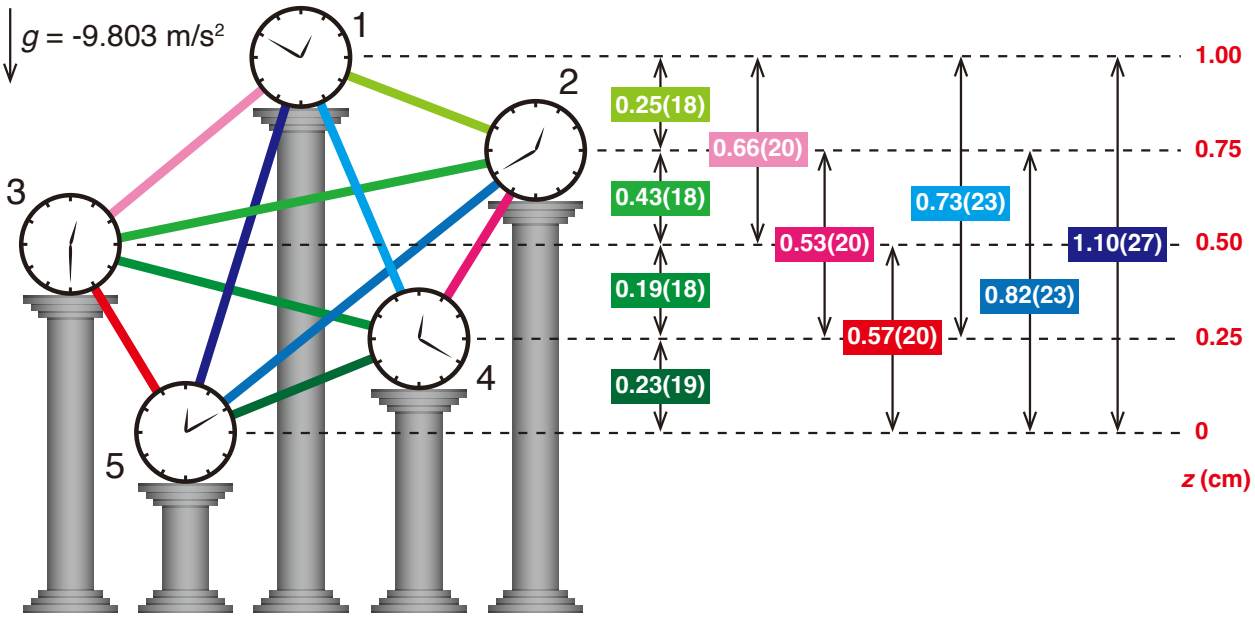


Figure 3.10: **a)** The relative clock height differences across the array are determined using the measured gravitational redshifts and the independently measured local gravitational acceleration g. The double arrows represent the extracted height difference and the associated uncertainty for each clock pair. The true clock heights are shown on the right (red values), with the lowest clock (clock 5) defined as being at a height of 0 cm. All units are in cm unless otherwise specified. The uncertainties correspond to 1σ standard deviation.

where δf is the measured gravitational redshift, g is the independently measured local gravitational acceleration ($g = -9.803$ m/s^2), f is the clock transition frequency, and c is the speed of light. The uncertainties of the extracted height differences are dominated by the systematic uncertainties of the measured gravitational redshifts.

3.6 Context and discussion

The measurement of gravitational potential differences between clocks with sub-centimeter resolution is a major goal of relativistic geodesy [29–32, 98]. In the preceding discussion and analysis we treated the height differences between each ensemble pair and the local gravitational acceleration g as known, as we measure them independently, but did not *a priori* trust the gravitational redshift predicted by general relativity. From another perspective, our measurements can be viewed as a proof-of-principle demonstration of relativistic gravitational potential measurement with millimeter scale resolution. Taking as a given that the redshift is given by Eq. 3.1 and treating the ensemble array as a network of spatially distributed clocks with unknown height differences, we can extract the height ordering and relative height

differences from the measured gravitational redshifts and g, which we measure independently. We find that we correctly assign the order of gravitational potential differences within the network, and that all of the extracted height differences are within 2 mm of the known values (Fig. 3.10). However, we note that we greatly benefit from the rejection of common-mode systematic shifts thanks to the ensembles sharing the same optical lattice and the same science chamber, which will not be possible when comparing two individual clocks at different geospatial locations. In addition, over a long baseline (> 1 km), phase noise from the frequency transfer will not be common-mode and will limit the coherence times of the differential comparison. Therefore, while these results demonstrate that relativistic gravitational potential measurements with mm-scale height resolution are achievable in the lab over short spatial separations, considerable challenges must be overcome before they can be applied to relativistic geodesy at length scales of interest.

In a recent work [103], Bothwell and collaborators resolved the gravitational redshift across a single 1 mm atom ensemble. While there are aspects in common between this work and Ref. [103], there are also several critical differences that set this work apart. First, we employed a blinded offset during data taking and systematic evaluation. Second, while Bothwell et al. made use of second-scale Rabi spectroscopy with an 8 mHz linewidth clock laser, we demonstrate comparable levels of differential stability and perform a full systematic evaluation at the 10^{-19} level by employing synchronous Ramsey spectroscopy with a Hz linewidth clock laser. This demonstrates that measurements of this kind need not be limited by the stability of the local oscillator. Third, we measure between spatially resolved ensembles using techniques that are likely more relevant to applications that require spatially separated clocks such as relativistic geodesy and gravitational wave detection. Finally, we also observe and characterize several systematic effects that were not observed by Bothwell et al., such as a black-body radiation gradient shift and differential tensor lattice light shift, likely in part because of the larger range of spatial separations used in our work.

Chapter 4

Measurement of the natural lifetime of the $^3P_0$ clock state in ^{87}Sr

This chapter was previously published as Jonathan Dolde, Dhruva Ganapathy, Xin Zheng, Shuo Ma, Kyle Beloy, and Shimon Kolkowitz. "Direct measurement of the $^3P_0$ clock state natural lifetime in ^{87}Sr". In: Phys. Rev. A *112.2 (Aug. 2025), p. 023121.* DOI: *10.1103/f6pt-flnt.*

4.1 Introduction

In the previous chapters, we have seen very good ground state atomic lifetimes in our optical lattice, up to 95 s in our apparatus. As these lifetimes are comparable to the measured and theorized $^3P_0$ lifetime (≈160 s), we recognize that we could make a precise measurement of the $^3P_0$ lifetime with our apparatus. In this chapter, we discuss our work in performing this measurement.

Over the past two decades optical atomic clocks have rapidly developed into the most precise and accurate frequency references ever realized [69], with clocks based on neutral strontium (Sr) now demonstrating fractional frequency accuracy at the level of 8.1×10^{-19} [67], and clock instabilities down to $4.8 \times 10^{-17}/\sqrt{\text{Hz}}$ [100]. These Sr optical lattice clocks make use of the transition between the $5s^2\ ^1S_0$ and $5s5p\ ^3P_0$ state, both of which are magnetically insensitive states due to their lack of electronic angular momentum. While this transition is completely forbidden by selection rules, hyperfine interactions from the nuclear spin of ^{87}Sr induce state mixing within the $5s5p\ ^3P_J$ manifold, creating a narrow optical transition near 429 THz [45] that balances the competing requirements of a long excited state lifetime with a sufficient transition dipole moment to enable coherent excitation with moderate clock laser intensities. ^{87}Sr based systems have therefore now been used for tests of the gravitational redshift down to cm and mm scales [12, 84, 103], to constrain ultra-light dark matter coupling [24, 124], for clock frequency ratio measurements toward a redefinition of the SI second [124–126], and for relativistic geodesy [30, 32, 127], and have also been proposed

as leading candidates for long-baseline optical clock atom interferometers [128, 129] and quantum computing [130].

The ultimate limit to the achievable coherent interrogation time of a clock measurement is set by the lifetime of the excited clock state. Theory calculations predict a lifetime for the $^3P_0$ state in ^{87}Sr of >100 s, with calculated values ranging from 110(30) s to 156(9) s [131, 132]. Experimentally measuring this value more precisely will allow for better estimations of the sensitivities and bandwidths that can be achieved in existing and future platforms that make use of the ^{87}Sr clock transition. For example, the excited state lifetime is a contributing factor in estimating the sensitivities of future clock-based gravitational wave detectors in space [26].

An accurate measurement of such a long excited state lifetime is made challenging by competing decay processes in an optical trap. These include optical lattice trap-induced Raman scattering, black-body radiation (BBR) induced scattering, background gas collisions, inelastic scattering from collisions between excited state atoms, and other mechanisms of loss of atoms from the lattice. To the best of our knowledge, the only previously reported direct measurement was made by Dörscher et al. [133], in which ^{87}Sr atoms were loaded into a 1-D optical lattice trap, initialized in the excited state, and held for varying time intervals, after which the populations of the ground and excited states were measured. However, the extraction of the $^3P_0$ lifetime from these measurements was particularly constrained by the vacuum-limited lifetime of 6 s, which was far below their reported value of 330(140) s.

While the ^{87}Sr lifetime can be inferred from a measurement of the dipole matrix element of the $^1S_0$ to $^3P_0$ transition, the two other reported values [134, 135] that use this method disagree with each other well beyond what would be expected based on their statistical and systematic uncertainties, indicating that one or both of these measurements may be limited by additional systematic uncertainties, and motivating direct measurements of the quantity of interest.

In this chapter, we perform direct lifetime measurements similar to those of Dörscher et al. However, we take advantage of significantly longer trapped-atom lifetimes and also introduce the concept of making simultaneous measurements of multiple ensembles at high and low density, and with both ^{87}Sr and ^{88}Sr . This allows us to isolate the contribution of radiative decay from other competing rates, obtaining a natural lifetime of 167^{+79}_{-40} s for the $^3P_0$ state in ^{87}Sr. Inspired by the concepts of "erasure conversion" and mid-circuit measurement from quantum computing with alkaline-earth atoms, we also confirm the consistency of our measurements and the extracted rates by performing novel measurements in which the population decaying into the ground state is repeatedly measured while the population remaining in the excited state is left undisturbed and continues to decay.

4.2 Lifetime measurement setup

In order to measure the lifetime of the $^3P_0$ state of ^{87}Sr, we load ensembles of ^{87}Sr or ^{88}Sr into a vertically oriented 1-D optical lattice at the 'magic' wavelength of 813.4 nm (see Fig. 4.1)

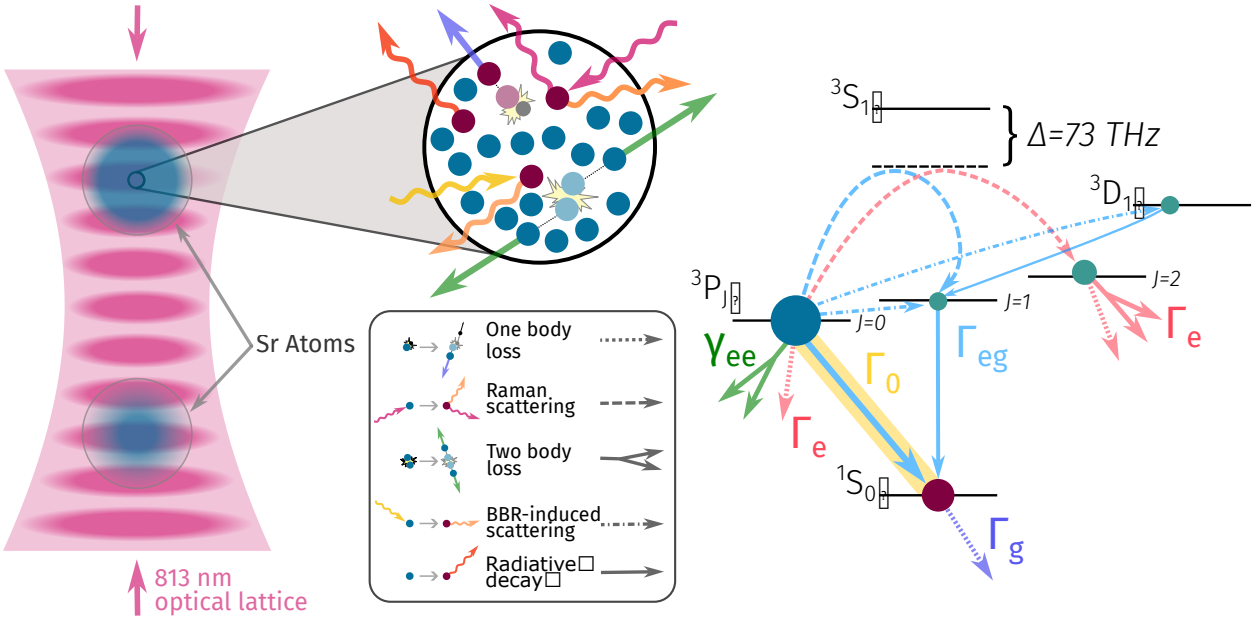


Figure 4.1: Population decay in an optical lattice. Two ensembles of ^{87}Sr or ^{88}Sr atoms are loaded into an optical lattice (left) and prepared in the excited $^3P_0$ state. The zoomed-in portion of the atomic ensemble shows atoms that have decayed into the $^1S_0$ ground state (red) and atoms that remain in the excited state (blue), along with the decay and loss mechanisms considered in our model. These processes are also represented using different line styles in a Sr level diagram (right). The line colors correspond to different parameters in the rate equation (see Eq. (4.1)). These include one-body losses, Γ_g and Γ_e, from the ground and excited states, two-body loss, γ_{ee}, and decay rate from excited to ground state, Γ_{eg}. The radiative decay rate, Γ_0, corresponding to the natural lifetime of the clock state, is highlighted in yellow.

for the Sr clock transition [59]. Our loading sequence starts with a standard two-stage magneto-optical trap (MOT), which cools the atoms to ∼1 μK. As the atoms are cooled, they fall into the overlapping optical lattice potential. Multiple spatially resolved atomic ensembles are then loaded into different regions of the lattice by modulating the zero-field point of the narrow-line second-stage MOT with additional bias coils [136]. The atom number in each ensemble is controlled by varying the duration of time for which the narrow-line MOT is overlapped with the lattice at each location. We operate with two ensembles separated by 0.8 millimeters, and with a factor of three difference in atom numbers in order to separate out the effects of density-dependent two-body loss. Once these ensembles are loaded into the lattice, we employ sideband and radial cooling and then ramp the lattice intensity from the loading depth of ∼70 E_{rec} to ∼8 E_{rec} to filter out hotter atoms. The recoil energy is given by $E_{\mathrm{rec}} = h^2/(2\mathrm{m}_{87(88)}\lambda^2)$, where m_{87} is the atomic mass of ^{87}Sr(^{88}Sr), λ = 813 nm is the wavelength of the lattice laser and h is Planck's constant. The lattice is then ramped back up to our operational depth, between ∼(20 and 65)E_{rec}. Finally, we initialize our ensembles into

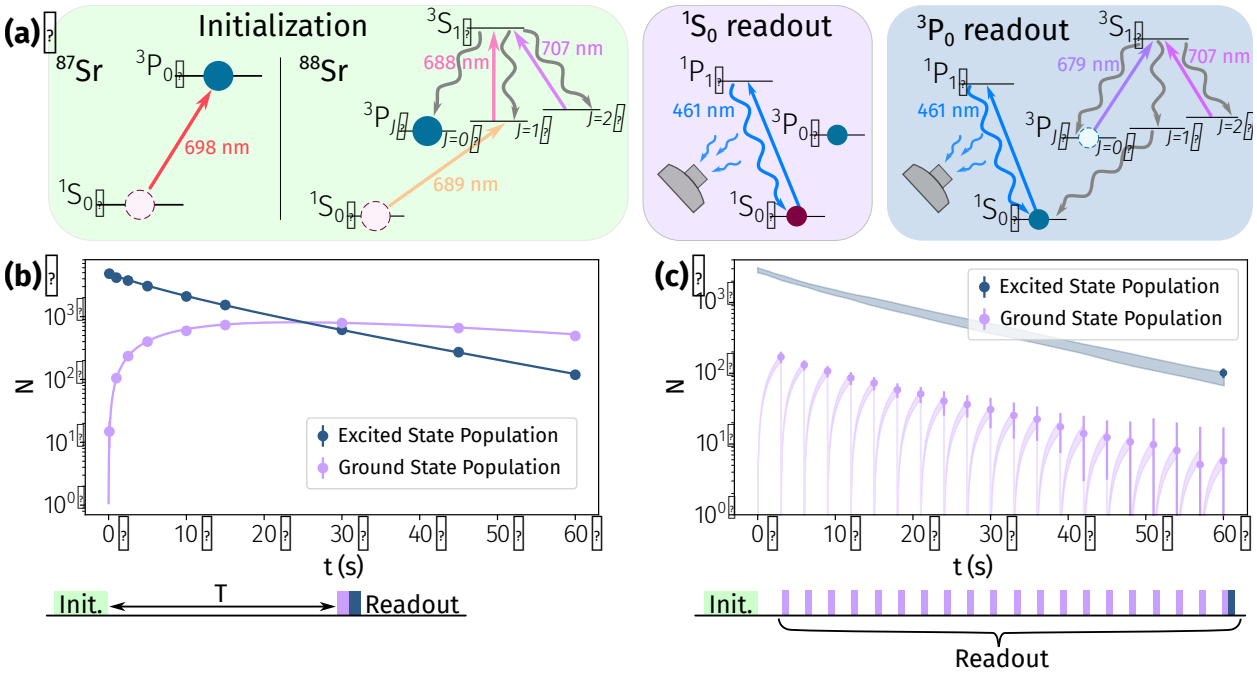


Figure 4.2: Population decay measurement scheme and example data for ^{87}Sr loaded at 40 E_{rec}. **a)** After loading, ^{87}Sr atoms are directly initialized in the $^3P_0$ excited clock state using a π-pulse. In ^{88}Sr, the atoms are first initialized in the $^3P_1$ state, then are optically pumped into $^3P_0$ via the $^3S_1$ state. The readout procedure is the same for ^{87}Sr and ^{88}Sr; the $^1S_0$ ground state population is read out using fluorescence from the $^1P_1$ state after a 461 nm cycling pulse. The excited state population is excited to the $^3S_1$ state where it decays to the ground state via the $^3P_1$ state and is then read out. **b)** In the standard measurement, the atoms are prepared in the excited state using a π-pulse and allowed to decay for time T, after which the ground (purple) and excited (blue) state populations are read out destructively. This process is repeated while varying T, and the resulting decay curves are fit to the rate equations for the state populations. The data points and error bars result from averaging over 10 sets of population data. This representative plot is of high-density ^{87}Sr atoms held at a trap depth of $\approx 40E_{\text{rec}}$. **c)** In the multi-readout measurement, the ground state population is read out at regular time intervals within a single experiment sequence, while atoms in the excited state are unaffected and continue to decay. The data points and error bars are obtained by median averaging the data over 48 experimental runs. The final readout destructively measures populations of both states. In order to estimate the initial population of the excited state, the atoms are prepared using a $\pi/2$ pulse and the remaining ground state population is destructively read out immediately at $t = 0$. The model curves use parameters inferred from the standard measurement. The shaded region indicates the uncertainty in model parameters.

the excited clock state, $|^3\mathrm{P}_0,\ m_F = 3/2\rangle$, as shown in Fig. 4.2a. For ^{87}Sr, we initialize into the excited state with a coherent $\pi-$pulse on the $^1\mathrm{S}_0$ to $^3\mathrm{P}_0$ transition. In ^{88}Sr, this transition is completely forbidden in the absence of a magnetic field, and the dipole moment remains too weak to drive at the magnetic fields we currently achieve in our apparatus. We instead drive the $^1\mathrm{S}_0 - ^3\mathrm{P}_1$, $^3\mathrm{P}_1 - ^3\mathrm{S}_1$, and $^3\mathrm{P}_2 - ^3\mathrm{S}_1$ transitions simultaneously in order to optically pump the atoms into the excited state. After initialization into the excited state we use a strong 461 nm pulse on the $^1\mathrm{S}_0 - ^1\mathrm{P}_1$ transition to clear any residual ground state atoms out of the trap. To extract the radial temperature of the atoms, we direct a probe beam radially at ground state atoms and measure their Doppler-broadened excitation profile. For ^{87}Sr, we probe using the $^1\mathrm{S}_0 - ^3\mathrm{P}_0$ clock transition, but in ^{88}Sr, we cannot directly use this transition, so we use $^1\mathrm{S}_0 - ^3\mathrm{P}_1$. To account for heating during loading of ^{88}Sr, we measure the radial temperature after performing one cycle of loading in and out of $^3\mathrm{P}_0$ as described above.

To measure the decay curves shown in Fig. 4.2b, we hold atoms in the lattice for a variable time T, after which the populations of the ground and excited states are destructively read out in series with fluorescence imaging using a 461 nm probe beam. By performing this experiment across different lattice trap depths between $\sim$(20 and 65) E_{rec}, we observe how the decay rate from the excited to ground state is affected by Raman scattering induced by the 813 nm trapping light. Simultaneous loading of two ensembles with a factor of 3 difference in atom number is used to check for consistency between different initial densities during the same experiment.

We also perform a modified experiment that is meant to reduce the effects of run-to-run differences in initial atom number and to confirm the consistency of the extracted rates. We initialize atoms into the excited state, but then repeatedly image the atoms that have decayed or scattered into the ground state during the lattice hold time while leaving the excited state undisturbed. This imaging is repeated with a constant interval, t_{rep}, between 3 and 5 seconds depending on trap depth. We thereby measure almost all atoms that decay to the ground state, as these atoms are quickly counted before they have a chance to escape the lattice. This imaging protocol leaves population of the excited state intact, such that we construct the entire ground state population curve with a single initialization of excited state atoms. In order to determine the initial population of the excited state ($t = 0$), we reduce the duration of the initialization pulse such that a specifically calibrated ratio of atoms are prepared in the excited state, with the rest remaining in the ground state. By then immediately imaging the leftover ground state atoms, we estimate the number of atoms in the excited state. We then only directly read out the population of the excited state at the end of the sequence. We refer to this second experimental method as the "multi-readout" technique to differentiate from the previously described "standard" or "single-imaging" technique. Since this method captures multiple snapshots of the ground state population throughout a single experiment, we construct a ground state population curve (see Fig. 4.2c) with only a single experimental run, which both speeds up data taking and reduces the effect of run-to-run variance in initial atom number.

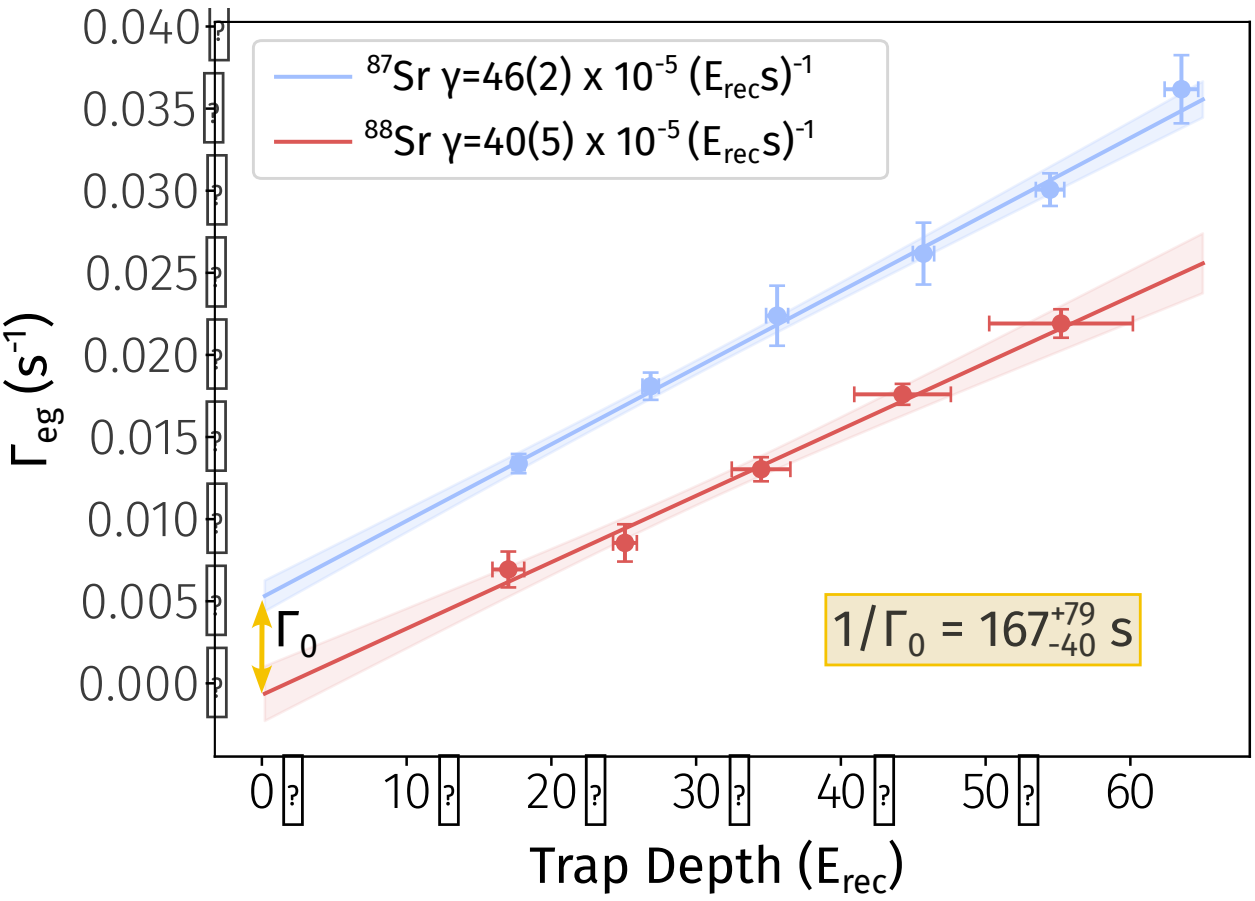


Figure 4.3: Decay rate Γ_{eg} from the excited $^3P_0$ state to the ground $^1S_0$ state in ^{87}Sr (blue) and ^{88}Sr (red) as a function of lattice trap depth. The data are fit to Eq. (4.2) to extract the Raman scattering rate from the excited to ground state. The natural lifetime ($1/\Gamma_0$) of ^{87}Sr is given by the inverse of the difference between the decay rates of the two isotopes extrapolated to 0 E_{rec}. The error bars on the lifetime are obtained by fitting resampled data to obtain a distribution of model parameters. The x-axis is an effective depth, where the radial profile of the trapping light is factored into the total intensity the atoms experience. The x-axis errors in this measurement arise mostly from the uncertainty in the determination of the radial temperature of the atomic ensembles.

4.3 Decay modeling and analysis

To account for the various sources of decay and loss in the optical lattice, we use the model diagrammatically represented in Fig. 4.1. We consider the following rate equations:

$$\begin{aligned} \dot{N}_e &= -(\Gamma_e + \Gamma_{eg})N_e - \gamma_{ee}N_e^2, \\ \dot{N}_g &= -\Gamma_g N_g + \Gamma_{eg}N_e, \end{aligned} \tag{4.1}$$

where the N_g is the ground state population, N_e is the excited clock state population, Γ_{eg} is the rate of decay from the excited to ground state, Γ_g is the background loss rate from the ground state, Γ_e is the background loss rate from the excited state, $\gamma_{ee}N_e = K_{ee}/V$ is the density dependent two-body loss rate, where K_{ee} is the e-e collision rate and V is the effective trapping volume (see Section 4.3.2), and the dot signifies a derivative with respect to time. The decay rate can further be expanded as:

$$\Gamma_{eg} = (\Gamma_0 + \gamma U), \tag{4.2}$$

where Γ_0 is the radiative decay rate, γ is the Raman scattering rate per unit trap depth and U is the effective optical trap depth, calculated by using the measured axial trap depth, U_{axial}, and radial atomic temperature, T_r, through [137]

$$U = U_{\text{axial}}(1 + k_B T_r/U_{\text{axial}})^{-1}. \tag{4.3}$$

We fit our model to standard readout data, averaged over 10 sets of population measurements (Fig. 4.2b) for both Sr isotopes Eq. (4.1). While using the multi-readout data (Fig. 4.2c) to infer model parameters is challenging due to the lack of N_e data, we instead use it to verify the consistency of the model and rates extracted from the other measurements. To numerically solve the equations for the multi-readout technique, N_g is set to zero after every readout while N_e remains unchanged (here, we use the data corresponding to the higher density ensemble; we discuss the low-density data in Section 4.4). Additional fit parameters are discussed in the one- and two-body loss subsections. The uncertainty in the fit parameters is estimated by resampling the data according to the distribution of population measurements.

We then plot the extracted values of Γ_{eg} as a function of depth and a linear fit allows us to extract the Raman scattering rate for ^{3}P$_0$ to ^{3}P$_1$ as well as the decay rate extrapolated to a depth of 0 E_{rec}. This should correspond to Γ_0, along with additional contributions from black-body scattering that is common to both ^{87}Sr and ^{88}Sr . As radiative decay is expected to be absent in ^{88}Sr, we subtract the inferred value of Γ_{eg} for ^{88}Sr from that of ^{87}Sr in order to obtain Γ_0 for ^{87}Sr. These results are plotted in Fig. 4.3. By simulating experimental data based on the model we use to fit to observed data, we verify that the systematic uncertainty due to covariance in fit parameters is negligible compared to the statistical uncertainty, which is dominated by the run-to-run variation in the number of initially loaded atoms. The other major systematic contribution to the uncertainty in the linear fits in Fig. 4.3 arises from the effective trap depth uncertainty, which is ultimately limited by our measurements of the atomic temperature.

We measure Raman scattering rates γ, of $46(2) \times 10^{-5}$ $(E_{\text{rec}}\text{s})^{-1}$ and $40(5) \times 10^{-5}$ $(E_{\text{rec}}\text{s})^{-1}$ for ^{87}Sr and ^{88}Sr respectively, which are in agreement with each other and with previously reported values of $\sim(42 - 55) \times 10^{-5}$ $(E_{\text{rec}}\text{s})^{-1}$ [133, 138]. For ^{88}Sr at 0 E_{rec}, we find Γ_{eg} to be $-0.8(17) \times 10^{-3}$ s^{-1}, which is roughly 2σ from the theoretically predicted black-body-induced scattering rate at 300 K of $2.47(14) \times 10^{-3}$ s^{-1}(see Section 4.5). This discrepancy may be the result of statistical fluctuations, or could arise from an unaccounted for systematic effect. However, as we subtract the intercept of the ^{88}Sr rate from that of ^{87}Sr, any systematic that is common to both will cancel out in our extracted radiative decay rate. The calculated black-body-induced scattering rate also subtracts out and does not contribute. The resulting radiative decay rate we obtain for the excited clock state in ^{87}Sr is $6.0(19) \times 10^{-3}$ s^{-1} corresponding to a lifetime of 167^{+79}_{-40} s. Note that our measurement and analysis method results in a radiative decay rate with symmetric uncertainties. Inverting the measured decay rate then results in asymmetric uncertainties in the extracted radiative lifetime. We compare this value with previous measurements in Fig. 4.7. The contributions of atom number and temperature uncertainties to the uncertainty in the extracted radiative decay rate are listed in Table 4.2.

The larger uncertainty in the measured ^{88}Sr radial temperature arises primarily due to the fact that the relatively broad $^1\text{S}_0 - ^3\text{P}_1$ transition is used for this measurement.

4.3.1 One-body loss

The one-body loss from the ground state, Γ_g is measured independently by loading atoms in the ground state and measuring the population decay. The extracted values and their uncertainties, shown in Fig. 4.4, are used to constrain fit parameters in the standard readout data analysis. The excited state loss is extracted from fitting the rate equations (Eq. (4.1)) to the standard readout data.

4.3.2 Two-body loss

In Eq. (4.1), the two-body loss term, γ_{ee}, can be written as K_{ee}/V where V is the effective volume of the ensemble. To calculate V, we must first sum the rate equation over every individual lattice site -

$$\sum_i \dot{N}_{e,i} = -(\Gamma_e + \Gamma_{eg}) \sum_i N_{e,i} - \sum_i \frac{K_{ee}}{V_{\text{site}}} N_{e,i}^2, \tag{4.4}$$

where the volume of an individual lattice site, V_{site}, is assumed to be constant. Additionally assuming that the atoms are approximately distributed normally and the width of the distribution across sites, σ, does not change significantly with time, we can re-write the above equation as

$$\dot{N}_e = -(\Gamma_e + \Gamma_{eg}) N_e - K_{ee} \frac{N_e^2}{2\sqrt{\pi}\sigma V_{\text{site}}}. \tag{4.5}$$

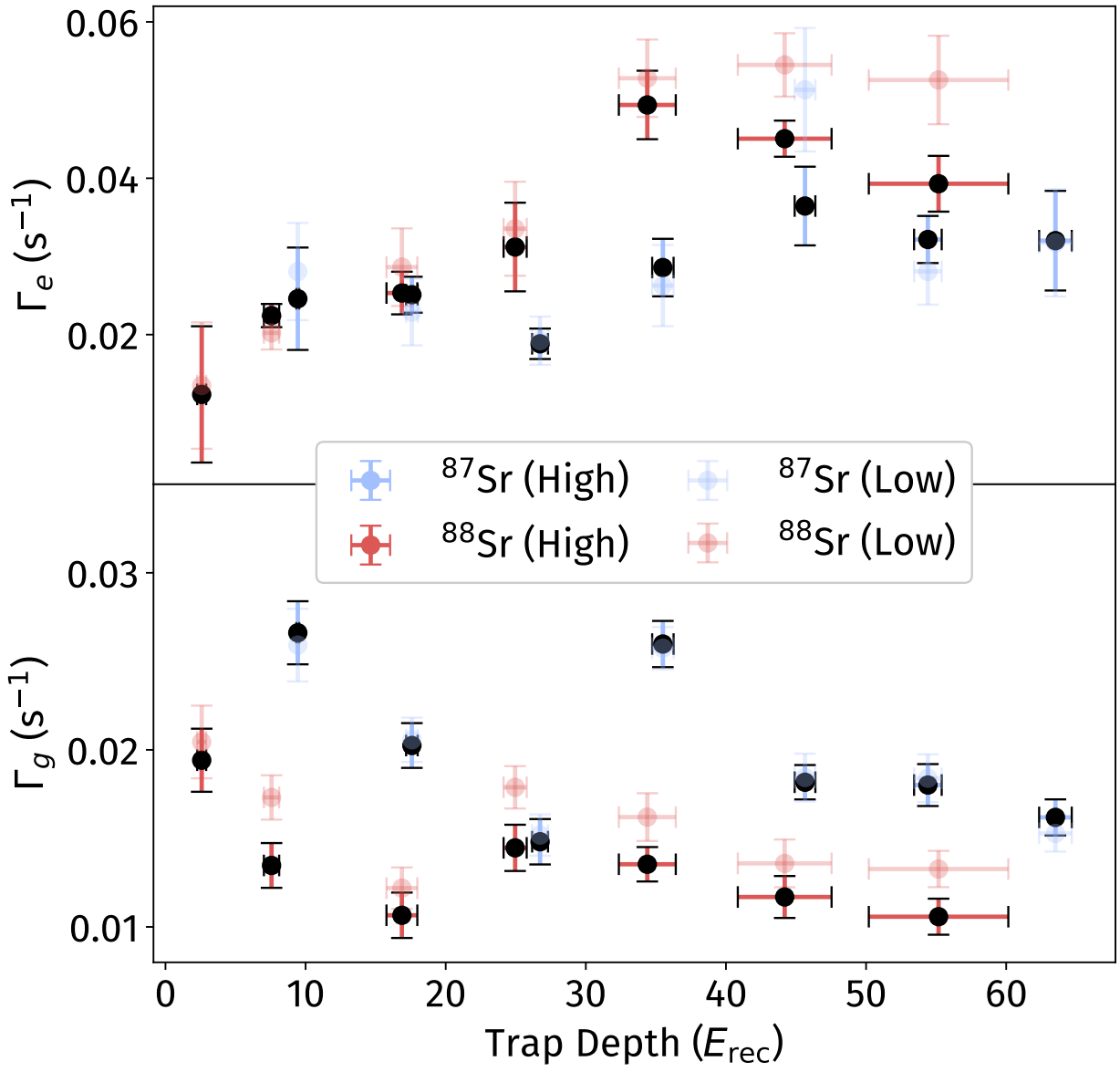


Figure 4.4: One-body loss rates for ground Γ_g and excited Γ_e states for high and low density ensembles of ^{87}Sr and ^{88}Sr. Γ_g is measured independently while Γ_e is inferred by fitting standard readout data to the decay model (Eq. (4.1)).

Rate	This work	Other Expt.	Theory
Γ_0 ($\times 10^{-3}$) (s^{-1})	6.0(19)	6.6(2) [135], 8.5(2)[134], 3.0(13)[133]	6.9(19)[46]
γ ^{87}Sr ($\times 10^{-5}$) $(E_{rec}s)^{-1}$	46(2)	55.6(1.5)[133]	49.8[133]
γ ^{88}Sr ($\times 10^{-5}$) $(E_{rec}s)^{-1}$	40(5)		
K_{ee} ^{87}Sr ($\times 10^{-6}$) ($cm^3s^{-1}K^{-1}$)	$11(1) \times T_r$	$4(2) \times T_r$[139]	
K_{ee} ^{88}Sr ($\times 10^{-13}$) (cm^3s^{-1})	262(6)	180(30)[140]	

Table 4.1: Summary of experimentally measured rates and comparison with existing theory.

Using the fitted values of γ_{ee} and experimentally measured values of σ and V_{site}, we extract K_{ee} by comparing the above expression to Eq. (4.1), which gives us an effective volume $V = 2\sqrt{\pi}\sigma V_{\text{site}}$. We show these values for the high-density ensemble in Fig. 4.5. For ^{87}Sr, we obtain an atomic-temperature-dependent two-body loss rate $K_{ee} = 11(1) \times T_r \times 10^{-6}$ $cm^3s^{-1}K^{-1}$. We note that this value is larger than the previously reported value of $4(2) \times T_r \times 10^{-6}$ $cm^3s^{-1}K^{-1}$[139]. For ^{88}Sr, we obtain $K_{ee} = 262(6) \times 10^{-13}$ cm^3s^{-1}, which is close, but not entirely consistent with the previously reported value of $180(30) \times 10^{-13}$ cm^3s^{-1}[140]. A possible reason for the inconsistencies might be that the relatively minor contribution of two-body loss cannot be efficiently decoupled from other losses by the curve fitting routines, due to the high covariance between the various fit parameters. Additionally, the assumptions in Eq. (4.5) cease to be valid when individual sites have low atom numbers. Future experiments could leverage greater control of experimental parameters, ideally enabling a triple-zero extrapolation in atom number, trap depth and radial temperature. This would help isolate the effects of various loss channels with low uncertainty.

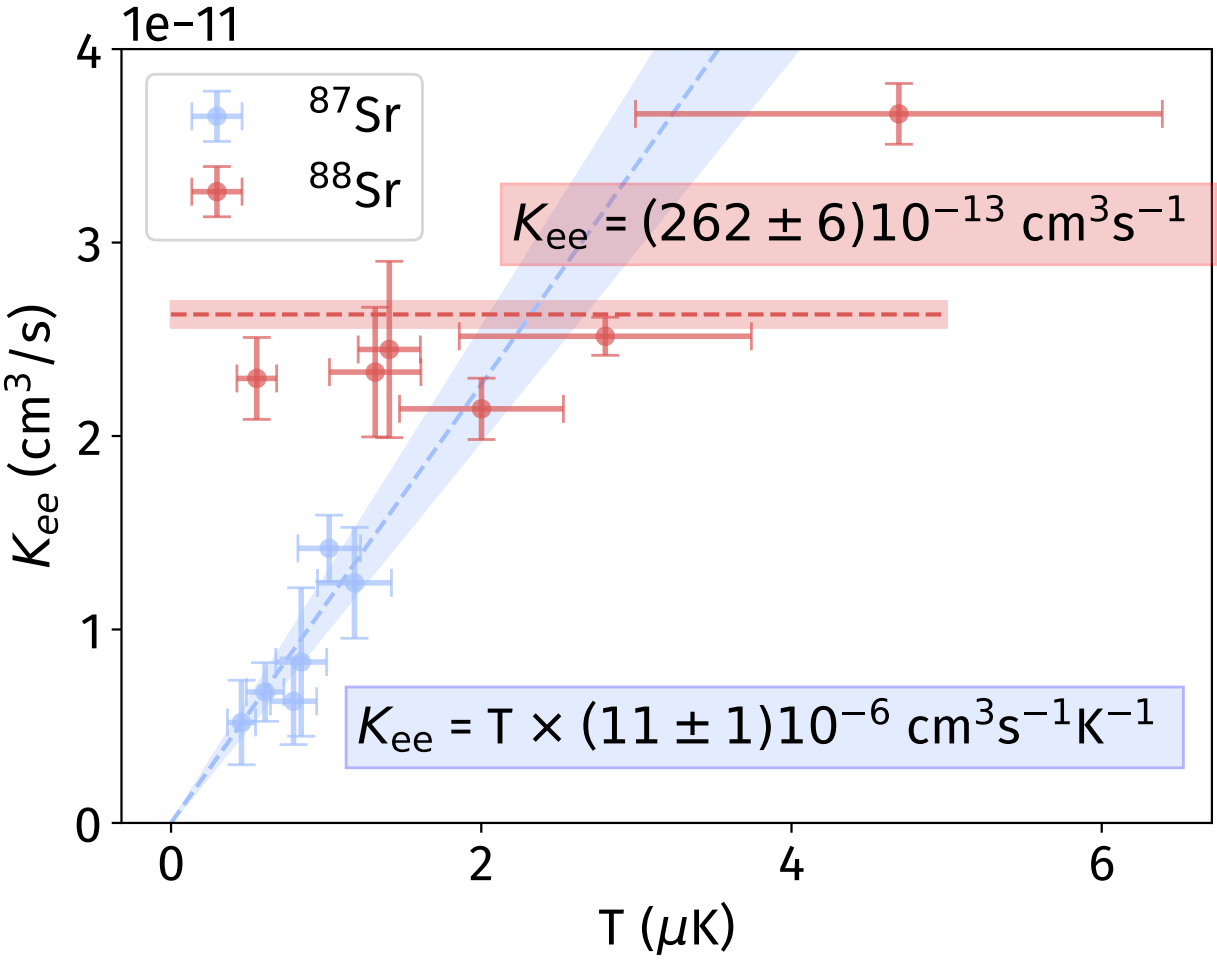


Figure 4.5: Inferred values of two-body loss K_{ee} for high-density ensembles of ^{87}Sr and ^{88}Sr.

4.4 Low-density data

In Fig. 4.6, we observe that while the data from high and low density ensembles of ^{87}Sr are largely consistent with each other, there is a significant difference between the fit parameters for the two ensembles in ^{88}Sr. A possible reason for this discrepancy might lie in the calculation of the effective trap depths which depends on the radial temperature of the ensembles. While our analysis assumes that this temperature is the same across both densities, Fig. 4.4 seems to suggest a systematic shift in the ground state loss between high and low densities which could be a result of higher temperatures for the low-density ensembles. This, in turn, would give us a smaller effective trap depth for the low-density data in ^{88}Sr, thereby suggesting a larger increase in Raman scattering rate with trap depth. While a thorough analysis of this effect is more suitable for future work, we do observe that if we let the estimated radial

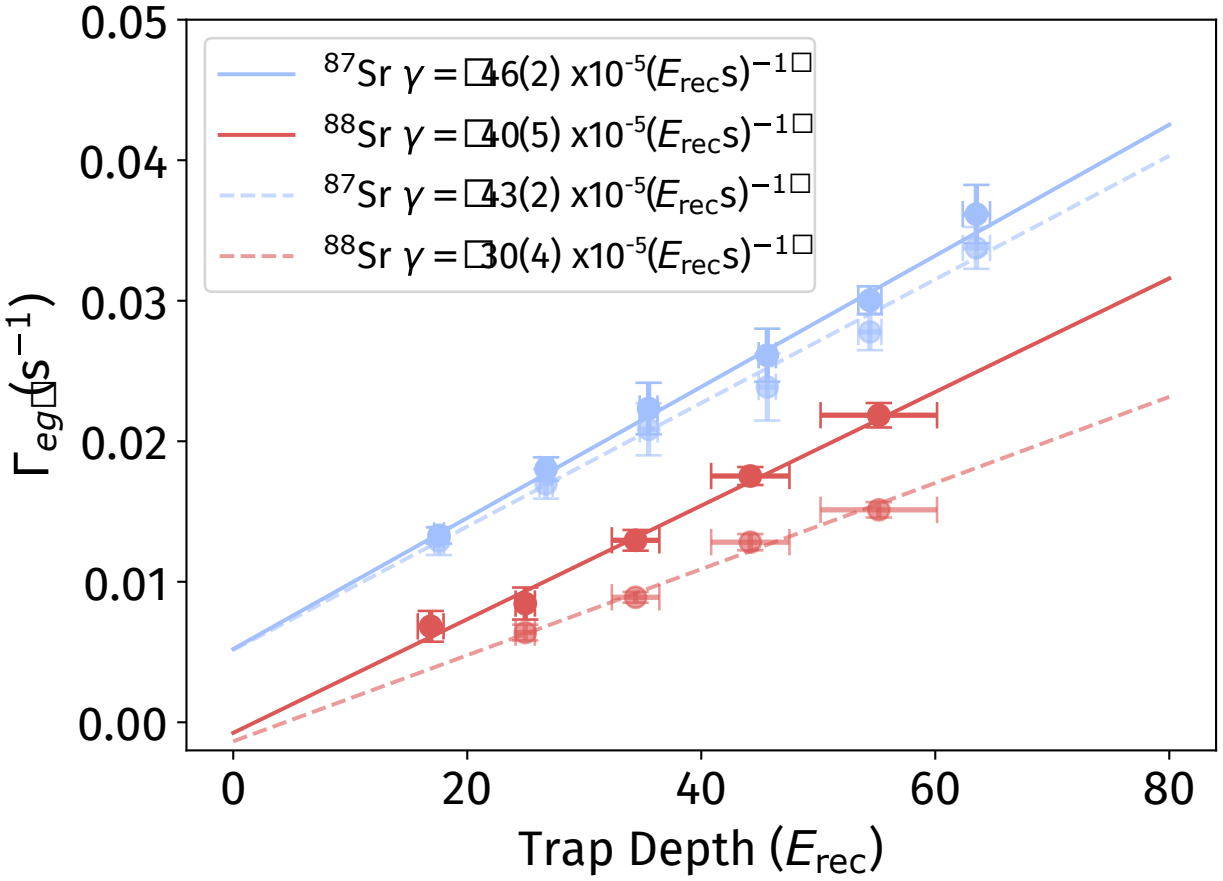


Figure 4.6: Comparison of extracted decay rates between high (solid) and low (dashed) density ensembles of ^{87}Sr and ^{88}Sr as a function of trap depth.

temperature of the low-density data to be increased by a factor in the decay model, the decay rates of the two ensembles are more consistent with each other.

4.5 Black-body scattering rate

Black-body radiation (BBR) can scatter atoms out of the $^3P_0$ state primarily through two channels, the E1 transition, $^3P_0 \rightarrow {}^3D_1$, and the M1 transition, $^3P_0 \rightarrow {}^3P_1$. The BBR scattering rate for each channel can be calculated through the following Gaussian electromagnetic expressions

$$R_{E1} = \frac{2\pi}{3\hbar^2}\rho(\nu_{E1}, T_{BBR})Z_{E1}^2, \tag{4.6}$$

$$R_{M1} = \frac{2\pi}{3\hbar^2}\rho(\nu_{M1}, T_{BBR})Z_{M1}^2, \tag{4.7}$$

where ν_{E1} is the $^3\mathrm{P}_0 \rightarrow {}^3\mathrm{D}_1$ transition frequency, ν_{M1} is the $^3\mathrm{P}_0 \rightarrow {}^3\mathrm{P}_1$ transition frequency, Z_{E1} is the reduced matrix element $\langle {}^3P_0||\mathbf{D}||{}^3D_1\rangle$, Z_{M1} is the reduced matrix element $\langle {}^3P_0||\boldsymbol{\mu}||{}^3P_1\rangle$, and $\rho(\nu, T_{BBR})$ is the BBR spectral energy density at frequency ν and temperature T_{BBR}, given by

$$\rho(\nu, T_{BBR}) = \frac{8\pi h\nu^3}{c^3}\frac{1}{e^{h\nu/k_BT} - 1}. \tag{4.8}$$

While the reduced matrix element for the electric dipole transition is a factor of $\approx 1/\alpha$ larger than that of the magnetic dipole transition, the BBR spectral energy density at 300 K is much greater at ν_{M1} than ν_{E1}.

Considering both of these channels when calculating the BBR-induced scattering rate out of $^3\mathrm{P}_0$, we arrive at a value of $2.47(14) \times 10^{-3}$ s^{-1}. This value differs from the value reported in Dörscher et al. [133], as they did not consider the extra contribution from the M1 channel, which amounts to a $\approx 1.7\ \sigma$ correction from their reported value of $2.23(14)\times 10^{-3}$ s^{-1}.

4.6 Lifetime measurement conclusions and outlook

We find the lifetime to be 167^{+79}_{-40} s. This value is largely consistent with previous measurements by Lu et al. [135], Dörscher et al. [133], and Muniz et al. [134]. It also lies within the theory uncertainty given by Boyd et al. [46].

By varying the lattice depth, ensemble density, and measuring with two different isotopes, we disentangled the radiative decay rate from the other decay processes occurring in a 1-D optical lattice trap. At lower trap depths, ultra-high vacuum and long atom lifetimes in the optical lattice allowed us to attribute a significant fraction ($\sim 50\%$) of the measured ground state population from the excited state to radiative decay.

The primary limitations in our measurement were the statistical uncertainty due to variation in the initial number of loaded atoms between experimental runs and uncertainty in the radial temperature of ^{88}Sr, both of which could be mitigated through technical

Table 4.2: Contribution of statistical and systematic uncertainties to the total uncertainty in extracted radiative decay rates.

Source	**Uncertainty** ($\times 10^{-3}$**s**$^{-1}$)
^{87}**Sr**	0.9
Atom number	0.9
Atom temperature	0.3
^{88}**Sr**	1.7
Atom number	1.3
Atom temperature	0.8
Total	1.9

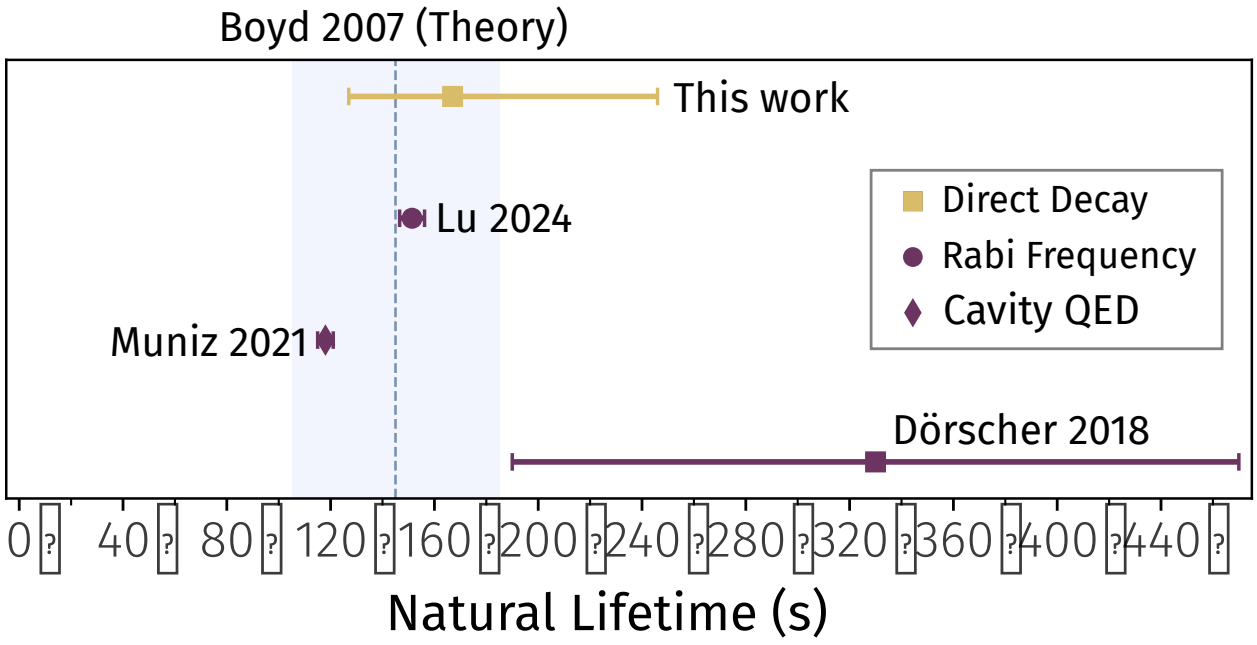


Figure 4.7: Comparison of measured ^{87}Sr lifetime values from Refs. Lu 2024 [135], Muniz 2021[134], Dörscher 2018 [133]. Dörscher and we both measure the $^3P_0$ lifetime through observations of radiative decay. Lu and Muniz both measured the dipole moment of the clock transition, leading to their lifetime values. Muniz used a cavity QED comparison between $^1S_0$ to $^3P_0$ and $^1S_0$ to $^3P_1$ dipole moments, and Lu measured the Rabi frequency of the transition in conjunction with characterization of the laser intensity. The dashed line and shaded region indicate theoretical lifetime value and uncertainty, respectively, calculated in Boyd et al [46]. Boyd applied Breit-Wills theory [141] to calculate the lifetime from measured hyperfine splitting values. The theory uncertainty arises from the choice of theoretical framework and confidence associated with lifetimes of the $^1P_1$ and $^3P_1$ states.

improvements to the experiment in future work. To mitigate the systematic uncertainty arising from uncertainty in additional fit parameters, adding a resonant laser that rapidly repumps out of the $^3P_1$ state would suppress decay events from $^3P_0$ to $^1S_0$ through the $^3P_1$ state due to Raman and black-body scattering. Finally, varying the effective trapping volume could help in isolating the two-body loss rates from the rest of the measurement.

The lifetime of the $^3P_0$ state sets an ultimate limit on the coherence of the narrow-line clock transition of ^{87}Sr. Our measurement of this value helps to determine the achievable performance of comparisons between ^{87}Sr clocks in applications where differential measurement techniques bypass the limits imposed by the local oscillator [59, 103]. The experimental techniques described in this chapter could also be used to make direct lifetime measurements of other similarly long-lived atomic transitions in atoms and ions.

Chapter 5

Erasure conversion in an optical lattice clock

This chapter was previously published as Shuo Ma, Jonathan Dolde, Xin Zheng, Dhruva Ganapathy, Alexander Shtov, Jenny Chen, Anke Stöltzel, Bennett J. Christensen, and Shimon Kolkowitz. "Enhancing Optical Lattice Clock Coherence Times with Erasure Conversion". In: PRX Quantum *6.4 (Nov. 2025), p. 040340.* DOI: 10.1103/2rqf-r9gw.

Section 5.2 of this chapter is adapted from Pradeep Niroula, Jack Dolde, Xin Zheng, Jacob Bringewatt, Adam Ehrenberg, Kevin C. Cox, Jeff Thompson, Michael J. Gullans, Shimon Kolkowitz, and Alexey V. Gorshkov. "Quantum Sensing with Erasure Qubits". In: Phys. Rev. Lett. *133 (8 Aug. 2024), p. 080801.* DOI: 10.1103/PhysRevLett.133.080801.

5.1 Introduction

State-of-the-art optical lattice clock comparisons have reached measurement precision at the 10^{-20} level [59, 103] and absolute clock accuracy at or below the 10^{-18} level [66, 67, 97–99]. This enables a range of novel emerging applications, such as relativistic geodesy, searches for ultralight dark matter, and gravitational wave detection [12, 24–27, 30, 69, 84, 101]. Central to these applications are low clock comparison instabilities and interrogation times that fully exploit the long lifetimes of the clock states.

While the performance of an optical lattice clock as an absolute time-keeper or frequency reference is limited by the coherence of the optical local oscillator [69, 100], synchronous differential comparisons between clocks sharing the same laser light can achieve coherence times exceeding the atom-laser coherence and can extend the coherent clock interrogation time by orders of magnitude. Recent demonstrations with neutral Sr atoms include differential comparisons between spatially separated atom ensembles in a one-dimensional (1D) optical lattice [59], and subregions of an extended atom ensemble in a cavity-enhanced 1D optical

lattice clock [103]. However, the demonstrated atomic coherence times have not yet reached the expected excited clock state lifetime in ^{87}Sr, which is believed to be on the order of $120 - 160$ s [123, 134, 135, 138], with one measurement even reporting a lifetime of 330(140)s [133], with Raman scattering induced by trapping light as the primary limiting factor [59, 123, 133, 138].

Standard measurement protocols employed in optical lattice clocks do not distinguish between coherent atoms and those affected by errors such as Raman scattering. In this chapter we show that the decoherence caused by Raman scattering and radiative decay in optical lattice clocks can be partially mitigated by identifying and removing atoms that have scattered photons or radiatively decayed, significantly extending the achievable coherent interrogation times. This concept is inspired by erasure conversion in quantum error detection [58, 143–145], and a related strategy was recently theoretically proposed to mitigate errors and enhance the performance of optical clocks and quantum sensors [136].

5.2 Comparing erasure and dephasing error limits on differential fractional frequency instability

In Ref. [136], we characterize two different error channels in our multiplexed optical lattice clock system. The two error channels that we examine are dephasing errors, which manifest as σ_z acting with some error rate q, and erasure errors, which manifest as an operator taking you out of the clock subspace into a loss channel at rate q. Deriving the quantum Cramér-Rao bounds based on the Fisher information scaling of each error channel puts bounds on the fractional instability our clock comparisons. The fractional instability from a clock comparison using Ramsey interrogation is given as

$$\sigma = \frac{1}{2\pi T_R}\frac{\delta\phi}{f_0} \tag{5.1}$$

where T_R is our Ramsey free evolution time, and $\delta\phi$ is the differential phase uncertainty of our Ramsey measurement, which is limited by the Cramér-Rao bound, given in terms of the Fisher information, $\mathcal{F}$, as

$$\delta\phi \geq \frac{1}{\mathcal{F}^{1/2}} \tag{5.2}$$

For dephasing errors, $\mathcal{F}$ scales as (1-q)^2 with the error rate q scaling as $\propto e^{-\Gamma T_R}$. The fractional instability under the effect of depolarization errors at rate q is therefore bounded by

$$\sigma_{dephasing} \geq \frac{\sigma}{(1-q)} \tag{5.3}$$

where σ for N uncorrelated atoms with cycle time $T_c \equiv T_R + T_{\text{dead}}$ and total averaging time τ is given as

$$\sigma = \frac{1}{2\pi}\frac{1}{f_0}\sqrt{\frac{1}{N}\frac{1}{T_c\tau}} \tag{5.4}$$

For erasure errors, the Fisher information scales as (1-q), giving a fractional instability bound of

$$\sigma_{erasure} = \frac{\sigma}{\sqrt{1-q}} \tag{5.5}$$

A full quantitative derivation of the above instability bounds can be found in the supplement of Ref. [136].

In order to demonstrate the different instability limits from the two error channels, we vary the error rates for each channel independently and compared the extracted differential instability at the same error probability q, see Fig. 5.1. To vary the erasure error, we vary the duration of the initial clock pulse we use to transfer our atom population from $|g, m_F = 9/2\rangle$ to $|e, m_F = 7/2\rangle$. This varying pulse duration, along with a 461 nm pulse to remove all ground state atoms from our lattice, allows us to vary the final number of atoms, N, read out in our system without affecting the dephasing error rate. Our erasure probability is then $q = 1 - N/N_0$ where N_0 is our nominal operating atom number. To vary the dephasing error, we detune the optical lattice wavelength away from the operational magic wavelength, which induces a loss of contrast, C, in our ensembles' Ramsey fringes. The dephasing probability is $q = 1 - C$. As shown in Fig. 5.1(f), the differential instability is lower for the erasure error measurement than the dephasing error measurement for the same error probability q. We see that the scaling of each error channel obeys the Cramér-Rao bound scaling by plotting the theoretical quantum projection noise limit scaled by the respective error probabilities with no free parameters.

Given the favorable scaling of differential fractional frequency instability subject to erasure errors when compared to dephasing errors, we should expect an improvement in the differential fractional instability if we can manage to convert dephasing or depolarizing errors into erasure errors. In the rest of this chapter, we realize erasure conversion for ^{87}Sr atoms in a multi-ensemble optical lattice clock by directly probing the coherent clock population using a hyperfine-state-resolved readout method, discriminating between the atoms that remain in the clock subspace and those that have scattered into other hyperfine states. This method introduces minimal experimental overhead, requiring only three additional π-pulses on the narrow-linewidth clock transition. As these pulses are applied after clock interrogation and only change the method of state readout, we do not expect this technique will introduce additional differential systematic frequency shifts.

Using hyperfine-resolved erasure conversion we roughly double the achievable atomic coherence times in our system, observing atomic coherence times exceeding 100 s with synchronous Ramsey spectroscopy and over 150 s with a synchronous spin echo sequence. We

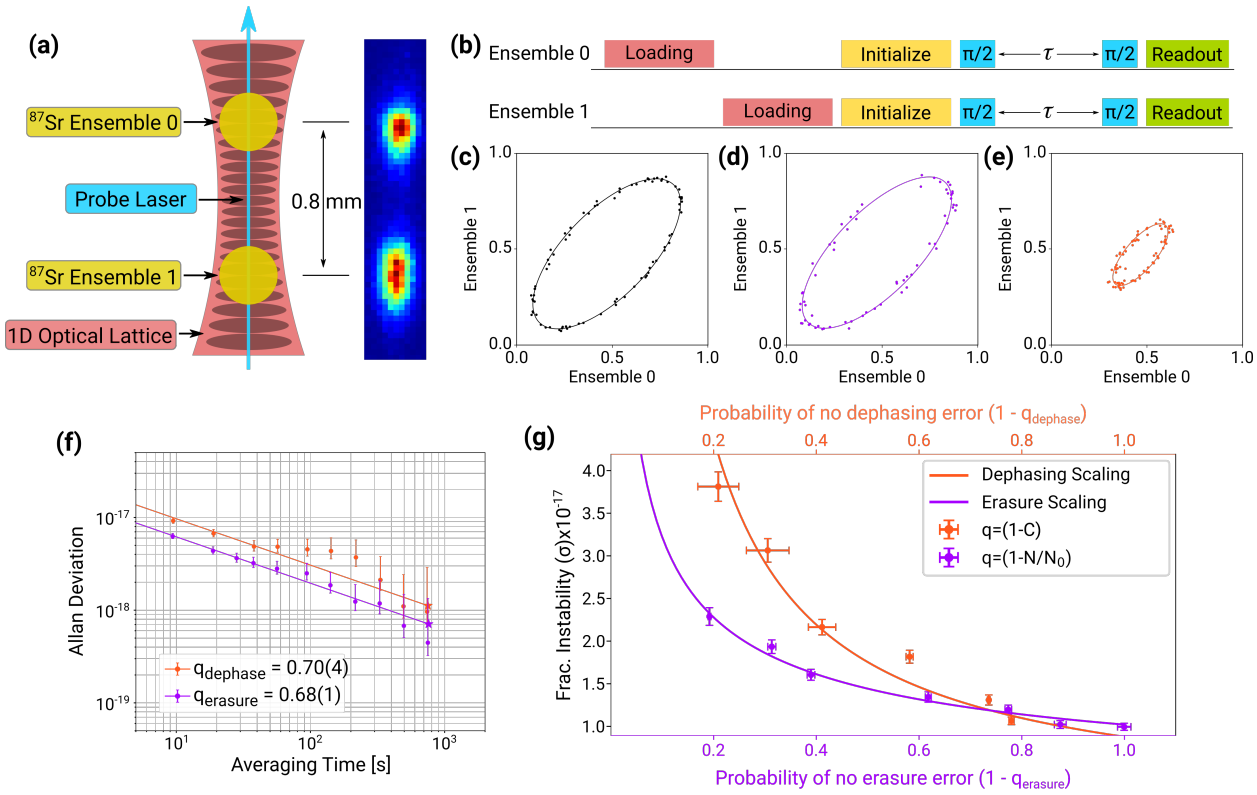


Figure 5.1: (a) Diagram of two ensembles of ^{87}Sr loaded into the same 1-D optical lattice trap. The ensembles, separated vertically by 1 cm, can be interrogated simultaneously with a laser directed along the axis of the trap. A camera image of the ensembles is shown on the right. (b) Experimental sequence (timing not to scale) used for differential comparisons of the ensembles. The atoms, initialized in the ground state, are synchronously probed with a Ramsey interrogation technique. We choose a Ramsey dark time, τ, of 8.0 seconds and a sequence time of 9.67 seconds. (c) The excitation fraction of each ensemble is plotted parametrically, tracing out an ellipse corresponding to the differential phase between the ensembles. This ellipse corresponds to an atom number N of 1915(24) atoms and a contrast C of 0.78(1). This gives a value of $q_{erasure} = 0.00(2)$ and $q_{dephase} = 0.22(1)$ (d) The atom number is decreased relative to the ellipse in (c) while keeping the contrast constant. This ellipse corresponds to an increase in erasure error. This ellipse has an atom number N of 551(14) atoms and a contrast C of 0.82(2), giving $q_{erasure} = 0.68(1)$ and $q_{dephase} = 0.18(2)$ (e) The contrast is decreased relative to the ellipse in (c), while keeping atom number approximately the same. This ellipse corresponds to an increase in dephasing error. This ellipse has an atom number N of 2112(28) atoms and a contrast C of 0.30(4), giving $q_{erasure} = 0.00(2)$ and $q_{dephase} = 0.70(4)$ (f) Extracted stabilities from ellipses shown in (d) and (e) The stability for the orange dephasing curve is 3.1(1)e-17/$\sqrt{\tau}$, and the stability for the purple erasure curve is 1.93(8)e-17/$\sqrt{\tau}$. Even with similar error rates, the erasure error leads to lower instability than dephasing error.

Figure 5.1 (continued): (g) Measured fractional instability against error rate q for erasure error and dephasing error. For the dephasing noise, the error rate q is derived from the differential Ramsey fringe contrast as $q = 1 - C$. For atom loss, the error rate is taken to be $q = 1 - N/N_0$, where $N_0(N)$ is the average number of atoms in both ensembles before (after) interrogation. The solid lines correspond to the quantum-projection-noise-limited stability at zero error rate (Eqs. (5.5) and (5.3) with no free parameters). Note that zero-erasure curve is offset to account for the maximum achievable contrast of ≈ 0.8. The reduced chi-squared value for the data compared to the theory curves is 2.14.

introduce a theoretical framework and perform numerical simulations incorporating known decoherence sources, including Raman scattering, lattice-induced AC Stark shifts, and density shifts, to explain the origin of this coherence enhancement. While we do not yet realize a meaningful enhancement in the measured stability of the clock comparison compared to standard readout, we find that erasure conversion flattens out the scaling of clock instability with interrogation time, offering advantages in applications requiring flexible interrogation times, such as gravitational wave detection[26]. Additionally, extending coherence times with erasure conversion could also enable new applications, such as spectroscopy of splittings below the frequency resolution limit set by the natural linewidth[146, 147].

5.3 Impact of Raman Scattering and Radiative decay on Atomic Coherence

We prepare our atoms the same way as detailed in Chapter 2; except for one modification, see Fig. 5.2(a). Rather than loading multiple spatial ensembles by detuning the retro-reflected lattice light using dual AOMs, we prepared multiple ensembles by shifting the location of the MOT field zero roughly midway through the single-frequency stage of the narrow linewidth MOT [148], so that the atoms are cooled into the lattice in two different regions spatially separated from each other by roughly 1 mm.

During the synchronous Ramsey comparisons, atoms in both ensembles are prepared in a superposition of $|g, 5/2\rangle$ and $|e, 3/2\rangle$, as shown in Fig. 5.2(b), the least magnetically sensitive clock transition for ^{87}Sr, which we define as the clock subspace. Because a clock interrogation sequence ends with a projective measurement of the remaining populations in $|g, 5/2\rangle$ and $|e, 3/2\rangle$, atoms lost during interrogation do not contribute signal or noise to the final measurement outcome. However, Raman scattering from the lattice trapping light redistributes population from $^3\mathrm{P}_0$ into $^3\mathrm{P}_1$ and $^3\mathrm{P}_2$, with calculated branching ratios of 0.39 and 0.22, respectively. Meanwhile, the remaining 0.39 of the population undergoes Rayleigh scattering, transferring back into $^3\mathrm{P}_0$ without flipping the nuclear spin state, due to the large detuning relative to the hyperfine splitting in the excited state and the use of linearly polarized lattice light (see Section A.3 for details). In particular, Raman scattering from $^3\mathrm{P}_0$ to $^3\mathrm{P}_1$,

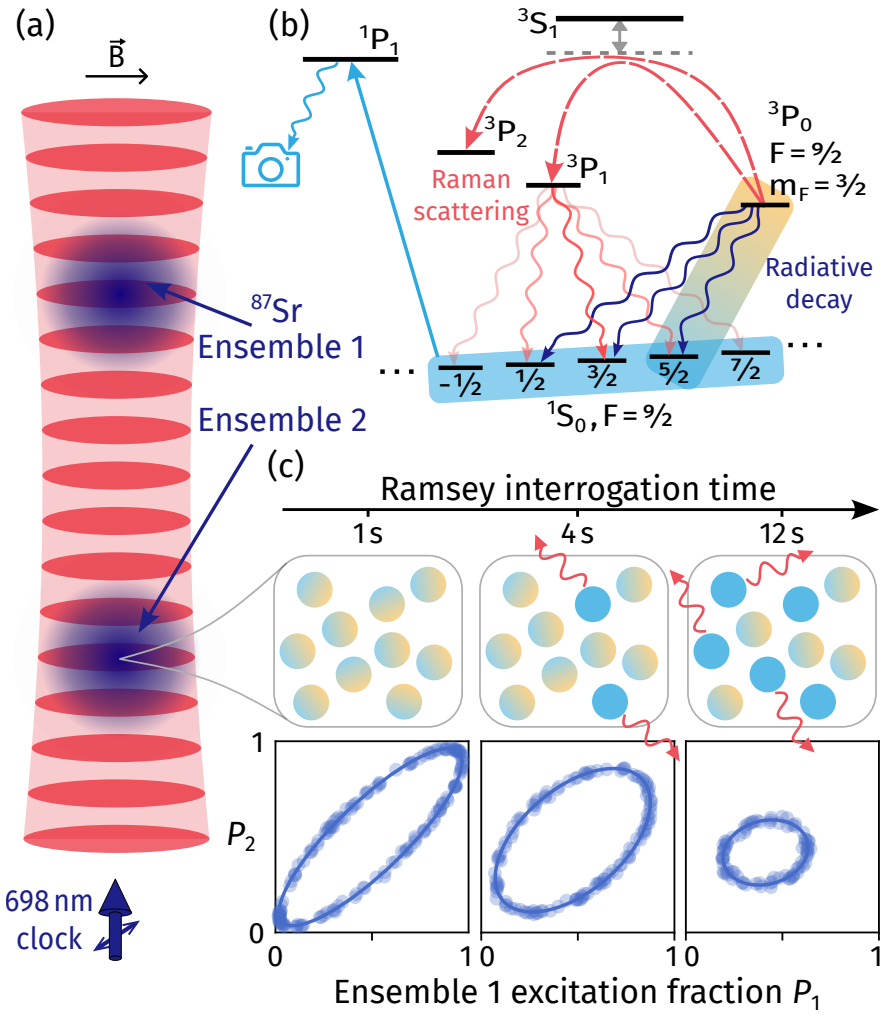


Figure 5.2: Lattice photon-induced Raman scattering and its effect on hyperfine state populations. (a) Two ensembles of ^{87}Sr atoms, initially prepared in the clock subspace, are simultaneously probed by the 698 nm clock laser under a magnetic bias field. (b) The relevant energy level diagram for a ^{87}Sr optical lattice clock. Atoms are initialized in the clock subspace, consisting of $|^1\mathrm{S}_0, m_F = 5/2\rangle$ (blue) and $|^3\mathrm{P}_0, m_F = 3/2\rangle$ (yellow). Raman scattering from the lattice light redistributes the population from $|^3\mathrm{P}_0, m_F = 3/2\rangle$ to the $^3\mathrm{P}_J$ manifolds, while radiative decay directly returns excited-state atoms to $^1\mathrm{S}_0$. Radiative decay from $^3\mathrm{P}_1$ further redistributes the population among the $^1\mathrm{S}_0$ m_F states. Detection is performed via fluorescence imaging on the $^1\mathrm{S}_0$-$^1\mathrm{P}_1$ transition. (c) The excitation fractions of ensembles 1 and 2 from synchronous Ramsey measurement are plotted parametrically, resulting in ellipses determined by the relative detuning between the clock transitions of the atoms in the two ensembles. Over time, Raman scattering and radiative decay transfer atoms out of the clock subspace, leading to the shrinking size of the ellipses, which corresponds to decoherence.

followed by subsequent radiative decay, redistributes population into the $^1S_0$ manifold with $\Delta m_F = 0, \pm 1, \pm 2$ according to selection rules, as depicted in Fig. 5.2(b)&(c). We find that most atoms scattered into $^3P_2$ subsequently escape the trap due to high two-body collision rates, effectively being erased. However, a small residual $^3P_2$ population would contribute to the final signal after repumping. Rayleigh scattering within $^3P_0$ and $^1S_0$ does not induce decoherence due to the use of a magic wavelength lattice [149], ensuring equal polarizabilities for the g and e states. On the other hand, radiative decay from the excited state redistributes the population among the m_F states in the $^1S_0$ manifold, with changes of $\Delta m_F = 0, \pm 1$.

Standard readout via the $^1S_0$-$^1P_1$ transition accounts for the remaining ground and excited state populations but excludes atoms lost during interrogation. However, it cannot resolve contributions from different m_F populations, leading to coherence degradation in projective measurements, as shown in Fig. 5.2c. In contrast, hyperfine-resolved readout selectively probes the clock subspace, distinguishing coherent atoms and thereby preserving and extending coherence.

5.4 Measurement of hyperfine state population distribution induced by Raman scattering

In order to determine the erasure conversion efficiency of hyperfine-resolved readout, we experimentally measure the nuclear spin population distribution for spin-polarized atoms prepared in the excited clock state and subject to Raman scattering and radiative decay at a trap depth of 100 E_{rec}. The experimental sequence is shown at the top of Fig. 5.3(b). We first initialize atoms in $|e, 3/2\rangle$ and then apply a clean-up pulse on the $^1S_0 \rightarrow {}^1P_1$ transition to remove residual population in g caused by pulse imperfections. Atoms are held in the lattice at a trap depth of approximately 100 E_{rec} for 10 s. As the radiative decay and Raman scattering rates have different dependencies on trap depth, the erasure fraction varies accordingly. We select this depth to ensure a sufficient number of scatterings and decays returning to the $^1S_0$ state while maintaining a reasonable overall measurement cycle time.

We spin-selectively probe each of the $|g, m_F\rangle$ population using hyperfine-state-dependent clock transitions ($|g, m_F\rangle \leftrightarrow |e, m'_F\rangle$). We calibrate the transition frequency for each hyperfine clock transition and perform Rabi oscillations by selectively driving one clock transition at a time. We average the result for each transition over at least 10 measurements and fit to a sinusoid. We infer the population of the m_F state from the fitted amplitude of the Rabi oscillation. Examples of the measured and fitted Rabi oscillations for the $|g, 5/2\rangle \leftrightarrow |e, 7/2\rangle$ and $|g, -5/2\rangle \leftrightarrow |e, -7/2\rangle$ transitions are shown in the inset of Fig. 5.3(b). A substantial population is observed in $|g, 5/2\rangle$, while little population is detected in $|g, -5/2\rangle$.

Summing the fitted amplitudes for all 10 $^1S_0$ hyperfine state populations, we obtain a total population of 0.449(19). Adding this to the average remaining $^3P_0$ and $^3P_2$ population of 0.541(1) results in a total amplitude of 0.990(20), consistent with unity. For clarity, in Fig. 5.3(b) we present the normalized population distribution of $^1S_0$, obtained after

subtracting the remaining $^3P_0$ and $^3P_2$ populations. We compare this to the theoretically calculated population distribution and find a reasonable agreement between theory and experiment. The calculated Raman and Rayleigh scattering rates are tabulated in Section A.3. We attribute the small but statistically significant deviations between the experiment and the theoretical prediction mainly to scattering contributions from higher excited states and from the omission of hyperfine splitting in the excited states in our calculations.

We measure the population distribution of $^3P_0$ using a sequence nearly identical to that in Fig. 5.3(b), with the addition of a clean-up pulse to remove $^1S_0$ populations before driving the clock pulse, as shown at the top of Fig. 5.3(a). The sum of the ten fitted Rabi oscillation amplitudes is 0.919(19). We suspect that the deviation from unity arises from residual population in the $^3P_2$ state due to scattering. Our measured probability distribution of the e hyperfine states (after normalization) indicates that the majority of the population undergoes $\Delta m_F = 0$ transitions. However, a small fraction appears in other excited m_F states. We suspect this arises from the Raman scattering between different excited m_F states caused by the impurity in the lattice laser's polarization.

A comparison between the experimentally measured and theoretically calculated populations in g (after normalization) is shown in Fig. 5.3(b). We observe that roughly 18% of atoms that are subject to Raman scattering are found in the $|g, 5/2\rangle$ state. This sets a lower bound on the detectable erasures through hyperfine-resolved readout. However, this limitation could in principle be mitigated by using more widely separated hyperfine clock states, such as a superposition between $|g, 9/2\rangle$ and $|e, 3/2\rangle$. This approach would come at the cost of increased magnetic field sensitivity and would require additional clock or microwave pulses for coherent population transfer.

5.5 Hyperfine-state-resolved readout method

In Fig. 5.4, we present a protocol for erasure conversion via hyperfine-resolved readout, which utilizes a sequence of clock π-pulses to coherently transfer and selectively measure population in specific targeted nuclear spin states. The protocol begins by shelving the $|g, 5/2\rangle$ population using a clock π-pulse resonant with the $|g, 5/2\rangle \rightarrow |e, 7/2\rangle$ transition. An imaging pulse then measures the remaining residual ground-state population, $N_{g,\mathrm{res}}$, while also removing them. We then apply a second clock π-pulse on the same transition, followed by another imaging pulse to measure the shelved $|g, 5/2\rangle$ population, $N_{g,5/2}$. Next, a third clock π-pulse, resonant with the $|e, 3/2\rangle \rightarrow |g, 5/2\rangle$ transition, transfers the $|e, 3/2\rangle$ population back to g, where it is measured with a third imaging pulse. A global repump pulse on the $^3P_{0,2} \rightarrow {}^3S_1$ transitions, followed by a fourth imaging pulse, measures the residual excited-state population, $N_{e,\mathrm{res}}$. Finally, a background imaging pulse without atoms records the stray light background, N_{bg}. The entire sequence is completed in under 50 ms.

The excitation fraction in the clock subspace probed by hyperfine-resolved readout is

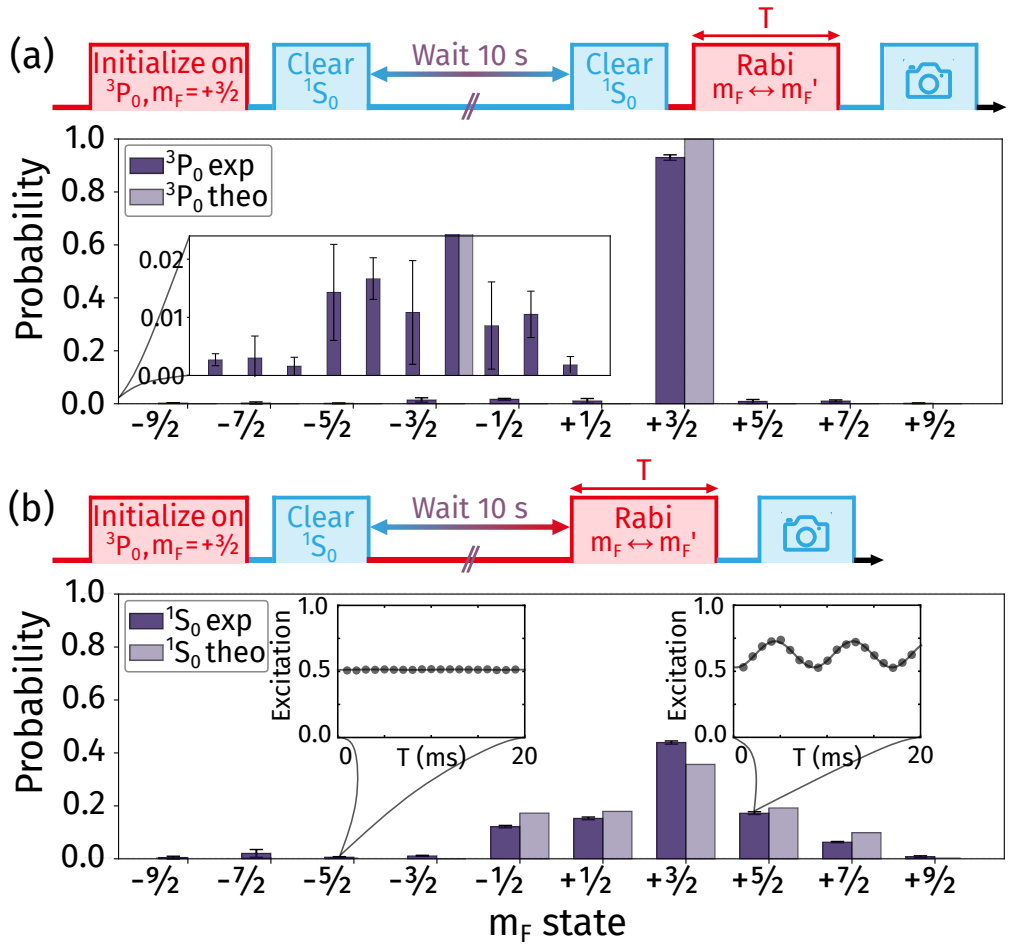


Figure 5.3: Hyperfine state population ratio measurement of erasures. The top panel of (a) illustrates the sequence used to measure the excited-state population distribution. The system is first initialized in $|e, 3/2\rangle$, followed by a clean-up pulse to remove the ground-state population. After holding the atoms in the lattice for 10 s, another clean-up pulse eliminates remaining ground-state atoms. A specific clock transition $|g, m_F\rangle \leftrightarrow |e, m_F'\rangle$ is then driven for varying pulse durations to map out the $|g, m_F\rangle$ state population. The bottom panel displays the resulting excited-state population distribution, with an inset that zooms into the probability below 0.02 in order to show the population in m_F-states other than $|e, 3/2\rangle$ more clearly. Similarly, the top panel of (b) depicts the sequence used to measure the ground-state population. The bottom panel presents the corresponding population distribution. Dark purple bars indicate measured normalized m_F-state populations in g (lower panel) and e (upper panel), while light purple bars indicate the theoretically predicted populations. Insets: Representative Rabi oscillation plots of the $|g, -5/2\rangle \leftrightarrow |e, -7/2\rangle$ transition (left panel) and the $|g, 5/2\rangle \leftrightarrow |e, 7/2\rangle$ transition (right panel), respectively.

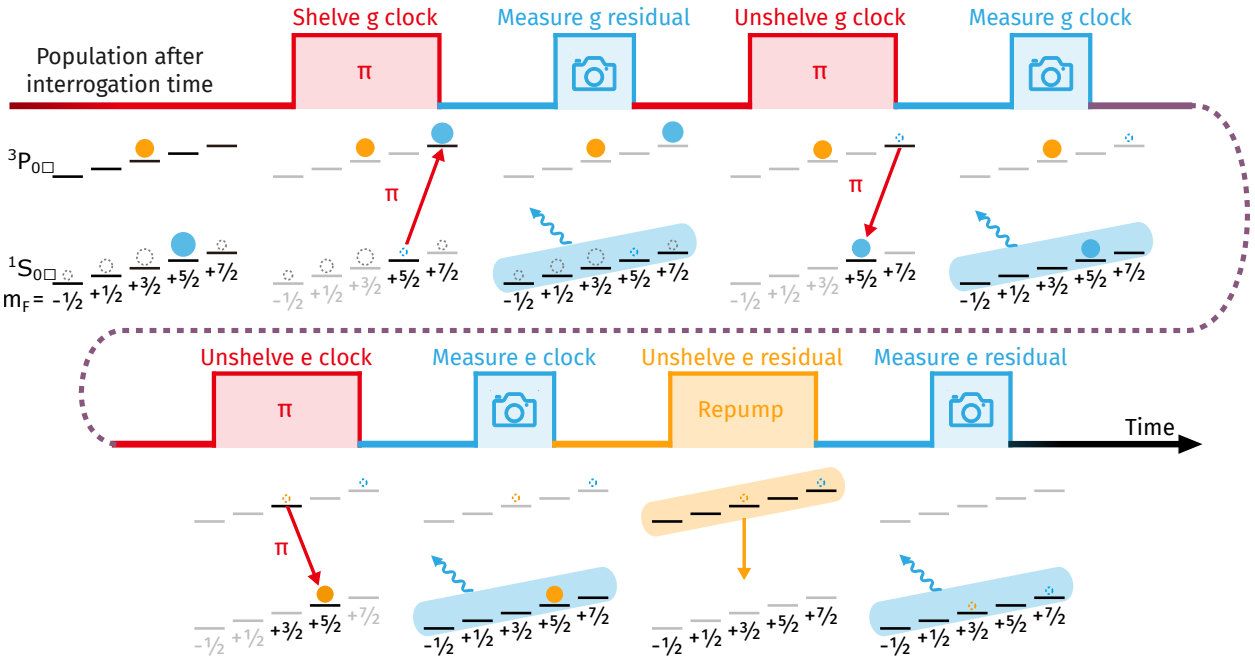


Figure 5.4: Illustration of pulse sequence used for hyperfine state resolved readout, starting with a quantum superposition between $|g, 5/2\rangle$ and $|e, 3/2\rangle$. The $|g, 5/2\rangle$ population is shelved in the clock state by a first π-pulse on resonant with the $|g, 5/2\rangle \rightarrow |e, 7/2\rangle$ transition; The remaining populations in g is measured ($N_{g,res}$) using a global imaging pulse ($\sim 25\ \mu$s) on the $^1S_0 \rightarrow {}^1P_1$ transition and at the same time erased from the remaining operations; A second clock π-pulse resonant with the $|e, 7/2\rangle \rightarrow |g, 5/2\rangle$ transition is used to coherently unshelve the population back to the ground state; The $|g, 5/2\rangle$ population ($N_{g,5/2}$) is measured using a second imaging pulse; The $|e, 3/2\rangle$ population is transferred to g via a third clock pulse on the $|e, 3/2\rangle \rightarrow |g, 5/2\rangle$ transition; The $|e, 3/2\rangle$ population ($N_{e,3/2}$) is measured using a third imaging pulse; The remaining populations in $^3P_0$ and $^3P_2$ are transferred back to g using standard global repump pulses on the $^3P_0 \rightarrow {}^3S_1$ and $^3P_2 \rightarrow {}^3S_1$ transitions; A final imaging pulse is applied to measure the residual excited state population ($N_{e,res}$).

calculated using:

$$P_{hf} = \frac{N_{e,3/2} - N_{bg}}{N_{e,3/2} + N_{g,5/2} - 2N_{bg}}, \tag{5.6}$$

while the reconstructed excitation fraction for standard readout, using the same data but including the measured residual atoms, is expressed as:

$$P_{recon} = \frac{N_{e,3/2} + N_{e,\mathrm{res}} - 2N_{bg}}{N_{e,3/2} + N_{g,5/2} + N_{g,\mathrm{res}} + N_{e,\mathrm{res}} - 4N_{bg}}. \tag{5.7}$$

5.6 Enhanced atomic coherence

We find that the atomic coherence is significantly improved by using hyperfine-resolved readout in synchronous differential comparisons employing both Ramsey and spin echo spectroscopy. In order to perform the comparisons, two spatially separated ensembles of ^{87}Sr atoms are co-trapped in a single 1D optical lattice and probed simultaneously by a shared clock laser along the axial direction [Fig. 5.2(a)]. The excitation fractions of the two ensembles are parametrically plotted and fitted to a resulting ellipse, from which the frequency difference between the two ensembles can be determined, as well as the Ramsey contrast of each atomic ensemble. This synchronous measurement bypasses the limitation on interrogation time imposed by the clock laser's phase noise [59].

5.6.1 Synchronous Ramsey spectroscopy

We first investigate atomic coherence using synchronous Ramsey spectroscopy [59], where the resulting ellipses are fitted using a maximum likelihood estimator (MLE; see Section A.1 for details).

An example of a comparison between the ellipses resulting from standard readout and hyperfine-resolved readout is shown in the inset of Fig. 5.5(i), taken at a trap depth of 75 E_{rec} with a Ramsey free evolution time of 12 s. Notably, we observe a significant enhancement in ellipse contrast when using hyperfine-resolved readout (cyan), achieving a factor of about 1.5 improvement compared to standard readout. Additionally, the reconstructed ellipse generated from hyperfine-resolved readout (orange) using Eq. (5.7) agrees well with the standard readout ellipse (blue).

In Fig. 5.5(a), we show the contrast as a function of coherence time for standard, hyperfine-resolved, and reconstructed readout methods. The fitted $1/e$ coherence time for hyperfine-resolved readout is 19(3) s, which is a factor of 1.4(1) longer than the coherence time obtained with standard readout (13(1) s). The numerically simulated contrast versus time using both hyperfine-resolved and standard readout shows reasonable agreement with the data.

We perform synchronous Ramsey spectroscopy at three lattice trap depths: 15, 45, and 75 E_{rec}. The fitted $1/e$ coherence times are plotted as a function of trap depth in Fig. 5.5(c). At 15 E_{rec}, we measure coherence times up to 120 s with hyperfine-resolved readout. Additionally,

reconstructed standard readout results from hyperfine-resolved readout measurements (cyan filled circles) closely match independently measured standard coherence (blue filled circles).

We numerically simulate the expected coherence times for each trap depth, incorporating the decoherence sources described in Section A.5. To model Ramsey spectroscopy, we also account for inhomogeneous dephasing effects such as the magnetic field gradient along the ensemble, measured to be 1.5 mG/cm. Additionally, other inhomogeneous broadening sources, such as residual Stark shifts, whose exact contributions remain uncertain, are modeled through a phenomenological Gaussian dephasing term with an empirically determined rate.

5.6.2 Modified synchronous spin echo spectroscopy

To further reduce decoherence from inhomogeneous broadening, we perform synchronous spin echo spectroscopy under similar experimental conditions. While the standard spin echo sequence effectively cancels much of the low-frequency differential frequency shifts such as those arising from magnetic field and lattice inhomogeneities, it typically also results in a differential phase shift ϕ between the two ensembles that is very close to 0 radians. At this phase, however, least-squares fitting [73] is heavily biased due to its numerical constraint enforcing an ellipse-specific solution. In contrast, maximum likelihood estimation (MLE) intrinsically reduces bias by incorporating a probabilistic noise model, which is particularly beneficial when the ellipse is primarily limited by quantum projection noise (QPN). A detailed description of MLE can be found in Section A.1. Although MLE has vanishing bias over a large range of phase, it remains slightly biased when ϕ is close to 0 radians because the fit cannot reliably distinguish between positive and negative values of ϕ, particularly in the presence of QPN. To ensure unbiased MLE, we introduce a transient magnetic field gradient along the lattice axis during the second free precession period of the spin echo sequence (see Section A.2 for details). This allows us to fine-tune the differential phase shift by adjusting the magnitude or duration of the applied gradient. To minimize potential impacts (such as decoherence) from the added transient gradient, we choose the lowest possible gradient ($\approx$ 2.0 mG/cm for 1.4 s), which results in a phase shift of 0.04 radians – sufficient for MLE to be unbiased.

We perform the modified synchronous spin echo spectroscopy at 5 different lattice trap depths: 15, 30, 45, 60, and 75 E_{rec}. The $1/e$ coherence times are fitted and plotted as a function of trap depth in Fig. 5.5(d). At a trap depth of 15 E_{rec}, we achieve atomic coherence times of up to 150 s after erasure conversion, about twice as long as when using standard readout under the same experimental conditions. Again, the reconstructed standard readout from hyperfine-resolved measurements and Eq. (5.7) (cyan empty circles) shows good agreement with independently measured coherence using standard readout (blue empty circles). Our numerical simulations of expected spin echo coherence as a function of trap depth show reasonable agreement with the data.

Notably, as shown in Fig. 5.5(e), the enhancement of coherence time in spin echo spectroscopy with hyperfine-resolved readout surpasses that of Ramsey spectroscopy across all trap depths. In Ramsey spectroscopy, wavefunction collapse induced by the non-Hermitian

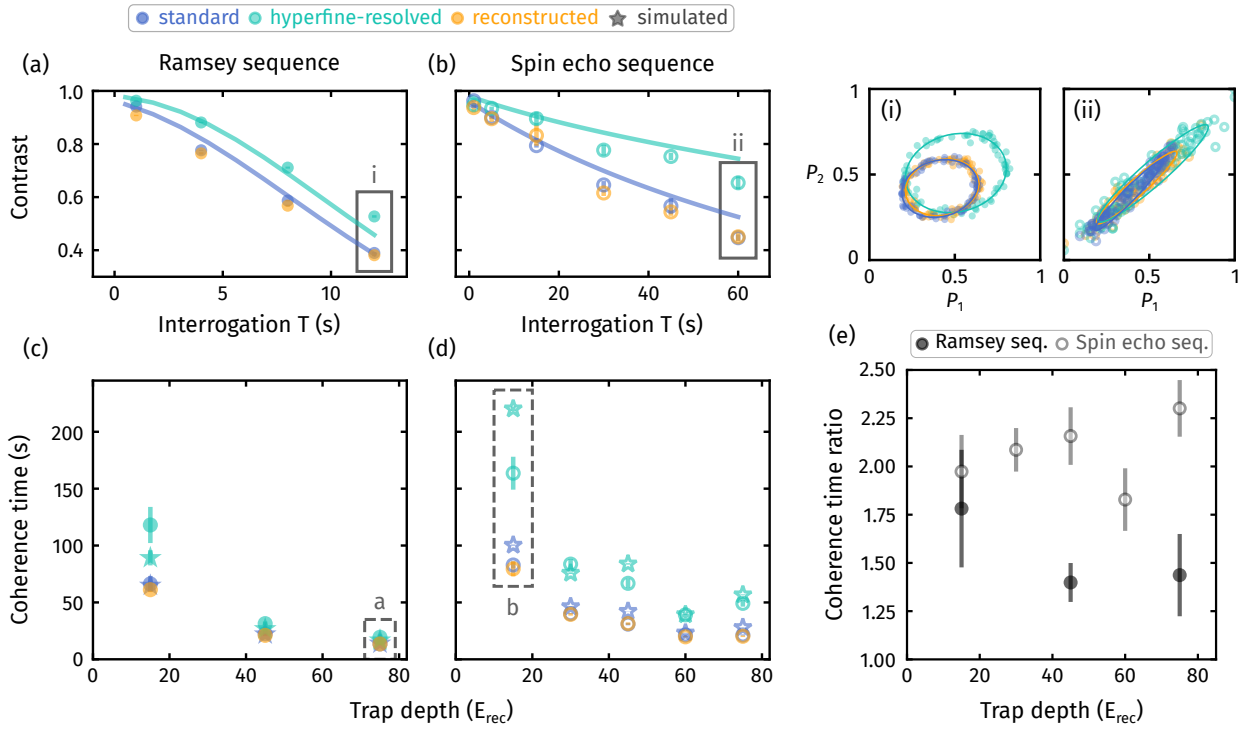


Figure 5.5: Comparison of coherence times using standard readout (blue), hyperfine-resolved readout (cyan), and reconstructed standard readout (orange) methods. Representative plots of coherence decay are shown in (a) for the Ramsey sequence at 75 E_{rec} (the highest trap depth measured in this work) and in (b) for the spin echo sequence at 15 E_{rec} (the lowest depth), with the corresponding comparison ellipses shown in panels (i) and (ii), respectively. Maximum likelihood estimation (MLE) is used to extract the atomic coherence. The solid curves are calculated through numerical simulation based on the known experimental parameters. (c) shows coherence time versus trap depth for the Ramsey sequence, while (d) presents the coherence time for the spin-echo sequence. Numerically simulated coherence times are indicated by star-shaped markers with matching color coding. (e) compares the enhancement ratio of the measured coherence time using erasure conversion for the Ramsey sequence (solid circles) and spin-echo sequence (hollow circles) as a function of depth. The measured and simulated coherence decay for the other trap depths are presented in Fig. A.3.

no-jump operator imposes a finite coherence time [150], even as the erasure fraction approaches 1. In contrast, the population swap due to the π-pulse in the spin echo sequence effectively erases the origin of the scattering, leading to a significant improvement in coherence time through erasure conversion. A more detailed discussion is provided in Section A.4, and additional plots of all measured coherence decays are included in Section A.7.

5.7 Resulting differential stabilities and the associated metrological gain

From the same measurements shown in Fig. 5.5, we extract differential clock comparison stabilities using the jackknife resampling technique (Section A.1). Representative Allan deviations (for 1 s averaging time) are presented in Fig. 5.6 (a)&(b) for standard and hyperfine-resolved readout, for both synchronous Ramsey and synchronous spin echo sequences. Despite achieving substantial enhancements in atomic coherence times, up to a factor of 1.5 to 2, the extracted stabilities with hyperfine-resolved readout do not show statistically significant improvement over standard readout. This limitation arises because while erasure conversion eliminates the excess noise arising from Raman scattering and radiative decay, the number of atoms that remain coherent and ultimately contribute to the measurement still falls exponentially with interrogation time, leading to a cap on the achievable fundamental improvement of $\sqrt{2}$ (or 2 in the limit of low duty cycle) in optimal clock stability [136]. Additionally, the finite erasure fraction and the infidelities (95–98% per pulse) in the additional clock π-pulses used for hyperfine-resolved readout further reduce the observed stability gains. We verify and isolate the impact of the imperfect π-pulses, which arise due to technical limitations and could in principle be mitigated (see Section A.6,) by comparing the stability achieved with hyperfine-resolved readout to that obtained using the reconstructed readout. Because the reconstructed readout method involves the same number of π-pulses as the hyperfine-resolved readout, and therefore also suffers from the same infidelities, this comparison reveals an enhancement in the lowest measured differential instability with hyperfine-resolved readout by factors of 1.22(6), 1.08(3), 1.62(6), 1.21(4), and 1.05(3) for lattice depths of 15, 30, 45, 60, and 75 E_{rec}, respectively, for the spin echo measurements. We attribute the additional fluctuations in clock stability across readout methods and interrogation times, which significantly exceed the uncertainty in the measured Allan deviation, to variance in the number of initially loaded atoms (detailed in Section A.7), along with contributions from uncompensated clock laser drift, which impacts the fidelity of the π-pulses used in the hyperfine-resolved and reconstructed readouts, as well as the relative accumulated phase between the two ensembles, which affects the stability of the differential clocks measurement as detailed in Refs. [56, 57, 59] and Section A.5.

While the benefits of erasure conversion are limited for conventional clock operation or traditional differential comparisons, where the interrogation time can be optimized to minimize the overall instability, it significantly reduces the dependence of instability on

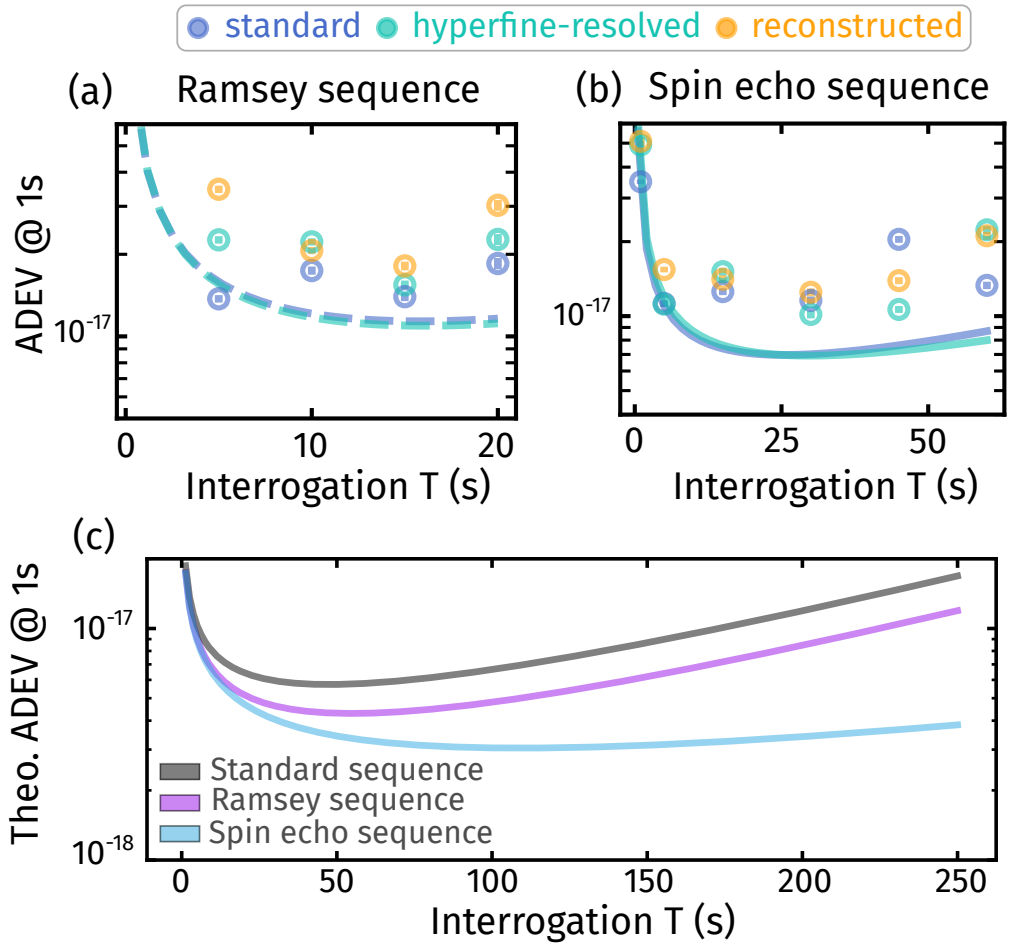


Figure 5.6: (a)&(b) show the extracted Allan deviations at 1 second for the differential clock comparisons for Ramsey (filled circles) and spin echo (empty circles), as well as using standard readout (blue), hyperfine-resolved readout (cyan), and reconstructed standard readout (orange), all taken at 15 E_{rec} depth. The error bar of each data point is on the order of 1×10^{-18}, and is thus not visible in the plot. The dashed curve in (a) represents the idealized Allan deviation, based only on the simulated coherence and the remaining number of atoms as a function of time, and does not include the relative phase difference between the two ensembles. In (b), the solid lines show the modeled Allan deviations for standard (blue) and hyperfine-resolved (cyan) readout, accounting for the accumulated phase between the two ensembles. Please see Section A.5 for details. (c) presents the theoretically predicted Allan deviation with 100% erasure fraction, assuming the only errors are radiative decay and Raman scattering, and 1000 initial number of atoms, for standard readout (black), Ramsey sequence (purple), and spin echo sequence (blue).

the interrogation time. Fig. 5.6(c), shows the theoretically calculated clock stability versus interrogation time for standard readout in the Ramsey sequence (black) and hyperfine-resolved readout in the Ramsey (purple) and spin echo (blue) sequences, assuming the contributing error sources including Raman scattering and spontaneous decay at trap depth of 15 E_{rec} and 100% erasure fraction. The simulation does not include the atom loss from lattice heating. See details about simulation in Section A.5. The enhanced coherence time in the spin echo sequence results in a flattening out of clock stability compared to standard readout. In applications requiring flexible interrogation times, such as gravitational wave detection [26] or dark matter searches [24], this relative insensitivity of stability to interrogation time could provide a significant advantage. Furthermore, the demonstrated extension of coherence time highlights potential applications beyond optical clocks, including the resolution of the line splittings beyond the limit set by the natural linewidth [146, 147].

To further enhance the achievable erasure fraction, one could utilize hyperfine states with larger separations, such as a superposition of $|g, 9/2\rangle$ and $|e, 3/2\rangle$ states which has the lowest magnetic field sensitivity (388 Hz/G) relative to all other transitions with $\Delta m_F \geq 3$. This configuration would effectively eliminate erasure contamination from Raman scattering and radiative decay. However, it would come at the cost of increased magnetic field sensitivity compared to the $|g, \pm 5/2\rangle \leftrightarrow |e, \pm 3/2\rangle$ transition employed here. Implementing this approach would therefore require careful mitigation of stray magnetic field gradients and additional clock π-pulses for coherent population transfer, imposing stricter requirements on clock pulse fidelities.

Finally, we note that our erasure conversion scheme relies on the large number of nuclear spin states of ^{87}Sr, and is not applicable to optical lattice clocks employing nuclear-spin-less isotopes or isotopes with spin-1/2, such as ^{171}Yb. However, in these systems, as well as in ^{87}Sr, alternative erasure conversion techniques could still be employed, such as the addition of a repumping laser out of $^3P_1$ during clock interrogation to suppress decays to $^1S_0$ and instead transfer scattered atoms into $^3P_2$. Naturally such an approach would come with its own trade-offs, such as large ac Stark shifts of the clock transition, and we leave investigation of this and other alternative approaches to future work.

5.8 Conclusion

We have experimentally demonstrated an erasure conversion protocol for optical clocks using hyperfine-resolved readout, effectively mitigating decoherence from lattice-light-induced Raman scattering and radiative decay. This approach extends atomic coherence times, achieving Ramsey spectroscopy coherence beyond 100 s and over 150 s with a spin echo sequence. Additionally, we developed a theoretical framework to describe erasure-enhanced coherence in both spectroscopy sequences, supported by numerical simulations incorporating Raman scattering, lattice Stark shifts, and density shifts. Our results demonstrate that hyperfine-resolved erasure detection not only suppresses decoherence from Raman scattering but also has the potential to fully unlock the benefits of ultra-narrow clock transitions, advancing the

performance of optical lattice clocks in applications requiring flexible interrogation times. Moreover, coherence enhancement via erasure conversion opens a new avenue for implementing sub-natural linewidth spectroscopy[146, 147].

Chapter 6

Future Work

In October of 2023, our lab group moved from the University of Wisconsin-Madison to the University of California, Berkeley, and we brought our experiment with us. At UC Berkeley, we have two experiments in development.

Our first planned experiment is the first direct test of the Einstein equivalence principle using the same experimental setup discussed throughout the rest of this thesis. The Einstein equivalence principle (EEP) states that there is a "complete physical equivalence" between a local system of test masses undergoing uniform acceleration and that same system experiencing the effects a gravitational field [151, 152]. The EEP can be constructed from the weak equivalence principle (WEP), which postulates the equivalence of inertial and gravitational mass, and the assumption of local Lorentz and local position invariance(LLI and LPI, respectively), which state that the outcomes of non-gravitational experiments are independent of the velocity and position in spacetime of the experiment [153]. The WEP has been tested extensively with many different types of experiments [154–160], with the MICROSCOPE experiment putting the lowest bounds on any WEP violations to below 4.25×10^{-15} by comparing the accelerations of test masses of different compositions on a drag-free satellite [160]. Local Lorentz invariance tests [161, 162] have been performed through many different types of experiments, including speed of light anisotropy [163, 164], vacuum dispersion [165–168],vacuum birefringence [169, 170], photon decay [171], and CPT violations in the neutral meson sector [172, 173]. The most sensitive terrestrial constraints on LLI come from nuclear or electronic spin coupling to LLI-violating background fields [174], which bounded neutron spin coupling to be below the 6.6×10^{-34}GeV level.

The least well constrained principle of the three is local position invariance. The best current bounds on LPI come from redshift measurements from atomic clocks based on different atomic species, which bound LPI violations below 7.6×10^{-7} [175]. Even though these three postulates have each been tested individually quite well, no experiment has yet tested all three simultaneously, motivating an experiment that can directly test the EEP.

In order to perform a direct test of the EEP, we plan to measure the gravitational redshift induced by an applied acceleration rather than from a gravitational field. In order to do this, our plan is to perform measurements similar to those in Chapter 3, but apply an acceleration

with our lattice not just when loading our atoms, but during the coherent interrogation time as well. Under these conditions, the ensembles will gain phase relative to each other based on the magnitude of the acceleration applied, which can be many times larger than the Earth's gravitational acceleration, g.

One concern that immediately arises with this setup is that for a 10 second Ramsey free evolution time, even just an acceleration of $1 \times g$ gives a vertical displacement of $g/2 \times (10)^2 = 490$ meters, or about 5.2 Sather Towers, well outside both the Rayleigh range of our lattice and vacuum system. In order to squeeze this much displacement to within our lattice's Rayleigh range of ≈5 cm, we will use a CPMG-style dynamical decoupling sequence [176, 177] with the π-pulses synchronized to changes in the acceleration direction of the lattice. The general scheme is shown in Fig. 6.1. Each upwards acceleration segment will see the bottom ensembles accrue more phase relative to the top ensembles, and the opposite for each downwards acceleration segment. Critically though, the π-pulse serves to swap the accrued phases of the ensembles, essentially allowing them to "trade places" with each other during the experiment. This acceleration swapping sequence also cancels out the DC signal of Earth's gravity. We are in the process of determining how much technical limitations will affect the number of acceleration segments we can perform, and thus how long we can interrogate for, but we expect to be either limited by atom loss at low lattice depths due to acceleration-induced heating, or π-pulse infidelity from our clock laser, which was previously a demonstrable technical limitation in Chapter 5.

The second experiment is currently under construction at our Berkeley lab and is essentially a larger, more sophisticated version of the redshift test performed in Chapter 3. This new system is pictured in Fig. 6.2. This system has three science regions across 1 meter of vertical displacement, over which we plan to test the gravitational redshift to a level that's competitive with the best current bounds. We plan to use the same synchronous Ramsey interrogation scheme for differential frequency shifts, but obviously there are some significant technical challenges to overcome in this system before performing these measurements. In order to actually displace atoms over 1 meter to bring them from the bottom MOT chamber to the science regions, we plan to use a separate transport beam using a 532 nm laser and a deformable lens to create an optical lattice with a movable focus spanning over 1 meter. The 813 nm stationary optical lattice for trapping during interrogation also has to have an extremely long Rayleigh range in order to be able to trap the clock ensembles at comparable depths across all three regions. In order to have sufficient trap depths in our stationary lattice, we created a 1.8 m long buildup cavity with two 1/2 inch mirrors at the top and bottom of the vacuum system, with a finesse of ≈ 640. The bottom mirror is mounted on a 2 cm piezo stack that has 15 μm of travel range to compensate changes in the cavity length that could cause phase shifts of the lattice during interrogation. However, we have already found that the external aluminum support structure expands more than this travel range with ambient conditions, since the linear coefficient of thermal expansion of Al $\approx 2 \times 10^{-5}$m/m K^{-1}, and therefore we would have to control the entire structure's temperature to about 0.5 K precision. Instead, we've chosen to construct a new support system for the cavity out of carbon fiber tubes, which have a factor of 10 lower linear coefficient of thermal expansion.

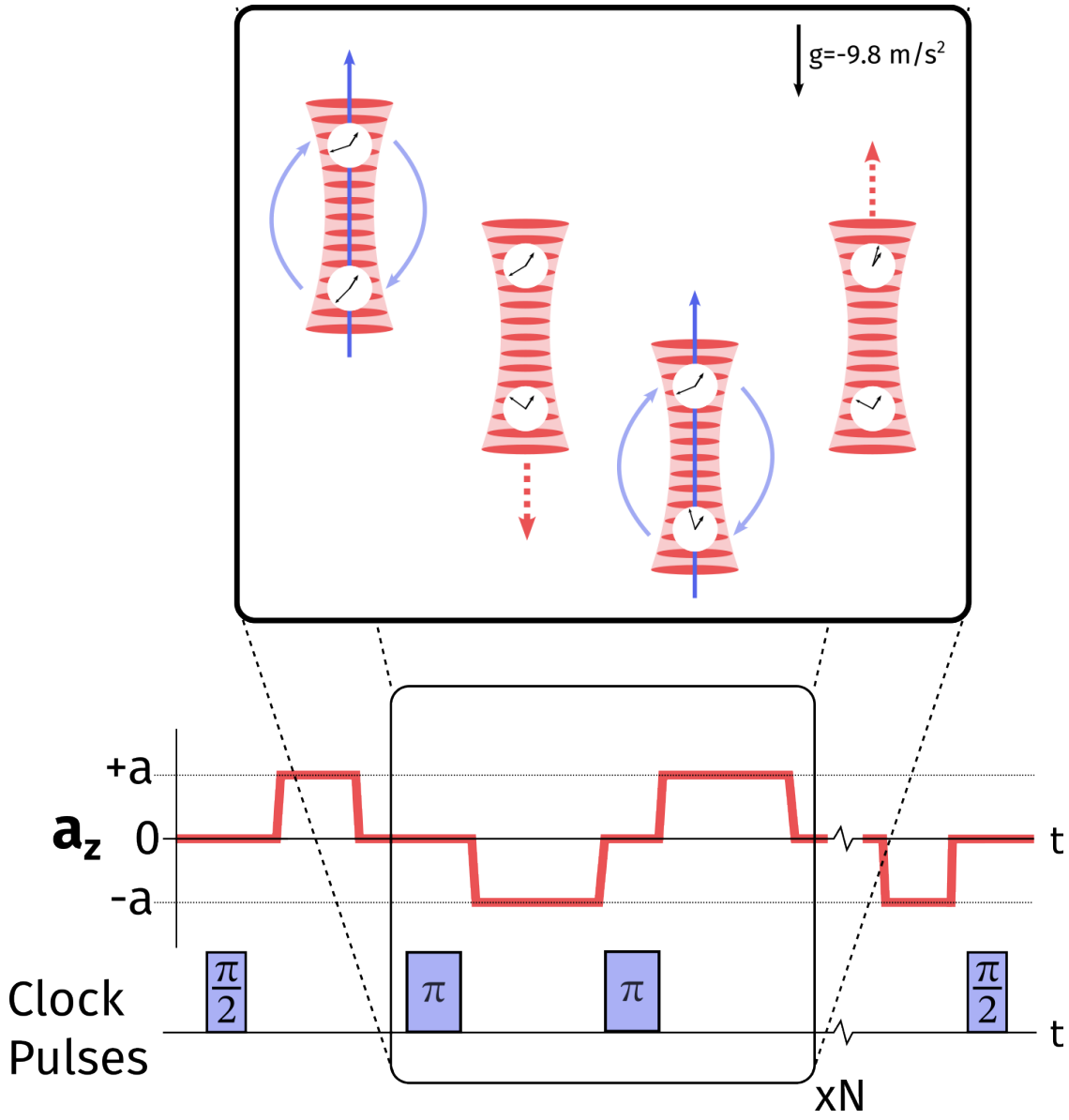


Figure 6.1: Diagram of planned test of the Einstein equivalence principle in our movable 1D lattice clock. During the interrogation of the atomic ensembles, we apply an acceleration to induce a redshift signal as predicted by the EEP. In order to average for a similar period of time as in our gravitational redshift measurements, we need to apply a sequence of dynamical decoupling pulse synchronized with the reversal of acceleration direction. This allows the AC applied acceleration redshift signal to continue to be tracked by our clock ensemble phases and for the DC gravitational redshift signal to be averaged out. The limit to the number of pulses will be set either by the pulse fidelity in our dynamical decoupling sequence, or atom loss due to acceleration-induced heating in our lattice.

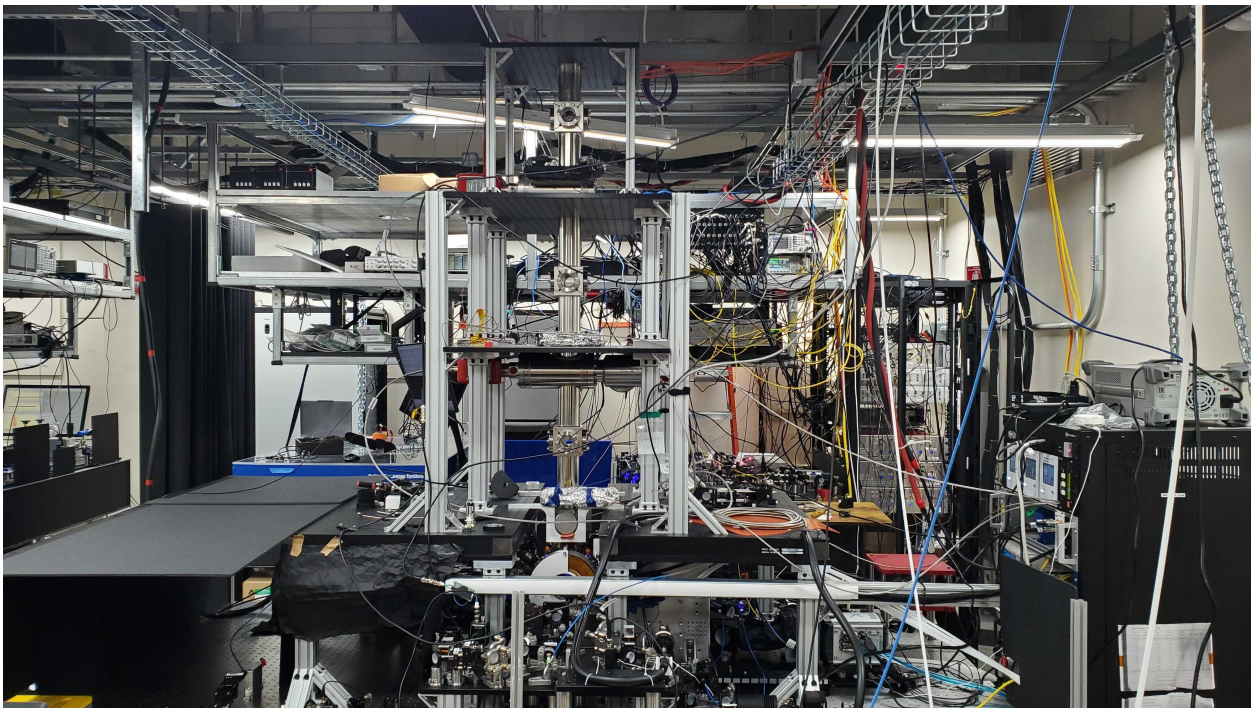


Figure 6.2: Photograph of our next-generation experiment. The distance between each science region in 0.5 meter, allowing us to probe the gravitational redshift signal at 1 meter.

Assuming we're able to measure the redshift in this system to the same frequency precision as in Chapter 3, the determination of α should improve by 2 orders of magnitude, or somewhere around 2×10^{-3}. On top of that, we want to push down differential systematics by an order of magnitude to be competitive at the low 10^{-4} with previous tests of the gravitational redshift [9, 12]. In order to do this, each science region will have added independent systematic controls, such as their own 3 axis bias field controls and μ-metal magnetic shielding. We should also be able to more precisely apply differential BBR shifts owing to the science region's larger spatial separations allowing for individual temperature control and measurement for each region.

Looking more broadly at where the atomic clock field is headed, there are a lot of exciting paths to carve out. One exciting prospect is the redefinition of the SI second based on an optical frequency standard [178] as clocks based on optical frequencies have already demonstrated stabilities more than two orders of magnitude better than the current Cs clocks. This move towards the redefinition of the second would help to enable precision timekeeping dissemination that could be useful for fundamental physics tests, quantum communication, and long-baseline geodesy.

Another exciting direction is the exploration of an atomic clock based on a nuclear transition in Thorium-229. First investigated in the early 2000s [179], the nuclear transition

from ^{229}Th to ^{229m}Th is notably very low energy compared to other nuclear transitions at 8.4 eV or 148 nm and a natural linewidth of $\Gamma \approx 2\pi\times$ 70 μHz. A high frequency vacuum-UV (VUV) transition is beneficial for clock performance as you can get more oscillations in the same amount of time, the same argument for why an optical clock could perform better than a microwave clock. However, this VUV transition is much harder to actually address, as lasers in the UV range are much harder to produce compared to visible wavelength lasers. This high frequency is not the only advantage of the nuclear clock, as nuclear transitions tend to be much less sensitive to environmental effects compared to electronic effects. For example, the nuclear magneton is a factor of electron mass/proton mass $\approx$ 1800 times less than the Bohr magneton, making it much less sensitive to external magnetic fields that could perturb this transition. Furthermore, the fundamental physics prospects are quite exciting, as this nuclear transition is sensitive to the interplay between the electromagnetic force and strong nuclear force. This transition has been experimentally observed and characterized [180–184], and new developments and experiments seem to be happening quite quickly.

One final interesting development is zero-dead-time (ZDT) optical clocks. As the name implies, these types of clocks operate with no time inbetween interrogation cycles, allowing for continuous feedback to the local oscillator/clock laser, eliminating the Dick Effect in this type of clock operation. This has been demonstrated before using two interleaved optical clocks [112], but work is also being done on creating a continuous clock by transporting cold strontium in a moving lattice and constantly interrogating atoms along the lattice axis with a clock laser [52, 53]. Alternatively, this continuous beam can be used to push towards a continuous millihertz-level linewidth superradiant laser based on the strontium clock transition [185, 186]. The ability to use optical lattices as a way to transport ultra-cold and confined atomic samples opens up a lot of interesting possibilities for the future of optical atomic timekeeping.

With all that said, things are looking very exciting for the atomic clock community, and it will be very interesting to see what new advances and discoveries are lying in wait.

Bibliography

[1] L. Essen and J. V. L. Parry. "An Atomic Standard of Frequency and Time Interval: A Cæsium Resonator". In: *Nature* 176.4476 (Aug. 1955), pp. 280–282. ISSN: 1476-4687. DOI: 10.1038/176280a0.

[2] J. Terrien. "News from the International Bureau of Weights and Measures". In: *Metrologia* 4.1 (Jan. 1968), p. 41. DOI: 10.1088/0026-1394/4/1/006.

[3] Wayne M. Itano and Norman F. Ramsey. "Accurate measurement of time". In: *Scientific American* 269.1 (July 1993), pp. 56–59. DOI: 10.1038/scientificamerican0793-56.

[4] David W. Allan, Neil Ashby, and Clifford C. Hodge. *The Science of Timekeeping.* Application Note. Hewlett Packard, 1997. URL: http://www.allanstime.com/Publications/DWA/Science_Timekeeping/.

[5] B. Hofmann-Wellenhof, H. Lichtenegger, and J. Collins. *Global Positioning System. Theory and practice.* Springer Vienna, 1993. ISBN: 978-3-7091-6199-9. DOI: 10.1007/978-3-7091-6199-9.

[6] J. C. Camparo, R. P. Frueholz, and A. P. Dubin. "Precise time synchronization of two Milstar communications satellites without ground intervention". In: *International Journal of Satellite Communications* 15.3 (1997), pp. 135–139. DOI: 10.1002/(SICI)1099-1247(199705/06)15:3<135::AID-SAT571>3.0.CO;2-O.

[7] M.S. Grewal, A.P. Andrews, and C.G. Bartone. *Global Navigation Satellite Systems, Inertial Navigation, and Integration.* Wiley, 2015. ISBN: 978-1-118-52353-7. URL: https://books.google.com/books?id=YIAxBwAAQBAJ.

[8] Bernardo Jaduszliwer and James Camparo. "Past, present and future of atomic clocks for GNSS". In: *GPS Solutions* 25.1 (Jan. 2021), p. 27. ISSN: 1521-1886. DOI: 10.1007/s10291-020-01059-x.

[9] R. F. C. Vessot et al. "Test of Relativistic Gravitation with a Space-Borne Hydrogen Maser". In: *Phys. Rev. Lett.* 45 (26 Dec. 1980), pp. 2081–2084. DOI: 10.1103/PhysRevLett.45.2081.

[10] J. C. Hafele and R. Keating. "Around-the-world atomic clocks: predicted relativistic time gains". In: *Science* 177 (1977), pp. 166–168. DOI: 10.1126/science.177.4044.166.

[11] S. Herrmann et al. "Test of the gravitational redshift with Galileo satellites in an eccentric orbit". In: *Phys. Rev. Lett.* 121 (2018), p. 231102. DOI: 10.1103/PhysRevLett.121.231102.

[12] Masao Takamoto et al. "Test of general relativity by a pair of transportable optical lattice clocks". In: *Nature Photonics* 14.7 (July 2020), pp. 411–415. ISSN: 1749-4893. DOI: 10.1038/s41566-020-0619-8.

[13] C. R. Pollock et al. "Direct frequency measurements of transitions at 520 THz (576 nm) in iodine and 260 THz (1.15 μm) in neon". In: *Opt. Lett.* 8.3 (Mar. 1983), pp. 133–135. DOI: 10.1364/OL.8.000133.

[14] Y. Millerioux et al. "Towards an accurate frequency standard at $\lambda = 778$ nm using a laser diode stabilized on a hyperfine component of the Doppler-free two-photon transitions in rubidium". In: *Optics Communications* 108.1 (May 1994), pp. 91–96. ISSN: 0030-4018. DOI: 10.1016/0030-4018(94)90221-6.

[15] Jun Ye, L.-S. Ma, and John Hall. "Ultrastable optical frequency reference at 1.064 μm using a C2HD molecular overtone transition". In: *IEEE Transactions on Instrumentation and Measurement* 46 (Apr. 1997), pp. 178–182. ISSN: 00189456. DOI: 10.1109/19.571806.

[16] Jun Ye et al. "Absolute frequency atlas of molecular I_2 lines at 532 nm". In: *IEEE Transactions on Instrumentation and Measurement* 48.2 (1999), pp. 544–549. DOI: 10.1109/19.769654.

[17] A. Clairon et al. "Ramsey Resonance in a Zacharias Fountain". In: *Europhysics Letters* 16.2 (Sept. 1991), p. 165. DOI: 10.1209/0295-5075/16/2/008.

[18] G. Santarelli et al. "Frequency stability degradation of an oscillator slaved to a periodically interrogated atomic resonator". In: *IEEE Transactions on Ultrasonics, Ferroelectrics, and Frequency Control* 45.4 (July 1998). Number: 4 Conference Name: IEEE Transactions on Ultrasonics, Ferroelectrics, and Frequency Control, pp. 887–894. ISSN: 1525-8955. DOI: 10.1109/58.710548.

[19] Th. Udem et al. "Absolute Optical Frequency Measurement of the Cesium D_1 with a Mode-Locked Laser". In: *Phys. Rev. Lett.* 82.18 (May 1999), pp. 3568–3571. DOI: 10.1103/PhysRevLett.82.3568.

[20] David J. Jones et al. "Carrier-Envelope Phase Control of Femtosecond Mode-Locked Lasers and Direct Optical Frequency Synthesis". In: *Science* 288.5466 (2000), pp. 635–639. DOI: 10.1126/science.288.5466.635. eprint: https://www.science.org/doi/pdf/10.1126/science.288.5466.635.

[21] W. H. Oskay et al. "Single-Atom Optical Clock with High Accuracy". In: *Phys. Rev. Lett.* 97.2 (July 2006), p. 020801. DOI: 10.1103/PhysRevLett.97.020801.

[22] Benjamin M. Roberts et al. "Search for domain wall dark matter with atomic clocks on board global positioning system satellites". In: *Nature Communications* 8.1 (Oct. 2017), p. 1195. ISSN: 2041-1723. DOI: 10.1038/s41467-017-01440-4.

[23] P. Wsciło et al. "New bounds on dark matter coupling from a global network of optical atomic clocks". In: *Sci. Adv.* 4 (2018), eaau4869. DOI: 10.1126/sciadv.aau4869.

[24] Colin J. Kennedy et al. "Precision Metrology Meets Cosmology: Improved Constraints on Ultralight Dark Matter from Atom-Cavity Frequency Comparisons". In: *Phys. Rev. Lett.* 125 (20 Nov. 2020), p. 201302. DOI: 10.1103/PhysRevLett.125.201302.

[25] A. Derevianko and M. Pospelov. "Hunting for topological dark matter with atomic clocks". In: *Nature Physics* 10.12 (Dec. 2014), pp. 933–936. ISSN: 1745-2481. DOI: 10.1038/nphys3137.

[26] S. Kolkowitz et al. "Gravitational wave detection with optical lattice atomic clocks". In: *Phys. Rev. D* 94 (12 Dec. 2016), p. 124043. DOI: 10.1103/PhysRevD.94.124043.

[27] M. S. Safronova et al. "Search for new physics with atoms and molecules". In: *Rev. Mod. Phys.* 90 (2 June 2018), p. 025008. DOI: 10.1103/RevModPhys.90.025008.

[28] Ruxandra Bondarescu et al. "Geophysical applicability of atomic clocks: direct continental geoid mapping". In: *Geophysical Journal International* 191.1 (Oct. 2012), pp. 78–82. ISSN: 0956-540X. DOI: 10.1111/j.1365-246X.2012.05636.x.

[29] P. Delva and J. Lodewyck. "Atomic clocks: new prospects in metrology and geodesy". In: *Acta Futura* 7 (2013), pp. 67–78. DOI: 10.2420/AF07.2013.67.

[30] Tetsushi Takano et al. "Geopotential measurements with synchronously linked optical lattice clocks". In: *Nature Photonics* 10.10 (Oct. 2016), pp. 662–666. ISSN: 1749-4893. DOI: 10.1038/nphoton.2016.159.

[31] G. Lion et al. "Determination of a high spatial resolution geopotential model using atomic clock comparisons". In: *J. Geod.* 91 (2017), pp. 597–611. DOI: 10.1007/s00190-016-0986-6.

[32] J. Grotti et al. "Geodesy and metrology with a transportable optical clock". In: *Nat. Phys.* 14 (2018), pp. 437–441. DOI: 10.1038/s41567-017-0042-3.

[33] M. Fischer et al. "New Limits on the Drift of Fundamental Constants from Laboratory Measurements". In: *Phys. Rev. Lett.* 92.23 (June 2004), p. 230802. DOI: 10.1103/PhysRevLett.92.230802.

[34] T. Rosenband et al. "Frequency Ratio of Al^+ and Hg^+ Single-Ion Optical Clocks; Metrology at the 17th 12imal Place". In: *Science* 319.5871 (2008), pp. 1808–1812. DOI: 10.1126/science.1154622.

[35] I. I. Rabi et al. "The Molecular Beam Resonance Method for Measuring Nuclear Magnetic Moments. The Magnetic Moments of ${}_3Li^6$, ${}_3Li^7$ and ${}_9F^{19}$". In: *Phys. Rev.* 55.6 (Mar. 1939), pp. 526–535. DOI: 10.1103/PhysRev.55.526.

[36] Norman F. Ramsey. "A Molecular Beam Resonance Method with Separated Oscillating Fields". In: *Phys. Rev.* 78.6 (June 1950), pp. 695–699. DOI: 10.1103/PhysRev.78.695.

[37] W. M. Itano et al. "Quantum projection noise: Population fluctuations in two-level systems". en. In: *Physical Review A* 47.5 (May 1993). Number: 5, pp. 3554–3570. ISSN: 1050-2947, 1094-1622. DOI: 10.1103/PhysRevA.47.3554.

[38] D.W. Allan. "Statistics of atomic frequency standards". In: *Proceedings of the IEEE* 54.2 (1966), pp. 221–230. DOI: 10.1109/PROC.1966.4634.

[39] D W Allan et al. *Characterization of clocks and oscillators*. en. Tech. rep. NBS TN 1337. Issue: NBS TN 1337 Edition: 0. Gaithersburg, MD: National Bureau of Standards, 1990, NBS TN 1337. DOI: 10.6028/NIST.TN.1337.

[40] Edwin Pedrozo-Peñafiel et al. "Entanglement on an optical atomic-clock transition". In: *Nature* 588.7838 (Dec. 2020), pp. 414–418. ISSN: 1476-4687. DOI: 10.1038/s41586-020-3006-1.

[41] William J. Eckner et al. "Realizing spin squeezing with Rydberg interactions in an optical clock". In: *Nature* 621.7980 (Sept. 2023), pp. 734–739. ISSN: 1476-4687. DOI: 10.1038/s41586-023-06360-6.

[42] Johannes Franke et al. "Quantum-enhanced sensing on optical transitions through finite-range interactions". In: *Nature* 621.7980 (Sept. 2023), pp. 740–745. ISSN: 1476-4687. DOI: 10.1038/s41586-023-06472-z.

[43] John M. Robinson et al. "Direct comparison of two spin-squeezed optical clock ensembles at the 10−17 level". In: *Nature Physics* 20.2 (Feb. 2024), pp. 208–213. ISSN: 1745-2481. DOI: 10.1038/s41567-023-02310-1.

[44] Mason C. Marshall et al. "High-Stability Single-Ion Clock with 5.5×10^{-19} Systematic Uncertainty". In: *Phys. Rev. Lett.* 135.3 (July 2025), p. 033201. DOI: 10.1103/hb3c-dk28.

[45] Irène Courtillot et al. "Clock transition for a future optical frequency standard with trapped atoms". In: *Phys. Rev. A* 68 (3 Sept. 2003), p. 030501. DOI: 10.1103/PhysRevA.68.030501.

[46] Martin M. Boyd et al. "Nuclear spin effects in optical lattice clocks". In: *Phys. Rev. A* 76 (2 Aug. 2007), p. 022510. DOI: 10.1103/PhysRevA.76.022510.

[47] T. Kessler et al. "A sub-40-mHz-linewidth laser based on a silicon single-crystal optical cavity". In: *Nat. Photon.* 6 (2012), pp. 687–692. DOI: 10.1038/nphoton.2012.217.

[48] D. G. Matei et al. "1.5 μm Lasers with Sub-10 mHz Linewidth". In: *Phys. Rev. Lett.* 118.26 (June 2017), p. 263202. DOI: 10.1103/PhysRevLett.118.263202.

[49] W. Zhang et al. "Ultrastable silicon cavity in a continuously operating closed-cycle cryostat at 4 K". In: *Phys. Rev. Lett.* 119 (2017), p. 243601. DOI: 10.1103/PhysRevLett.119.243601.

[50] J. M. Robinson et al. "Crystalline optical cavity at 4 K with thermal-noise-limited instability and ultralow drift". In: *Optica* 6 (2019), pp. 240–243. DOI: 10.1364/OPTICA.6.000240.

[51] Dhruv Kedar et al. "Frequency stability of cryogenic silicon cavities with semiconductor crystalline coatings". In: *Optica* 10.4 (Apr. 2023), pp. 464–470. DOI: 10.1364/OPTICA.479462.

[52] Hidetoshi Katori. "Longitudinal Ramsey spectroscopy of atoms for continuous operation of optical clocks". In: *Applied Physics Express* 14.7 (July 2021), p. 072006. DOI: 10.35848/1882-0786/ac0e16.

[53] Shoichi Okaba et al. "Continuous generation of an ultracold atomic beam using crossed moving optical lattices". In: *Phys. Rev. Appl.* 21.3 (Mar. 2024), p. 034006. DOI: 10.1103/PhysRevApplied.21.034006.

[54] E. R. Clements et al. "Lifetime-limited interrogation of two independent $^{27}Al^{+}$ clocks using correlation spectroscopy". In: *Phys. Rev. Lett.* 125 (2020), p. 243602. DOI: 10.1103/PhysRevLett.125.243602.

[55] S. L. Campbell et al. "A Fermi-degenerate three-dimensional optical lattice clock". In: *Science* 358 (2017), pp. 90–94. DOI: 10.1126/science.aam5538.

[56] G. E. Marti et al. "Imaging optical frequencies with 100 μHz precision and 1.1 μm resolution". In: *Phys. Rev. Lett.* 120 (2018), p. 103201. DOI: 10.1103/PhysRevLett.120.103201.

[57] Aaron W. Young et al. "Half-minute-scale atomic coherence and high relative stability in a tweezer clock". In: *Nature* 588.7838 (Dec. 2020), pp. 408–413. ISSN: 1476-4687. DOI: 10.1038/s41586-020-3009-y.

[58] Yue Wu et al. "Erasure conversion for fault-tolerant quantum computing in alkaline earth Rydberg atom arrays". In: *Nature Communications* 13.1 (Aug. 2022), p. 4657. ISSN: 2041-1723. DOI: 10.1038/s41467-022-32094-6.

[59] Xin Zheng et al. "Differential clock comparisons with a multiplexed optical lattice clock". In: *Nature* 602.7897 (Feb. 2022), pp. 425–430. ISSN: 1476-4687. DOI: 10.1038/s41586-021-04344-y.

[60] A. Keshet. "A next-generation apparatus for lithium optical lattice experiments". PhD thesis. Massachusetts Institute of Technology, 2013.

[61] S. Campbell. "A Fermi-degenerate three-dimensional optical lattice clock". PhD thesis. University of Colorado Boulder, 2017.

[62] Masami Yasuda and Hidetoshi Katori. "Lifetime Measurement of the $^3P_2$ Metastable State of Strontium Atoms". In: *Phys. Rev. Lett.* 92.15 (Apr. 2004), p. 153004. DOI: 10.1103/PhysRevLett.92.153004.

[63] Oleksiy Onishchenko et al. "Frequency of the ultranarrow $^1S_0 \rightarrow ^3 P_2$ transition in ^{87}Sr". In: *Phys. Rev. A* 99.5 (May 2019), p. 052503. DOI: 10.1103/PhysRevA.99.052503.

[64] M. M. Boyd. "High Precision Spectroscopy of Strontium in an Optical Lattice: Towards a New Standard for Frequency and Time". PhD thesis. University of Colorado Boulder, 2013.

[65] T. L. Nicholson et al. "Systematic evaluation of an atomic clock at 2×10^{-18} total uncertainty". In: *Nature Communications* 6.1 (2015), p. 6896. DOI: 10.1038/ncomms7896.

[66] Tobias Bothwell et al. "JILA SrI optical lattice clock with uncertainty of 2.0×10^{-18}". In: *Metrologia* 56.6 (Oct. 2019), p. 065004. DOI: 10.1088/1681-7575/ab4089.

[67] Alexander Aeppli et al. "Clock with 8×10^{-19} Systematic Uncertainty". In: *Phys. Rev. Lett.* 133 (2 July 2024), p. 023401. DOI: 10.1103/PhysRevLett.133.023401.

[68] Kyungtae Kim et al. "Atomic Coherence of 2 Minutes and Instability of 1.5×10^{-18} at 1 s in a Wannier-Stark Lattice Clock". In: *Phys. Rev. Lett.* 135 (10 Sept. 2025), p. 103601. DOI: 10.1103/3wtv-sty2.

[69] Andrew D. Ludlow et al. "Optical atomic clocks". In: *Rev. Mod. Phys.* 87 (2 June 2015), pp. 637–701. DOI: 10.1103/RevModPhys.87.637.

[70] P. Lemonde and P. Wolf. "Optical lattice clock with atoms confined in a shallow trap". In: *Phys. Rev. A* 72 (2005), p. 033409. DOI: 10.1103/PhysRevA.72.033409.

[71] William R. Milner et al. "Demonstration of a Timescale Based on a Stable Optical Carrier". In: *Phys. Rev. Lett.* 123 (17 Oct. 2019), p. 173201. DOI: 10.1103/PhysRevLett.123.173201.

[72] Abraham. Savitzky and M. J. E. Golay. "Smoothing and Differentiation of Data by Simplified Least Squares Procedures." In: *Analytical Chemistry* 36.8 (July 1964), pp. 1627–1639. ISSN: 0003-2700. DOI: 10.1021/ac60214a047.

[73] R. Halir and J. Flusser. "Numerically stable direct least squares fitting of ellipses". In: *Proc. of Sixth Intl Conf. Computer Graphics and Visualization*. Vol. 1. 1998. URL: https://api.semanticscholar.org/CorpusID:15772208.

[74] B. V. Estey. "Precision Measurement in Atom Interferometry Using Bragg Diffraction". PhD thesis. Univeristy of California, Berkeley, 2016.

[75] Matthew A. Norcia et al. "Seconds-scale coherence on an optical clock transition in a tweezer array". In: *Science* 366.6461 (2019), pp. 93–97. DOI: 10.1126/science.aay0644. eprint: https://www.science.org/doi/pdf/10.1126/science.aay0644.

[76] Ivaylo S. Madjarov et al. "An Atomic-Array Optical Clock with Single-Atom Readout". In: *Phys. Rev. X* 9.4 (Dec. 2019), p. 041052. DOI: 10.1103/PhysRevX.9.041052.

[77] A. V. Taichenachev et al. "Magnetic Field-Induced Spectroscopy of Forbidden Optical Transitions with Application to Lattice-Based Optical Atomic Clocks". In: *Phys. Rev. Lett.* 96.8 (Mar. 2006), p. 083001. DOI: 10.1103/PhysRevLett.96.083001.

[78] Cédric Delaunay et al. "Probing atomic Higgs-like forces at the precision frontier". In: *Phys. Rev. D* 96.9 (Nov. 2017), p. 093001. DOI: 10.1103/PhysRevD.96.093001.

[79] Julian C. Berengut et al. "Probing New Long-Range Interactions by Isotope Shift Spectroscopy". In: *Phys. Rev. Lett.* 120.9 (Feb. 2018), p. 091801. DOI: 10.1103/PhysRevLett.120.091801.

[80] Tetsushi Takano, Ray Mizushima, and Hidetoshi Katori. "Precise determination of the isotope shift of ^{88}Sr–^{87}Sr optical lattice clock by sharing perturbations". In: *Applied Physics Express* 10.7 (June 2017), p. 072801. DOI: 10.7567/APEX.10.072801.

[81] Hirokazu Miyake et al. "Isotope-shift spectroscopy of the $^1S_0 \rightarrow ^3P_1$ and $^1S_0 \rightarrow ^3P_0$ transitions in strontium". In: *Phys. Rev. Res.* 1.3 (Nov. 2019), p. 033113. DOI: 10.1103/PhysRevResearch.1.033113.

[82] Zhuang Ge et al. "High-precision measurement of the atomic mass of ^{84}Sr and implications to isotope shift studies". In: *The European Physical Journal A* 60.7 (July 2024), p. 147. ISSN: 1434-601X. DOI: 10.1140/epja/s10050-024-01359-7.

[83] Julian C. Berengut and Natalia S. Oreshkina. "Second-order hyperfine structure and its impact on searches for new physics using isotope-shift spectroscopy". In: *Phys. Rev. A* 112.2 (Aug. 2025), p. 022804. DOI: 10.1103/qkv8-z8z1.

[84] Xin Zheng et al. "A lab-based test of the gravitational redshift with a miniature clock network". In: *Nature Communications* 14.1 (Aug. 2023), p. 4886. ISSN: 2041-1723. DOI: 10.1038/s41467-023-40629-8.

[85] A. Einstein. "Grundgedanken der allgemeinen Relativitätstheorie und Anwendung dieser Theorie in der Astronomie". In: *Sitzungsberichte, Preuss. Akad. der Wissenschaften* 315 (1915), pp. 778–786.

[86] C. M. Will. "The confrontation between general relativity and experiment". In: *Living Rev. Relativ.* 17 (2014), p. 4. DOI: 10.12942/lrr-2014-4.

[87] F. W. Dyson, A. S. Eddington, and C. Davidson. "IX. A determination of the deflection of light by the sun's gravitational field, from observations made at the total eclipse of May 29, 1919". In: *Philosophical Transactions of the Royal Society of London. Series A, Containing Papers of a Mathematical or Physical Character* 220 (1920), pp. 291–333.

[88] G. M. Clemence. "The relativity effect in planetary motions". In: *Rev. Mod. Phys.* 19 (1947), pp. 361–364. DOI: 10.1103/RevModPhys.19.361.

[89] R. V. Pound and G. A. Rebka. "Gravitational red-shift in nuclear resonance". In: *Phys. Rev. Lett.* 3 (1959), p. 439. DOI: 10.1103/PhysRevLett.3.439.

[90] I. Ciufolini and E. C. Pavlis. "A confirmation of the general relativistic prediction of the Lense–Thirring effect". In: *Nature* 431 (2004), pp. 958–960. DOI: 10.1038/nature03007.

[91] I. H. Stairs. "Testing general relativity with pulsar timing". In: *Living Rev. Relativ.* 6 (2003), p. 5. DOI: 10.12942/lrr-2003-5.

[92] B. P. Abbott et al. "Observation of gravitational waves from a binary black hole merger". In: *Phys. Rev. Lett.* 116 (2016), p. 061102. DOI: 10.1103/PhysRevLett.116.061102.

[93] A. M. Archibald et al. "Universality of free fall from the orbital motion of a pulsar in a stellar triple system". In: *Nature* 559 (2018), pp. 73–76. DOI: 10.1038/s41586-018-0265-1.

[94] R. Colella, A. W. Overhauser, and S. A. Werner. "Observation of gravitationally induced quantum interference". In: *Phys. Rev. Lett.* 34 (1975), p. 1472. DOI: 10.1103/PhysRevLett.34.1472.

[95] Don N. Page and C. D. Geilker. "Indirect evidence for quantum gravity". In: *Phys. Rev. Lett.* 47 (1981), p. 979. DOI: 10.1103/PhysRevLett.47.979.

[96] M. Zych et al. "Quantum interferometric visibility as a witness of general relativistic proper time". In: *Nat. Comm.* 2 (2011), pp. 1–7. DOI: 10.1038/ncomms1498.

[97] N. Huntemann et al. "Single-Ion Atomic Clock with 3×10^{-18} Systematic Uncertainty". In: *Phys. Rev. Lett.* 116 (6 Feb. 2016), p. 063001. DOI: 10.1103/PhysRevLett.116.063001.

[98] W. F. McGrew et al. "Atomic clock performance enabling geodesy below the centimetre level". In: *Nature* 564.7734 (Dec. 2018), pp. 87–90. ISSN: 1476-4687. DOI: 10.1038/s41586-018-0738-2.

[99] S. M. Brewer et al. "$^{27}Al^{+}$ Quantum-Logic Clock with a Systematic Uncertainty below 10^{-18}". In: *Phys. Rev. Lett.* 123 (3 July 2019), p. 033201. DOI: 10.1103/PhysRevLett.123.033201.

[100] E. Oelker et al. "Demonstration of 4.8×10^{-17} stability at 1 s for two independent optical clocks". In: *Nature Photonics* 13.10 (Oct. 2019), pp. 714–719. ISSN: 1749-4893. DOI: 10.1038/s41566-019-0493-4.

[101] C. W. Chou et al. "Optical Clocks and Relativity". In: *Science* 329.5999 (2010), pp. 1630–1633. DOI: 10.1126/science.1192720.

[102] P. Delva et al. "Gravitational redshift test using eccentric Galileo satellites". In: *Phys. Rev. Lett.* 121 (2018), p. 231101. DOI: 10.1103/PhysRevLett.121.231101.

[103] Tobias Bothwell et al. "Resolving the gravitational redshift across a millimetre-scale atomic sample". In: *Nature* 602.7897 (Feb. 2022), pp. 420–424. ISSN: 1476-4687. DOI: 10.1038/s41586-021-04349-7.

[104] N. Ohmae et al. "Transportable Strontium Optical Lattice Clocks Operated Outside Laboratory at the Level of 10^{-18} Uncertainty". In: *Adv. Quantum Technol.* 4 (2021), p. 2100015. DOI: 10.1002/qute.202100015.

[105] Y. Huang et al. "A compact, transportable single-ion optical clock with 7.8×10^{-17} systematic uncertainty". In: *Appl. Phys. B* 123 (2017), p. 112. DOI: 10.1007/s00340-017-6671-5.

[106] P. Delva, H. Denker, and G. Lion. "Chronometric Geodesy: Methods and Applications". In: *Relativistic Geodesy. Fundamental Theories of Physics*. Vol. 196. 2019, pp. 25–85. DOI: 10.1007/978-3-030-11500-5_2.

[107] H. Denker et al. "Geodetic methods to determine the relativistic redshift at the level of 10^{-18} in the context of international timescales – A review and practical results". In: *Journal of Geodesy* 92 (2018), pp. 487–516. DOI: 10.1007/s00190-017-1075-1.

[108] T. E. Mehlstäubler et al. "Atomic clocks for geodesy". In: *Reports on Progress in Physics* 81 (2018), p. 064401. DOI: 10.1088/1361-6633/aab409.

[109] Y. Huang et al. "Geopotential measurement with a robust, transportable Ca^+ optical clock". In: *Phys. Rev. A* 102 (2020), 050802(R). DOI: 10.1103/PhysRevA.102.050802.

[110] S. B. Koller et al. "Transportable optical lattice clock with 7×10^{-17} uncertainty". In: *Phys. Rev. Lett.* 118 (2017), p. 073601. DOI: 10.1103/PhysRevLett.118.073601.

[111] M. Takamoto, T. Takano, and H. Katori. "Frequency comparison of optical lattice clocks beyond the Dick limit". In: *Nat. Photon.* 5 (2011), pp. 288–292. DOI: 10.1103/PhysRevLett.114.230801.

[112] M. Schioppo et al. "Ultrastable optical clock with two cold-atom ensembles". In: *Nat. Photon.* 11 (2017), pp. 48–52. DOI: 10.1038/nphoton.2016.231.

[113] M. E. Kim et al. "Improved interspecies optical clock comparisons through differential spectroscopy". In: *Nat. Phys.* 19 (2023), pp. 25–29. DOI: 10.1038/s41567-022-01794-7.

[114] M. J. Martin et al. "A quantum many-body spin system in an optical lattice clock". In: *Science* 341 (2013), pp. 632–636. DOI: 10.1126/science.1236929.

[115] X. Zhang et al. "Spectroscopic observation of SU(N)-symmetric interactions in Sr orbital magnetism". In: *Science* 345 (2014), pp. 1467–1473. DOI: 10.1126/science.1254978.

[116] A. Aeppli et al. "Hamiltonian engineering of spin-orbit–coupled fermions in a Wannier-Stark optical lattice clock". In: *Sci. Adv.* 8 (2022), eadc9242. DOI: 10.1126/sciadv.adc9242.

[117] R. C. Brown et al. "Hyperpolarizability and operational magic wavelength in an optical lattice clock". In: *Phys. Rev. Lett.* 119 (2017), p. 253001. DOI: 10.1103/PhysRevLett.119.253001.

[118] I. Ushijima, M. Takamoto, and H. Katori. "Operational magic intensity for Sr optical lattice clocks". In: *Phys. Rev. Lett.* 121 (2018), p. 263202. DOI: 10.1103/PhysRevLett.121.263202.

[119] K. Beloy et al. "Atomic clock with 1×10^{-18} room-temperature blackbody Stark uncertainty". In: *Phys. Rev. Lett.* 113 (2014), p. 260801. DOI: 10.1103/PhysRevLett.113.260801.

[120] I. Ushijima et al. "Cryogenic optical lattice clocks". In: *Nat. Photon.* 9 (2015), pp. 185–189. DOI: 10.1038/nphoton.2015.5.

[121] Philipp Haslinger et al. "Attractive force on atoms due to blackbody radiation". In: *Nature Physics* 14.3 (Mar. 2018), pp. 257–260. ISSN: 1745-2481. DOI: 10.1038/s41567-017-0004-9.

[122] K. Beloy et al. "Faraday-shielded DC Stark-shift-free optical lattice clock". In: *Phys. Rev. Lett.* 120 (2018), p. 183201. DOI: 10.1103/PhysRevLett.120.183201.

[123] Jonathan Dolde et al. "Direct measurement of the $^3P_0$ clock state natural lifetime in ^{87}Sr". In: *Phys. Rev. A* 112.2 (Aug. 2025), p. 023121. DOI: 10.1103/f6pt-flnt.

[124] Kyle Beloy et al. "Frequency ratio measurements at 18-digit accuracy using an optical clock network". In: *Nature* 591.7851 (Mar. 2021), pp. 564–569. ISSN: 1476-4687. DOI: 10.1038/s41586-021-03253-4.

[125] S Dörscher et al. "Optical frequency ratio of a $^{171}Yb^+$ single-ion clock and a ^{87}Sr lattice clock". In: *Metrologia* 58.1 (Jan. 2021), p. 015005. DOI: 10.1088/1681-7575/abc86f.

[126] Yusuke Hisai et al. "Improved frequency ratio measurement with ^{87}Sr and ^{171}Yb optical lattice clocks at NMIJ". In: *Metrologia* 58.1 (Jan. 2021), p. 015008. DOI: 10.1088/1681-7575/abc104.

[127] J. Grotti et al. "Long-distance chronometric leveling with a portable optical clock". In: *Phys. Rev. Appl.* 21 (6 June 2024), p. L061001. DOI: 10.1103/PhysRevApplied.21.L061001.

[128] Mahiro Abe et al. "Matter-wave Atomic Gradiometer Interferometric Sensor (MAGIS-100)". In: *Quantum Science and Technology* 6.4 (July 2021), p. 044003. DOI: 10.1088/2058-9565/abf719.

[129] Sven Abend et al. "Terrestrial very-long-baseline atom interferometry: Workshop summary". In: *AVS Quantum Science* 6.2 (2024). DOI: 10.1116/5.0185291.

[130] Katrina Barnes et al. "Assembly and coherent control of a register of nuclear spin qubits". In: *Nature Communications* 13.1 (2022), p. 2779. DOI: 10.1038/s41467-022-29977-z.

[131] Robin Santra, Kevin V. Christ, and Chris H. Greene. "Properties of metastable alkaline-earth-metal atoms calculated using an accurate effective core potential". In: *Phys. Rev. A* 69 (4 Apr. 2004), p. 042510. DOI: 10.1103/PhysRevA.69.042510.

[132] Xiaotong Lu et al. "M_F-dependent hyperfine-induced $5s5p\ ^3P_0^o - -5s^2\ ^1S_0$ clock transition rates in an external magnetic field for ^{87}Sr". In: *Phys. Rev. A* 108 (1 July 2023), p. 012820. DOI: 10.1103/PhysRevA.108.012820.

[133] Sören Dörscher et al. "Lattice-induced photon scattering in an optical lattice clock". In: *Phys. Rev. A* 97 (6 June 2018), p. 063419. DOI: 10.1103/PhysRevA.97.063419.

[134] Juan A. Muniz et al. "Cavity-QED measurements of the ^{87}Sr millihertz optical clock transition and determination of its natural linewidth". In: *Phys. Rev. Res.* 3 (2 May 2021), p. 023152. DOI: 10.1103/PhysRevResearch.3.023152.

[135] Xiao-Tong Lu et al. "Determining the lifetime of the $5s5p^3P_0^o$ metastable state in ^{87}Sr from the electric dipole matrix element". In: *Phys. Rev. Appl.* 21 (2 Feb. 2024), p. 024042. DOI: 10.1103/PhysRevApplied.21.024042.

[136] Pradeep Niroula et al. "Quantum Sensing with Erasure Qubits". In: *Phys. Rev. Lett.* 133 (8 Aug. 2024), p. 080801. DOI: 10.1103/PhysRevLett.133.080801.

[137] J. L. Siegel et al. "Excited-Band Coherent Delocalization for Improved Optical Lattice Clock Performance". In: *Phys. Rev. Lett.* 132 (13 Mar. 2024), p. 133201. DOI: 10.1103/PhysRevLett.132.133201.

[138] Ross B. Hutson et al. "Engineering Quantum States of Matter for Atomic Clocks in Shallow Optical Lattices". In: *Phys. Rev. Lett.* 123 (12 Sept. 2019), p. 123401. DOI: 10.1103/PhysRevLett.123.123401.

[139] M. Bishof et al. "Inelastic collisions and density-dependent excitation suppression in a ^{87}Sr optical lattice clock". In: *Phys. Rev. A* 84 (5 Nov. 2011), p. 052716. DOI: 10.1103/PhysRevA.84.052716.

[140] A. Traverso et al. "Inelastic and elastic collision rates for triplet states of ultracold strontium". In: *Phys. Rev. A* 79 (6 June 2009), p. 060702. DOI: 10.1103/PhysRevA.79.060702.

[141] G. Breit and Lawrence A. Wills. "Hyperfine Structure in Intermediate Coupling". In: *Phys. Rev.* 44.6 (Sept. 1933), pp. 470–490. DOI: 10.1103/PhysRev.44.470.

[142] Shuo Ma et al. "Enhancing Optical Lattice Clock Coherence Times with Erasure Conversion". In: *PRX Quantum* 6.4 (Nov. 2025), p. 040340. DOI: 10.1103/2rqf-r9gw.

[143] Shuo Ma et al. "High-fidelity gates and mid-circuit erasure conversion in an atomic qubit". In: *Nature* 622.7982 (Oct. 2023), pp. 279–284. ISSN: 1476-4687. DOI: 10.1038/s41586-023-06438-1.

[144] Pascal Scholl et al. "Erasure conversion in a high-fidelity Rydberg quantum simulator". In: *Nature* 622.7982 (Oct. 2023), pp. 273–278. ISSN: 1476-4687. DOI: 10.1038/s41586-023-06516-4.

[145] H. Levine et al. "Demonstrating a Long-Coherence Dual-Rail Erasure Qubit Using Tunable Transmons". In: *Phys. Rev. X* 14 (1 Mar. 2024), p. 011051. DOI: 10.1103/PhysRevX.14.011051.

[146] Dennis P. O'Brien, Pierre Meystre, and Herbert Walther. "Subnatural Linewidths in Atomic Spectroscopy". In: *Advances in Atomic and Molecular Physics*. Ed. by D.R. Bates and Benjamin Bederson. Vol. 21. Academic Press, 1985, pp. 1–49. DOI: 10.1016/S0065-2199(08)60140-2.

[147] Tuvia Gefen, Amit Rotem, and Alex Retzker. "Overcoming resolution limits with quantum sensing". In: *Nature communications* 10.1 (2019), p. 4992. DOI: 10.1038/s41467-019-12817-y.

[148] Youssef S Hassan et al. "Ratchet loading and multi-ensemble operation in an optical lattice clock". In: *Quantum Science and Technology* 9.4 (Aug. 2024), p. 045023. DOI: 10.1088/2058-9565/ad6286.

[149] H. Uys et al. "Decoherence due to Elastic Rayleigh Scattering". In: *Phys. Rev. Lett.* 105 (20 Nov. 2010), p. 200401. DOI: 10.1103/PhysRevLett.105.200401.

[150] M. B. Plenio and P. L. Knight. "The quantum-jump approach to dissipative dynamics in quantum optics". In: *Rev. Mod. Phys.* 70 (1 Jan. 1998), pp. 101–144. DOI: 10.1103/RevModPhys.70.101.

[151] Albert Einstein and Brian Greene. *The meaning of relativity: including the relativistic theory of the non-symmetric field*. eng. 5th ed. Princeton Science Library. Princeton: Princeton University Press, 1970. ISBN: 0-691-02352-2.

[152] C. Y. Lo. *Einstein's Principle of Equivalence and the Einstein-Minkowski Condition*. Tech. rep. APRI-TH-PHY-005-01. 17 Newcastle Drive, Nashua, NH 03060: Fermilab, Nov. 2005.

[153] G. M. Tino et al. "Precision gravity tests and the Einstein Equivalence Principle". In: *Progress in Particle and Nuclear Physics* 112 (2020), p. 103772. ISSN: 0146-6410. DOI: 10.1016/j.ppnp.2020.103772.

[154] Galileo Galilei. *Le opere di Galileo Galilei*. Vol. 8. Tip. di G. Barbèra, 1898.

[155] Loránd Eötvös. "Über die Anziehung der Erde auf verschiedene Substanzen". In: *Mathematische und naturwissenschaftliche Berichte aus Ungarn* 8 (1890), pp. 65–68.

[156] S. Carusotto et al. "Test of g universality with a Galileo type experiment". In: *Phys. Rev. Lett.* 69.12 (Sept. 1992), pp. 1722–1725. DOI: 10.1103/PhysRevLett.69.1722.

[157] S. Schlamminger et al. "Test of the Equivalence Principle Using a Rotating Torsion Balance". In: *Phys. Rev. Lett.* 100.4 (Jan. 2008), p. 041101. DOI: 10.1103/PhysRevLett.100.041101.

[158] Lin Zhu et al. "Test of the equivalence principle with chiral masses using a rotating torsion pendulum". In: *Physical Review Letters* 121.26 (2018), p. 261101. DOI: 10.1103/PhysRevLett.121.261101.

[159] Chris Overstreet et al. "Effective inertial frame in an atom interferometric test of the equivalence principle". In: *Physical review letters* 120.18 (2018), p. 183604. DOI: 10.1103/PhysRevLett.120.183604.

[160] Pierre Touboul et al. "MICROSCOPE Mission: Final Results of the Test of the Equivalence Principle". In: *Phys. Rev. Lett.* 129.12 (Sept. 2022), p. 121102. DOI: 10.1103/PhysRevLett.129.121102.

[161] David Mattingly. "Modern Tests of Lorentz Invariance". In: *Living Reviews in Relativity* 8.1 (Dec. 2005), p. 5. ISSN: 1433-8351. DOI: 10.12942/lrr-2005-5.

[162] Jun-Jie Wei and Xue-Feng Wu. "Tests of Lorentz Invariance". In: *Handbook of X-ray and Gamma-ray Astrophysics*. Ed. by Cosimo Bambi and Andrea Santangelo. Singapore: Springer Nature Singapore, 2024, pp. 5305–5334. ISBN: 978-981-19-6960-7. DOI: 10.1007/978-981-19-6960-7_132.

[163] Yuta Michimura et al. "New Limit on Lorentz Violation Using a Double-Pass Optical Ring Cavity". In: *Phys. Rev. Lett.* 110.20 (May 2013), p. 200401. DOI: 10.1103/PhysRevLett.110.200401.

[164] S. Herrmann et al. "Rotating optical cavity experiment testing Lorentz invariance at the 10^{-17} level". In: *Phys. Rev. D* 80.10 (Nov. 2009), p. 105011. DOI: 10.1103/PhysRevD.80.105011.

[165] John Ellis et al. "Robust constraint on Lorentz violation using Fermi-LAT gamma-ray burst data". In: *Phys. Rev. D* 99.8 (Apr. 2019), p. 083009. DOI: 10.1103/PhysRevD.99.083009.

[166] V. A. Acciari et al. "Bounds on Lorentz Invariance Violation from MAGIC Observation of GRB 190114C". In: *Phys. Rev. Lett.* 125.2 (July 2020), p. 021301. DOI: 10.1103/PhysRevLett.125.021301.

[167] Zhen Cao et al. "Stringent Tests of Lorentz Invariance Violation from LHAASO Observations of GRB 221009A". In: *Phys. Rev. Lett.* 133.7 (Aug. 2024), p. 071501. DOI: 10.1103/PhysRevLett.133.071501.

[168] Merce Guerrero et al. "Bounding anisotropic Lorentz invariance violation from measurements of the effective energy scale of quantum gravity". In: *Phys. Rev. D* 112.10 (Nov. 2025), p. 104002. DOI: 10.1103/k3xg-wkrc.

[169] Andrew S. Friedman et al. "Constraints on Lorentz invariance and CPT violation using optical photometry and polarimetry of active galaxies BL Lacertae and S5 B0716+714". In: *Phys. Rev. D* 99.3 (Feb. 2019), p. 035045. DOI: 10.1103/PhysRevD.99.035045.

[170] Jun-Jie Wei. "New constraints on Lorentz invariance violation with polarized gamma-ray bursts". In: *Monthly Notices of the Royal Astronomical Society* 485.2 (Mar. 2019). _eprint: https://academic.oup.com/mnras/article-pdf/485/2/2401/28027389/stz594.pdf, pp. 2401–2406. ISSN: 0035-8711. DOI: 10.1093/mnras/stz594.

[171] David Amram et al. "New Constraint for Isotropic Lorentz Violation from LHC Data". In: *Phys. Rev. Lett.* 132.21 (May 2024), p. 211801. DOI: 10.1103/PhysRevLett.132.211801.

[172] R. Aaij et al. "Search for Violations of Lorentz Invariance and CPT Symmetry in $B^0_{(s)}$ Mixing". In: *Phys. Rev. Lett.* 116.24 (June 2016), p. 241601. DOI: 10.1103/PhysRevLett.116.241601.

[173] J. P. Lees et al. "Tests of CPT symmetry in B^0–$\bar{B}^0$ mixing and in $B^0 \to c\bar{c}K^0$ decays". In: *Phys. Rev. D* 94.1 (July 2016), p. 011101. DOI: 10.1103/PhysRevD.94.011101.

[174] F. Allmendinger et al. "New Limit on Lorentz-Invariance- and CPT-Violating Neutron Spin Interactions Using a Free-Spin-Precession ^{3}He-^{129}Xe Comagnetometer". In: *Phys. Rev. Lett.* 112.11 (Mar. 2014), p. 110801. DOI: 10.1103/PhysRevLett.112.110801.

[175] Steven Peil et al. "Tests of local position invariance using continuously running atomic clocks". In: *Phys. Rev. A* 87.1 (Jan. 2013), p. 010102. DOI: 10.1103/PhysRevA.87.010102.

[176] H. Y. Carr and E. M. Purcell. "Effects of Diffusion on Free Precession in Nuclear Magnetic Resonance Experiments". In: *Phys. Rev.* 94.3 (May 1954), pp. 630–638. DOI: 10.1103/PhysRev.94.630.

[177] S. Meiboom and D. Gill. "Modified Spin-Echo Method for Measuring Nuclear Relaxation Times". In: *Review of Scientific Instruments* 29.8 (Aug. 1958), pp. 688–691. ISSN: 0034-6748. DOI: 10.1063/1.1716296.

[178] N Dimarcq et al. "Roadmap towards the redefinition of the second". In: *Metrologia* 61.1 (Jan. 2024), p. 012001. DOI: 10.1088/1681-7575/ad17d2.

[179] E. Peik and Chr Tamm. "Nuclear laser spectroscopy of the 3.5 eV transition in Th-229". In: *Europhysics Letters* 61.2 (Jan. 2003), p. 181. DOI: 10.1209/epl/i2003-00210-x.

[180] Benedict Seiferle et al. "Energy of the ^{229}Th nuclear clock transition". In: *Nature* 573.7773 (Sept. 2019), pp. 243–246. ISSN: 1476-4687. DOI: 10.1038/s41586-019-1533-4.

[181] Tomas Sikorsky et al. "Measurement of the ^{229m}Th Isomer Energy with a Magnetic Microcalorimeter". In: *Phys. Rev. Lett.* 125.14 (Sept. 2020), p. 142503. DOI: 10.1103/PhysRevLett.125.142503.

[182] Sandro Kraemer et al. "Observation of the radiative decay of the ^{229}Th nuclear clock isomer". In: *Nature* 617.7962 (May 2023), pp. 706–710. ISSN: 1476-4687. DOI: 10.1038/s41586-023-05894-z.

[183] J. Tiedau et al. "Laser Excitation of the Th-229 Nucleus". In: *Phys. Rev. Lett.* 132.18 (Apr. 2024), p. 182501. DOI: 10.1103/PhysRevLett.132.182501.

[184] Chuankun Zhang et al. "Frequency ratio of the ^{229m}Th nuclear isomeric transition and the 87Sr atomic clock". In: *Nature* 633.8028 (Sept. 2024), pp. 63–70. ISSN: 1476-4687. DOI: 10.1038/s41586-024-07839-6.

[185] Vera M. Schäfer et al. "Continuous recoil-driven lasing and cavity frequency pinning with laser-cooled atoms". In: *Nature Physics* 21.6 (June 2025), pp. 902–908. ISSN: 1745-2481. DOI: 10.1038/s41567-025-02854-4.

[186] Julia R. K. Cline et al. "Continuous Collective Strong Coupling of Strontium Atoms to a High Finesse Ring Cavity". In: *Phys. Rev. Lett.* 134.1 (Jan. 2025), p. 013403. DOI: 10.1103/PhysRevLett.134.013403.

[187] John K. Stockton, Xinan Wu, and Mark A. Kasevich. "Bayesian estimation of differential interferometer phase". In: *Phys. Rev. A* 76 (3 Sept. 2007), p. 033613. DOI: 10.1103/PhysRevA.76.033613.

[188] Romaric Journet et al. "Differential polarizability of the strontium intercombination transition at 1064.7 nm". In: *Phys. Rev. A* 110 (3 Sept. 2024), p. 032819. DOI: 10.1103/PhysRevA.110.032819.

[189] Thomas Middelmann et al. "High Accuracy Correction of Blackbody Radiation Shift in an Optical Lattice Clock". In: *Phys. Rev. Lett.* 109 (26 Dec. 2012), p. 263004. DOI: 10.1103/PhysRevLett.109.263004.

Appendix A

Supplemental material for Chapter 5

This chapter was previously published as the supplement to Shuo Ma, Jonathan Dolde, Xin Zheng, Dhruva Ganapathy, Alexander Shtov, Jenny Chen, Anke Stöltzel, Bennett J. Christensen, and Shimon Kolkowitz. "Enhancing Optical Lattice Clock Coherence Times with Erasure Conversion". In: PRX Quantum *6.4 (Nov. 2025), p. 040340.* DOI: *10.1103/2rqf-r9gw.*

A.1 Ellipse fitting with maximum likelihood estimator

In order to calculate the differential phase between the two atomic ensembles, we use the angle inferred by fitting the data to an ellipse. For the spin echo sequence, this angle is very close to zero, and the ellipse is close to a line. In this regime, traditional least squares estimators are biased [73]. To overcome this limitation, and in contrast to our fitting in previous chapters, we use Maximum Likelihood Estimation (MLE) [187]. This involves maximizing the likelihood function which quantifies the probability of observing the given data as a function of the model's parameters with the assumption that quantum projection noise is the dominant source of noise in the data. By performing tests on simulated data (see Fig. A.1(c)), we see that MLE exhibits no bias over a wide range of phases in ellipse angle estimation. However, bias is not completely eliminated at near-zero differential phases. This is mitigated experimentally by introducing a phase offset, which is discussed in Section A.2.

The variance of the contrast is determined using a resampling technique [56] known as jackknifing :

$$\text{var } C = \frac{N}{N-1}\sum(\bar{C}^{\text{JK}} - \bar{C}^{\text{JK}}_{\neq i})^2, \tag{A.1}$$

where N is the total number of measurements, and $\bar{C}^{\text{JK}}$ is the mean of $\bar{C}^{\text{JK}}_{\neq i}$, which is a fit to all data except the i^{th} data point.

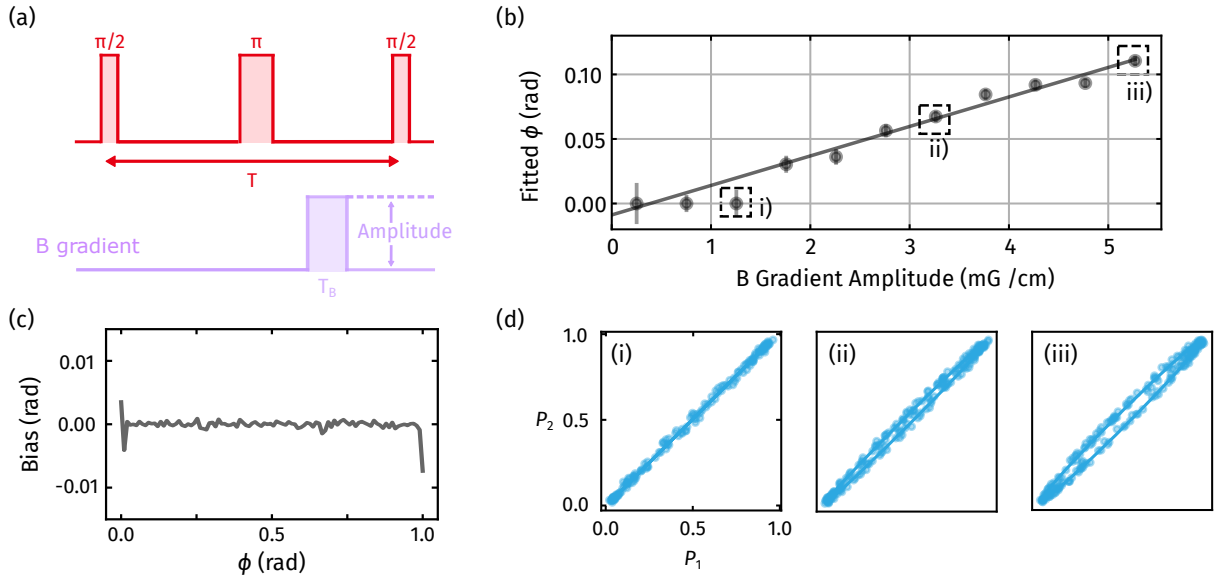


Figure A.1: Illustration of modified spin echo sequence. (a) Timing sequence for modified spin echo. To operate away from zero phase shift, a magnetic field (0.5 to 5 mG/cm) is applied to the second free evolution period for time TB =1.4 s.(b) Fitted phase using MLE as a function of B field gradient dB/dz. The solid line is fitted using data points at high gradient (>2mG/cm) and shows a fitted offset phase ϕ of -0.004(0.007) radians without gradient field, consistent with vanishing bias error using MLE. (c) Implementation of the MLE algorithm to estimate the relative phase of the ellipse. (d) Callout of specific ellipse fittings using MLE under varying magnetic field gradients.

A.2 Modified spin echo sequence

While the traditional spin echo sequence effectively removes inhomogeneous broadening at higher Fourier frequencies, it typically results in near-zero differential phase shifts during differential clock comparisons. Despite upgrading our ellipse estimator with MLE, this near-zero phase regime introduces bias. To address this, while still canceling most of the inhomogeneous broadening, we perform a modified spin echo sequence, as depicted in Fig. A.1(a).

In this sequence, a fixed-duration, amplitude-tunable magnetic field gradient is applied during the second half of the spin echo period. We fit the ellipses obtained by varying the magnetic field gradient (from 0.02 to 5.5mG/cm) and plot the extracted differential phase shifts as a function of the applied gradient. Several representative fit results are shown in Fig. A.1(d). Based on these, we choose to operate at a gradient of approximately 2.0 mG/cm, where the phase shift remains linear and the overall phase is kept small, minimizing bias while retaining effective decoherence cancellation.

A.3 Raman scattering population distribution calculation

We calculate the scattering rate from $|^3\mathrm{P}_0, m_F\rangle$ to $|^3\mathrm{P}_J, m'_F\rangle$ by the 813.4 nm lattice light following the formalism in [133]. We use the reduced matrix elements (RME) and transition frequencies for $^3\mathrm{P}_1$ from [188] and derive the RME for $^3\mathrm{P}_0$ transitions based on the line strengths and frequencies reported in [189].

Table Table A.1 presents the calculated off-resonant scattering rates for a π-polarized optical lattice, where atoms initially in the $|^3\mathrm{P}_0, m_F = 3/2\rangle$ state (labeled as state i) scatter to $|^3\mathrm{P}_1, m_F\rangle$ (state j). The subsequent decay rate to $|^1\mathrm{S}_0, m_F\rangle$ is determined using Clebsch-Gordan coefficients. All rates are calculated for a trap depth of 1 E_{rec}.

$i \to j$	F'	m'_F	$\Gamma/(10^{-4}\mathrm{s}^{-1})$
$^3\mathrm{P}_0 \to {}^3\mathrm{P}_1$	7/2	1/2	0.83
		3/2	0.
		5/2	0.17
	9/2	1/2	1.21
		3/2	0
		5/2	1.06
	11/2	1/2	0.46
		3/2	0
		5/2	1.27
$^3\mathrm{P}_0 \to {}^1\mathrm{S}_0$	9/2	-1/2	0.95
		1/2	0.68
		3/2	2.01
		5/2	0.79
		7/2	0.53
$^3\mathrm{P}_0 \to {}^3\mathrm{P}_2$			2.85
$^3\mathrm{P}_0 \to {}^3\mathrm{P}_0$			5.01

Table A.1: Theoretically calculated Raman scattering rates from $|^3\mathrm{P}_0, m_F = 3/2\rangle$ to various $|^3\mathrm{P}_1, m_F\rangle$ states at a lattice potential of 1 Erec, along with the subsequent decay rates to different $|^1\mathrm{S}_0, m_F\rangle$ states.

A.4 Theoretical discussion on coherence enhancement

In this section, we briefly discuss the origin of the enhanced clock coherence. We first consider a simple three-level model: $|c_g\rangle$, $|c_e\rangle$, and $|e\rangle$. Here, $|c_g\rangle$ and $|c_e\rangle$ represent the ground

and excited states of the clock transition (clock subspace), while $|e\rangle$ belongs to the disjoint subspace where population leaving the clock subspace is converted into detectable erasures.

For simplicity, we assume a general loss channel that transfers population out of the clock excited state, with a finite probability of decaying either to the clock ground state or to the erasure subspace. This channel effectively models a combination of radiative decay, Raman scattering, and blackbody-induced scattering. The impact of such a channel during clock interrogation can be described by a quantum channel with Kraus operators:

$$K_0(t) = |c_g\rangle\langle c_g| + \sqrt{e^{-\Gamma t}}\,|c_e\rangle\langle c_e| + |e\rangle\langle e| \tag{A.2}$$

$$K_1(t) = \sqrt{(1-r_e)(1-e^{-\Gamma t})}\,|c_g\rangle\langle c_e| \tag{A.3}$$

$$K_e(t) = \sqrt{r_e(1-e^{-\Gamma t})}\,|e\rangle\langle c_e| \tag{A.4}$$

Where Γ is the loss rate out of $|c_e\rangle$, and the fraction of loss that falls into the erasure subspace is denoted by r_e. K_0 describes how the state evolves when no loss occurs. Specifically, the population in $|c_g\rangle$ and $|e\rangle$ remains the same while the probability of $|c_e\rangle$ damps. K_1 represents the probability of population scattered from $|c_e\rangle$ to $|c_g\rangle$, and K_e represents the probability scattering to $|e\rangle$.

The standard readout method makes no distinction between the population in the clock subspace and the population in the erasure subspace. The evolution of the system corresponds to the full quantum channel and the coherence decays exponentially with a rate of $\Gamma/2$. However, the hyperfine-resolved readout gives access to the information solely in the clock subspace. Conditioning on not witnessing erasures, equivalent to only measuring population in the clock subspace, the system is subject to operations defined by K_0 and K_1. The outcome density matrix requires a proper renormalization as K_0 and K_1 together do not describe a complete quantum channel. The density matrix after evolution with hyperfine-resolved readout is in Eq. (A.5) and the coherence is shown in Eq. (A.6)

$$\rho = \frac{K_0\rho_0 K_0^\dagger + K_1\rho_0 K_1^\dagger}{\mathrm{Tr}(K_0\rho_0 K_0^\dagger + K_1\rho_0 K_1^\dagger)} \tag{A.5}$$

$$\rho_{eg} = \frac{e^{-\frac{\Gamma}{2}t}/2}{1+(e^{-\Gamma t}-1)r_e/2} \tag{A.6}$$

In Fig. A.2(a), we show the theoretically calculated coherence time as a function of the erasure fraction. The coherence time (defined as the $1/e$ time) increases with the erasure fraction, showing a $\times 1.6$ improvement at full erasure conversion. However, in this limit, the coherence time does not diverge to infinity, as K_0 is a non-Hermitian no-jump operator that induces wavefunction collapse upon a no-detection event[136].

For the spin echo sequence, shown in Fig. A.2(c), the population in the clock subspace is inverted by a π-pulse, effectively redistributing the probability of decay back to the initial ground state. At high erasure fractions, the probability of correctly inferring the likely origin of the erasure is suppressed. As shown in Fig. A.2, the coherence time increases monotonically

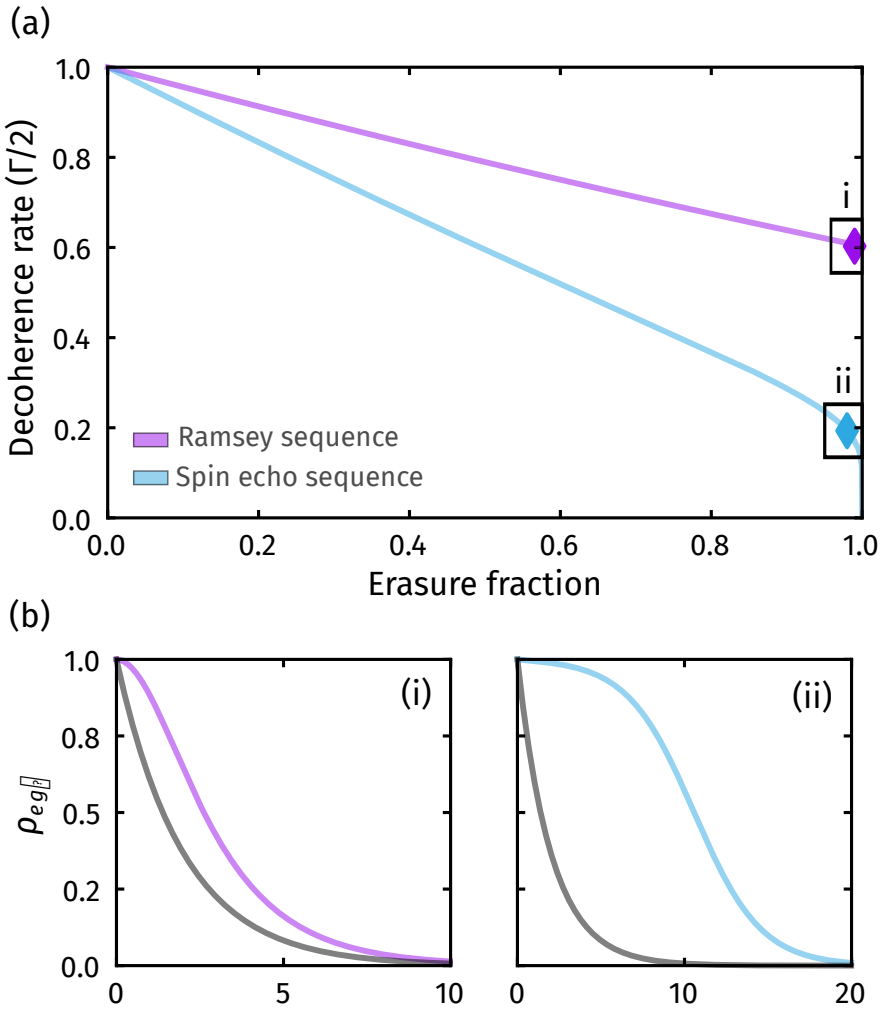


Figure A.2: (a) shows the theoretical decoherence rate for Ramsey (purple solid line) and spin echo (blue solid line) sequences with varying erasure fractions, assuming the only decoherence contribution is from erasure-convertible channels such as Raman scattering, loss, and radiative decay. (b) shows the calculated coherence versus time in the Ramsey sequence (i) with an erasure fraction of 1 and the spin echo sequence(ii) with an erasure fraction of 0.99. The black line in (i)&(ii) represents the coherence without erasure conversion.

as the erasure fraction approaches 1, ultimately limited by dephasing sources rather than loss mechanisms.

In the ensemble clock experiment, the inclusion of two-body collision-induced loss and density shifts introduces additional complexities in the dependence of coherence time on the erasure fraction. The density shift is incorporated as a phenomenological dephasing term to match experimental data, though a rigorous treatment would require solving the many-body dynamics.

A.5 Numerical simulation of the experiment

In this section, we present the numerical model of the experiment, incorporating additional loss and dephasing mechanisms such as two-body collision loss of $^3\mathrm{P}_0$ and dephasing from elastic scattering. We account for an effective trap depth by considering the finite radial temperature, following the formulation in Ref. [133]. The system dynamics are modeled using the density matrix formalism. Since the experiment involves simultaneous clock interrogation, laser phase noise does not affect atom-atom coherence and is therefore omitted from the simulation. In this framework, states 1, 2, and 3 correspond to the clock ground state, the clock excited state, and the remaining ground states, respectively.

$$\begin{aligned}
\dot{\rho}_{11} &= -\Gamma_{\mathrm{L}}^{\mathrm{g}}\rho_{11} + (\alpha\Gamma_{\mathrm{r}} + \beta\Gamma_0)\rho_{11} \\
\dot{\rho}_{22} &= -(\Gamma_{\mathrm{L}}^{\mathrm{e}} + \Gamma_0 + \Gamma_{\mathrm{r}} + \Gamma_{\mathrm{t}}\rho_{22})\rho_{22} \\
\dot{\rho}_{33} &= -\Gamma_{\mathrm{L}}^{\mathrm{g}}\rho_{33} + (1-\alpha)\Gamma_{\mathrm{r}}\rho_{22} + (1-\beta)\Gamma_0\rho_{22} \\
\dot{\rho}_{12} &= -\frac{1}{2}(\Gamma_{\mathrm{L}}^{\mathrm{g}} + \alpha\Gamma_{\mathrm{r}} + \beta\Gamma_0 + \Gamma_{\mathrm{t}}\rho_{22})\rho_{12} \\
&\quad - \Gamma_{\mathrm{t}}^{e}(\rho_{11} + \rho_{22} + \rho_{33})\rho_{12} - i\Delta\rho_{12} \\
\dot{\rho}_{21} &= -\frac{1}{2}(\Gamma_{\mathrm{L}}^{\mathrm{g}} + \alpha\Gamma_{\mathrm{r}} + \beta\Gamma_0 + \Gamma_{\mathrm{t}}\rho_{22})\rho_{21} \\
&\quad - \Gamma_{\mathrm{t}}^{e}(\rho_{11} + \rho_{22} + \rho_{33})\rho_{21} + i\Delta\rho_{21}
\end{aligned} \tag{A.7}$$

where $\Gamma_{\mathrm{L}}^{\mathrm{g}}$ is the one-body loss rate (2.1×10^{-2} s^{-1}) for ground-state atoms due to background gas collisions. $\Gamma_{\mathrm{L}}^{\mathrm{e}}$ is the one-body loss rate (2.7×10^{-2} s$^{-1}{E_{\mathrm{rec}}}^{-1} + 1.8 \times 10^{-2}$ s^{-1}) for the excited state, accounting for both background gas collisions and Raman scattering to $^3\mathrm{P}_2$. Γ_r is the Raman scattering rate to $^3\mathrm{P}_1$ (4.6×10^{-2} s$^{-1}{E_{\mathrm{rec}}}^{-1}$). Γ_0 is the natural lifetime of $^3\mathrm{P}_0$ (167 s).

The branching ratios of scattering and decay back to the clock subspace, α and β, are set to 0.18 and 0.42, respectively. Γ_{t} is the two-body loss rate coefficient (11×10^{-6} s^{-1}cm^{-3}). Δ is the laser detuning on the clock transition. All rates above are extracted from independent measurements of the $^3\mathrm{P}_0$ natural lifetime [123]. Quenching from blackbody radiation (BBR) provides an additional, but minor, contribution that would affect the erasure fraction. However, the overall BBR-induced decay rate out of $^3\mathrm{P}_0$ is smaller than the natural radiative lifetime, and quenching via $^3\mathrm{P}_2$ contributes only at second order. Consequently, BBR is not expected to be a significant source of error and is therefore neglected in the model.

We also incorporate a density-dependent phenomenological dephasing rate in the simulation. Notably, including a density-dependent dephasing term of 7.2×10^{-12} s^{-1}cm^{-3} is essential for achieving a good agreement between theory and experiment. We interpret this as capturing the effects of elastic scattering, similar to previous studies[139], though a complete description of elastic collisions would require a full many-body treatment of the clock ensemble.

In the simulation, we fit the total number of atoms remaining in the lattice at the end of the experiment and use the fitted atom number at $t = 0$ as the initial condition. When modeling the Ramsey experiment, we account for decoherence induced by magnetic field gradients within the ensemble. This is done by estimating the atomic distribution, assigning detunings based on axial positions, and averaging the coherence contribution across the ensemble.

Additionally, we incorporate a phenomenological Gaussian decay T_2^* in the simulation to account for slow noise sources recoverable by the spin echo sequence, such as residual Stark shifts from the lattice.

The coherence $C(T)$ is calculated as the off-diagonal matrix element $|\rho_{12}(T)|^2$ in the density matrix. The population $N(T)$ is the sum of the diagonal matrix elements. In the case of hyperfine readout, only the population remaining in the clock subspace is counted, and $N(T) = |\rho_{11}(T)|^2 + |\rho_{22}(T)|^2$. In the standard readout, the population sums over all diagonal matrix elements, including the remaining ground state population. Based on the simulated coherence $C(T)$ and atom number $N(T)$ as functions of interrogation time, we extract the QPN-limited Allan deviation using

$$\sigma_{\mathrm{QPN}}(T) = \frac{\sqrt{2}S(\phi, C(T))}{2\pi\nu C(T)T}\sqrt{\frac{T + T_d}{N(T)\tau}} \tag{A.8}$$

where ν is the clock transition frequency, $C(T)$ is the simulated atomic coherence, T is the coherent interrogation time, and T_d is the dead time between experimental shots, and $N(T)$ is the number of atoms. For standard and reconstructed readout, $T_d = 1.75$ s, while for the hyperfine-resolved readout sequence, $T_d = 1.95$ s.

For differential clock measurements, the quantum projection noise limit leads to an additional scaling factor in the stability of the clock comparison that depends on the accumulated phase difference between the two ensembles as well as the contrast of the ellipse [56, 57, 59]. We include this effect as an additional factor $S(\phi, C(T))$ given by

$$\begin{aligned} S &= \Big(\int_0^{2\pi} \frac{d\theta}{4\pi} \frac{1}{\csc^2(\theta)\tilde{\sigma}^2(x) + \csc^2(\theta+\phi)\tilde{\sigma}^2(y)} \Big)^{-\frac{1}{2}} \\ \tilde{\sigma}^2(x) &= \frac{C(T)}{2}\cos(\theta) - \frac{C(T)^2}{4}\cos^2(\theta) \\ \tilde{\sigma}^2(y) &= \frac{C(T)}{2}\cos(\theta+\phi) - \frac{C(T)^2}{4}\cos^2(\theta+\phi) \end{aligned} \tag{A.9}$$

where θ represents the clock laser's phase and ϕ is the relative phase between the two ensembles. Because our differential clock measurement interrogates atoms beyond the atom-laser coherence time, the scaling factor is averaged over θ and thus depends on the relative phase ϕ and the contrast of the ellipse. For the Ramsey measurements, this relative phase evolves over time due to the detuning between the two ensembles, resulting in an oscillating and non-trivial dependence of stability with interrogation time T. We therefore only consider

an idealized Allan deviation based on the simulated coherence and number of atoms without accounting for the additional effect of the phase, i.e., $\phi = 0$, which represents a lower bound on the Ramsey stability. For the spin echo measurements, the accumulated phase difference is the result of the applied magnetic field gradient and is independent of interrogation time (as described in Section A.2), so we calculate the expected stability accounting for the applied phase difference i.e. $\phi = 0.04$ radians.

A.6 Discussion of technical limitations

As discussed in the main text, the two dominant error sources in the experiment are π-pulse infidelity and off-resonant scattering by the clock laser.

The π-pulse infidelities primarily arise from the phase noise of our local oscillator (LO) and atomic temperature variations. LO phase noise can be mitigated by operating at a higher Rabi frequency or by reducing laser noise through a longer cavity spacer with improved thermal shielding. Atomic temperature variations lead to inconsistent Rabi frequencies for atoms in different axial lattice bands, as well as radial inhomogeneity in regions of weaker confinement. Employing a larger lattice beam waist and deeper cooling is expected to mitigate these effects. By addressing these issues, we anticipate achieving a clock π-pulse fidelity of up to 99.5%.

Additionally, off-resonant scattering of the clock light from adjacent m_F states exacerbates the problem. At a bias magnetic field of approximately 5.5 G, the separation between adjacent m_F states is $\Delta \approx 2\pi \times 1000$ Hz, while the Rabi frequency is $\Omega \approx 2\pi \times 150$ Hz, leading to a few percent of non-resonant excitation. Since off-resonant scattering scales as $\Omega^2/(\Omega^2 + \Delta^2)$, operating at a bias field of ~ 50 G and increasing Ω by a factor of 4 to improve the fidelity of the clock pulse could reduce off-resonant scattering by approximately a factor of 7.

A.7 Coherence and Allan deviation at all trap depths

In this section, we present the results of coherence and clock stability as functions of clock interrogation time in Fig. A.3, measured at the trap depths described in the main text. The simulated coherence decay and calculated stability curves are also presented. The stability plot for the Ramsey sequence, shown in Fig. A.3 (a), includes an idealized modeled stability (dashed curve) accounting for the simulated coherence and number of atoms calculated based on Eq. (A.8). In the spin echo sequence plot, shown in Fig. A.3 (b), we included a modeled stability (solid curves) that accounts for the relative accumulated phase between the two ensembles, as discussed in Section A.5.

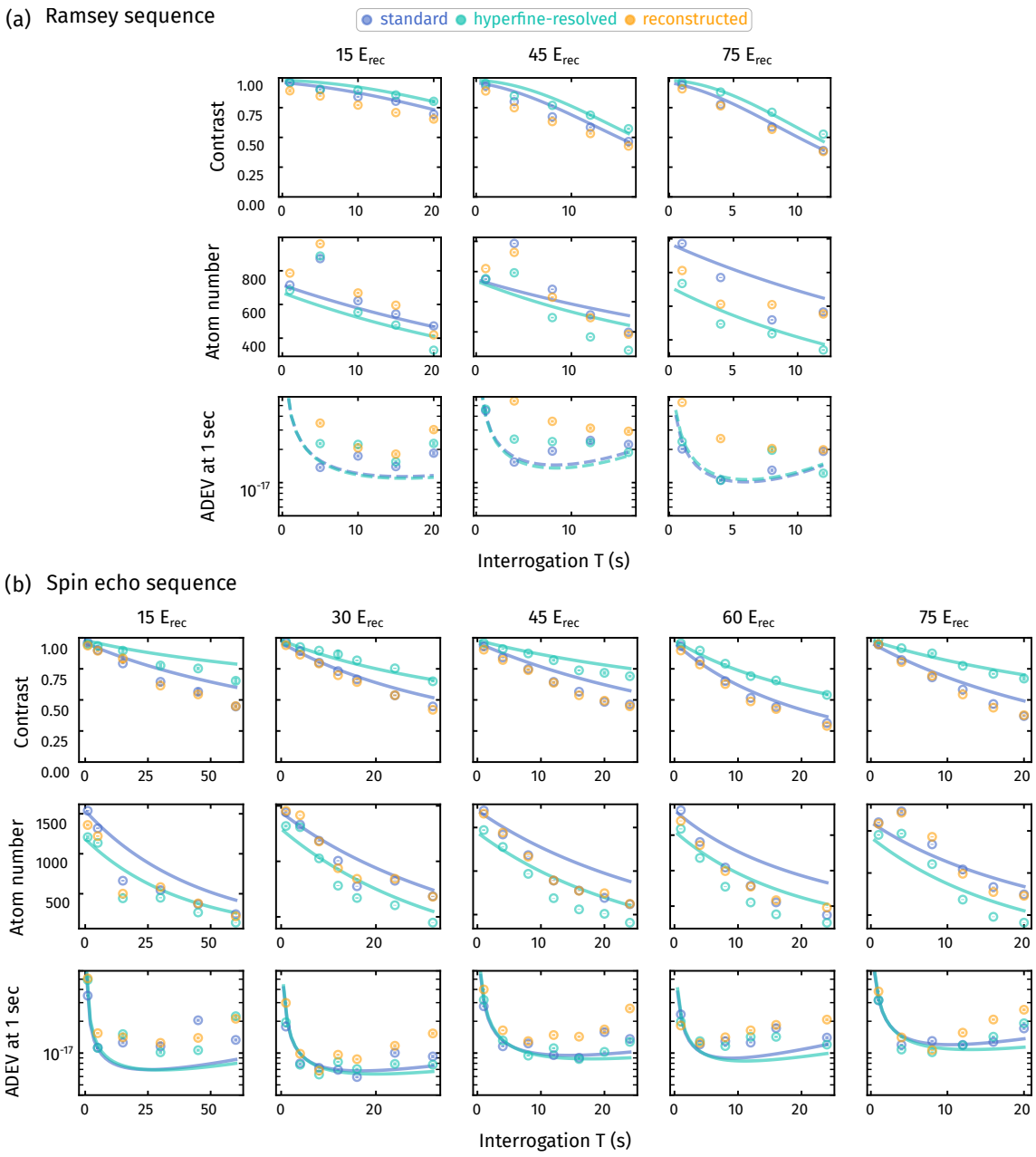


Figure A.3: Coherence, atom number and clock stability as functions of clock interrogation time at all trap depths measured (from 15 to 75 E_{rec}) for (a) Ramsey sequence and (b) spin echo sequence. The simulated curves are plotted with the same color coding. The dashed curves in (a) represent the calculated stability using the simulated coherence and the remaining number of atoms, assuming the relative phase difference between ensembles is 0. The solid curves in (b) represent the calculated stability accounting for the effect of the relative accumulated phase between the two ensembles.